Mesoscale Benchmark Demonstration Problem 1: Mesoscale Simulations of Intra-granular Fission Gas Bubbles in UO_2 under Post-irradiation Thermal Annealing

Fuel Cycle Research & Development

Prepared for
U.S. Department of Energy
Fuel Cycle R&D Program

Yulan Li, Shenyang Hu, Robert Montgomery, Fei Gao, Xin Sun
Pacific Northwest National Laboratory, Richland, WA 99352
Michael Tonks, Bulent Biner, Paul Millett
Idaho National Laboratory, Idaho Falls, ID 83415
Veena Tikare
Sandia National Laboratory, Albuquerque, NM 87185
Balasubramaniam Radhakrishnan
Oak Ridge National Laboratory, Oak Ridge, TN 37831
David Andersson
Los Alamos National Laboratory, Los Alamos, NM 87545

April 2012
FCR&D-MDSM-2012-000098
PNNL-21295

Reviewed by:

National Technical Director, Nuclear Energy
Advanced Modeling and Simulation

Keith Bradley Date

Concurred by:

Acting Director, Advanced Modeling and
Simulation Office

Trevor Cook Date

Approved by:

Deputy Assistant Secretary, Nuclear Energy

John Kelly Date

Mesoscale Benchmark Demonstration

Problem 1: Mesoscale Simulations of Intra-granular Fission Gas Bubbles in UO_2 under Post-irradiation Thermal Annealing

SUMMARY

A study was conducted to evaluate the capabilities of different numerical methods used to represent microstructure behavior at the mesoscale for irradiated material using an idealized benchmark problem. The purpose of the mesoscale benchmark problem was to provide a common basis for assessing several mesoscale methods to identify the strengths and areas of improvement in the predictive modeling of microstructure evolution. In this work, mesoscale models (phase-field, Potts, and kinetic Monte Carlo) developed by Pacific Northwest National Laboratory, Idaho National Laboratory, Sandia National Laboratory, and Oak Ridge National Laboratory were used to calculate the evolution kinetics of intra-granular fission gas bubbles in UO_2 fuel under post-irradiation thermal annealing conditions. The benchmark problem was constructed to include important microstructural evolution kinetics of intra-granular fission gas bubble behavior, such as the atomic diffusion of Xe atoms, U vacancies, and O vacancies; the effect of vacancy capture and emission from defects; and the elastic interaction on non-equilibrium gas bubbles. An idealized set of assumptions and a common set of thermodynamic and kinetic data were imposed on the benchmark problem to simplify the mechanisms considered. The modeling capabilities of different methods are compared against selected experimental and simulation results. These comparisons find that while the phase-field methods and Potts kinetic Monte Carlo methods are able to incorporate several of the mechanisms that influence intra-granular bubble growth and coarsening, the Potts model is challenged by the low solubility and long-range diffusion necessary to simulate this problem correctly. The statistical-mechanical nature of Potts kMC requires large ensembles with long simulation times to treat this problem. Future efforts are recommended to construct increasingly more complex mesoscale benchmark problems to further verify and validate the predictive capabilities of the mesoscale modeling methods used in this study.

Key words: mesoscale benchmark; phase-field approach; kinetic Monte Carlo approach; Potts model; fission gas bubbles; uranium dioxide; post-irradiation thermal annealing.

CONTENTS

FIGURES

TABLES

ACRONYMS

°C	degree(s) Celsius or Centigrade
2-D	two-dimensional (or two dimensions)
3-D	three-dimensional (three dimensions)
$Å^3$	cubic Angstrom
C	constant temperature
CPU	central processing unit
DFT	Density Functional Theory
DOF	degrees of freedom
eV	electron volt
FEM	finite element method
FFTW	Fastest Fourier Transform in the West
GPa	Giga pascal
GWd/MTU	gigawatt-days per metric ton uranium
h	hour(s)
INL	Idaho National Laboratory
J/m^2	joule per square meter
K	Kelvin
kMC	kinetic Monte Carlo
Kr	krypton
LANL	Los Alamos National Laboratory
LWR	light water reactor
min	minute(s)
MD	molecular dynamics
MCS	Monte Carlo time
O	oxygen
ORNL	Oak Ridge National Laboratory
PF	phase-field
PNNL	Pacific Northwest National Laboratory
R	ramp temperature
s or sec	second(s)
SNL	Sandia National Laboratory
U	uranium
UO_2	uranium dioxide
Xe	xenon

FUEL CYCLE R&D PROGRAM

MESOSCALE BENCHMARK DEMONSTRATION

PROBLEM 1: MESOSCALE SIMULATIONS OF INTRA-GRANULAR FISSION GAS BUBBLES IN UO_2 UNDER POST-IRRADIATION THERMAL ANNEALING

1. INTRODUCTION

Computational materials science—an active research area under intensive development in recent years—promises to provide improved and predictive capability for the modeling and simulation of material microstructural, mechanical, and thermal behaviors under extreme environmental conditions. The ability to describe and model the complex behavior of materials from the atomistic to the continuum scales can provide opportunities to design new materials and better understand and use existing materials. In general, computational materials models can be categorized into three groups based on their temporal and spatial domains of interest: at the atomistic scale, models include density functional theory (DFT) [1-4] and molecular dynamics (MD) methods [5-10]; at the mesoscale (i.e., microstructure level), models include the kinetic Monte Carlo (kMC) (i.e., Potts model) [11], and the phase-field (PF) methods [12-15]; at the continuum scale, methods include the finite element [16] and finite volume methods [17, 18].

A key challenge in modeling material behavior using the described multi-scale approach is the bridging or transfer of information across the disparate time and spatial scales of importance. Modeling within the atomistic domain considers at most microseconds and nanometers (millions of atoms and their motion) in describing atomic or molecular interactions. The continuum domain modeling can stretch to years and centimeters in the case of nuclear fuel rods or irradiated material. Given the large disparities between these domains, mesoscale methods may play a key role in bridging the temporal and spatial scales in computational materials science and may provide methods to better inform the constitutive models used at the continuum scale.

The atomistic and continuum domains are mature areas of computational materials science modeling with established confidence in the ability of their methods to provide predictive simulations, using, in the case of continuum level, semi-empirical constitutive models that may include lower length scale properties (e.g., diffusivities or Burger's vector). In contrast, the mesoscale domain of materials modeling is a relatively new area of development in computational materials science that resides between the discrete atomic particle models and the continuum representation. The characteristic length scales generally range from 100s of nanometers to 10s of micrometers and time scales of 10^{-3} to 10^{2} seconds. At these scales, the domain is often too small to be considered a continuum level representation, yet too large to effectively use atomistic methods. The advantage of the mesoscale modeling domain lies in the fact that microstructure-level material characteristics such as inhomogeneity, i.e., grains, grain boundaries or other

defects, can be represented in local detail and their interactions with atomic processes can be explicitly considered. These microstructural features have a deciding impact on material behavior on the continuum scale. Various mesoscale modeling methods have been successfully demonstrated to topographically represent the evolution of material microstructure during grain growth, sintering, and migration of bubbles within the solid. However, an important gap in the various mesoscale modeling methods is the lack of quantitative verification and validation in predicting microstructure evolution kinetics with quantitative inputs from the atomistic scale, particularly under complex conditions of temperature, strain, and radiation damage.

Several mesoscale modeling methods have been developed to evaluate microstructure evolution during the process of grain growth, phase transformation, second phase particle growth, etc. [12, 14, 15, 19]. The most widely used and well-known mesoscale modeling methods used in computational materials science are the Potts, kMC, and the PF approaches. The first two methods are discrete ensemble representations that use a statistical-mechanical approach to represent the evolution of distinct interfaces in the microstructure. The PF approach is a thermodynamic model that represents the microstructure using a continuum field with a set of smoothly changing order parameters to define the interfaces. Each of these methods has been successfully used to simulate microstructure evolution in metal and ceramic materials under conditions without irradiation. Tikare et al. [20] have compared the Potts and PF methods for grain growth simulations and Ostwald ripening processes. For these single-mechanism simulations, both methods gave similar topological results.

Application of mesoscale methods to predict microstructure evolution driven by complex and interacting mechanisms, such as those that occur in nuclear fuel under irradiation, has grown recently with the advancement of computational capabilities and the desire to improve the semi-empirical material models used in representing these systems. The ultimate goal in applying mesoscale methods to irradiated materials is to develop a quantitative, mechanistic-based multi-physics representation of the underlying processes controlling the microstructure evolution for predicting the material properties evolution at the continuum scale, i.e., thermal conductivity, elastic modulus, creep, and behavior of second phase particles or fission products. For example, the migration of fission gas atoms in nuclear fuel material is influenced by several important microstructural mechanisms, including 1) gas atom diffusion, 2) gas atom or vacancy trapping by defects and dislocations, 3) interaction with fission fragments and fission-induced cascades, 4) nucleation and growth of gas bubbles, 5) absorption and resolution from gas bubbles, 6) non-equilibrium pressure conditions in gas bubbles, and 7) elastic interactions between defects and bubbles. All of these mechanisms have a combined effect in controlling the rate of gas atom diffusion to the grain boundary and its ultimate release from the fuel. Semi-empirical continuum-level models approximate all of these mechanisms into a single effective diffusivity with limited predictive capability.

As the complexity of microstructure modeling has grown, verifying the predictive capabilities of mesoscale methods becomes more difficult, and those conducting the exercises used to validate the results must have a deep understanding of the interacting mechanisms that control the microstructural data. Very few separate effect experiments are available to provide the microstructure characteristics in sufficient detail to quantitatively verify the mesoscale methods. As a result, a concerted effort is required to engage a spectrum of experts who understand the intricacies of the experimental data, the current knowledge of

the microstructure evolution kinetics, and the different continuum and mesoscale modeling methods in order to formulate the verification and validation problems that can truly evaluate the predictive capabilities of these methods.

1.1 Study Purpose and Scope

This report describes a study undertaken to evaluate the capabilities of different methods used to represent microstructure behavior at the mesoscale for irradiated material using an idealized benchmark problem. The goal of developing such a benchmark problem is to provide a common basis for assessing the strength and areas of improvement for several different mesoscale methods in predicting the microstructure evolution of nuclear fuel material. The different mesoscale methods considered in this study include the PF method, Potts model, and kMC approaches. The benchmark problem summarized in this report is related to the growth and coarsening behavior of intra-granular fission gas bubbles observed after a post-irradiation thermal annealing test for uranium dioxide (UO_2), and it is the first in a series of verification problems that will be constructed to begin the process of quantitative verification of mesoscale methods for predicting microstructure evolution. It is envisioned that additional test problems will be constructed and analyzed that involve increasingly more complex multi-physics behavior, including defect-dislocation interactions and fission-induced damage.

A multi-laboratory team of researchers from Pacific Northwest National Laboratory (PNNL), Idaho National Laboratory (INL), Sandia National Laboratory (SNL), Oak Ridge National Laboratory (ORNL), and Los Alamos National Laboratory (LANL) participated in the benchmark problem by performing analyses with various mesoscale methods as part of this study. An important aspect of defining a common benchmark problem was to establish a consistent set of initial, boundary, and thermodynamic conditions across the selected mesoscale methods.

1.2 Report Contents and Organization

The ensuing sections of this report begin by describing the microstructure behavior of irradiated UO_2 material and the relevant aspects that will be considered in the mesoscale benchmark problem (Section 2). Section 3 outlines the benchmark problem definition, including the initial, boundary, and thermodynamic conditions. It also includes a set of calculations performed to verify that the formulation of the different interacting mechanisms on the bubble growth behavior is reasonable. Section 4 summarizes the mesoscale methods used in the evaluation and a comparison of the assumptions and results between the different approaches. Areas of common agreement and areas for further improvement are identified. Section 5 discusses the key conclusions from this evaluation and provides suggestions for further analytical evaluation and experimental data generation. Detailed descriptions of the mesoscale methods used in this evaluation and the detailed results for the benchmark problem are contained in appendixes.

2. MICROSTRUCTURE BEHAVIOR IN IRRADIATED UO_2 MATERIALS

The thermal, mechanical, and chemical behavior of nuclear fuel material during normal operations and transient conditions is an important element of the performance, reliability, and safety of any nuclear reactor. Implicit in this behavior is the changing microstructure of the material as a consequence of radiation damage, fission product generation, temperature and stress fields, etc. Understanding the impact of the microstructure evolution on the material properties such as thermal conductivity, elastic modulus, creep, and fission product retention is critical to evaluating the performance of the fuel material. Extensive experimental and analytical work has been conducted to develop this understanding. What is known is that the evolving state of the microstructure and its impact on material properties in irradiated material is a complex multi-scale and multi-physics process composed of many interacting and competing mechanisms, including radiation-induced defects, moving grain boundaries, gas bubbles and porosity, fission product compounds, non-stoichiometry, etc. [21-24].

2.1 Fission Gas Behavior in UO_2 Fuel

During irradiation of light water reactor (LWR) fuel, the fission process generates many different fission product atoms, including xenon (Xe) and krypton (Kr) atoms. The noble gas atoms Xe and Kr represent about 30% of the fission products produced, and the behavior of the gas atoms is important to the microstructure evolution and overall performance of the fuel. Because of the extremely low solubility of the noble gas atoms in the UO_2 matrix, gas bubbles composed of Xe , Kr, and other gas atoms precipitate within the UO_2 grains and, depending on the temperature conditions, gas atom diffusion will result in nucleation and growth of gas bubbles on the grain boundaries. Continuum-level mechanisms, such as fission gas release to the fuel rod environment and volumetric swelling due to bubble growth, are included in nuclear fuel performance assessments.

The behavior of fission gas atoms in UO_2 has been extensively studied using experiments performed on single crystal and polycrystalline material under a variety of temperature and irradiation conditions for more than 50 years [21, 24-29]. From these studies a general picture of the mechanisms that influence the transport and release of fission gas atoms has been developed. Thermally induced fission gas diffusion and release from the fuel generally occurs in two stages: 1) diffusion and trapping of single Xe gas atoms within the grains, and 2) formation and inter-linkage of grain boundary bubbles. A schematic of these processes is shown in Figure 1. First, a gas atom is created within a region of radiation-induced vacancies and interstitial atoms caused by the atomic interactions/cascades during the stopping process following fission. Gas atom diffusion assisted by uranium (U) vacancy clusters then takes over until nucleation of small high pressure intra-granular bubbles. These bubbles act as trapping sites for gas atoms until a fission fragment spike causes resolution of Xe atoms back into the matrix. Several transmission electron microscopy studies of irradiated fuel have found that the mean radius of the intra-granular bubbles is approximately 1 nm with only a slight dependency on the burnup or concentration of the Xe atoms in the matrix [30, 31]. At sufficient temperatures (> 800°C), gas atoms diffuse to the grain boundary and nucleate grain boundary bubbles. Some fraction of the gas in the grain boundary bubbles is knocked back

into the grain by interactions with fission fragments. The remainder continues to cause the grain boundary bubbles to grow until inter-linkage of bubbles results in venting of the gas out of the fuel.

These two stages are modeled at the continuum level using semi-empirical models that consider an effective diffusion coefficient that represents the trapping at intra-granular bubbles and dislocations within the grain, and various parameters that describe the nucleation, growth, and venting behavior of inter-granular bubbles. Several attempts have been made to apply mesoscale methods to model the different processes associated with fission gas diffusion and release from UO_2 fuel [32-35]. While the results of these efforts are encouraging, challenges remain to demonstrate the predictive nature of applying mesoscale methods to the complexities of nuclear fuel materials because of the lack of quantifiable benchmarking of these methods.

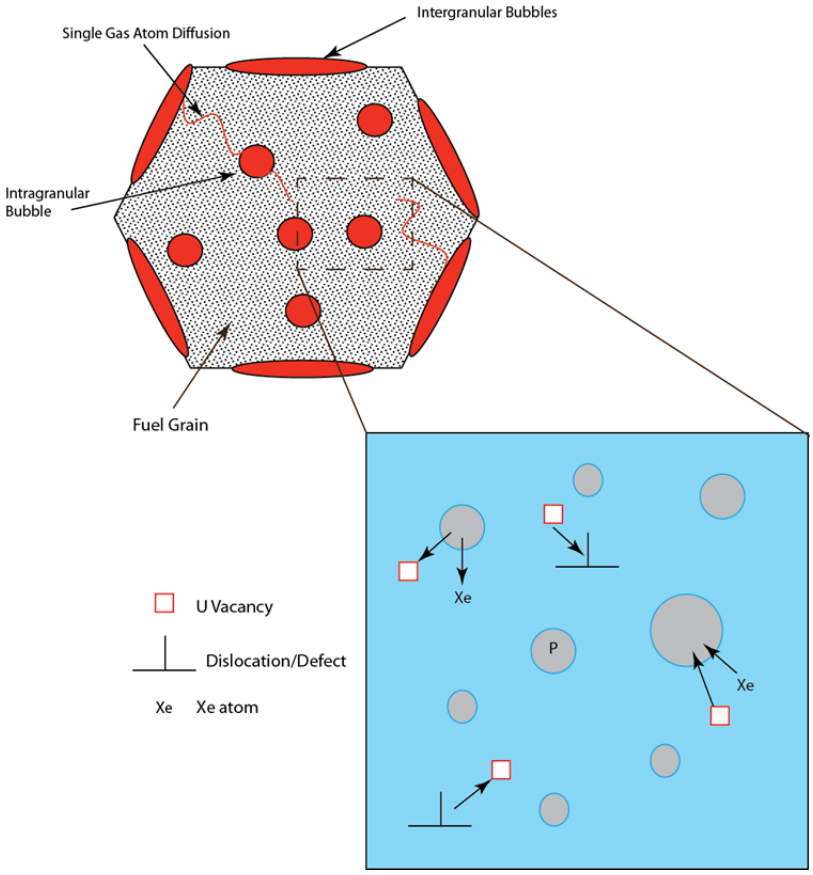

Figure 1. Schematic process of thermally induced fission gas diffusion and release from fuels.

2.2 Intra-granular Fission Gas Atom Behavior

The first step in developing mesoscale modeling for fission gas behavior in nuclear fuel is to demonstrate that the mechanisms leading to single gas atom diffusion, nucleation of intra-granular bubbles, and ultimately to calculating the flux of gas atoms reaching the grain boundary can be appropriately represented in the methods. As outline above, these mechanisms constitute the first stage in the fission

gas release process. The experiments and assessments performed to understand intra-granular fission gas behavior are reviewed below.

Intra-granular gas bubble growth kinetics have been investigated in irradiated UO_2 during thermal annealing from 800°C to 1800°C by Kashibe et al. [26]. Their results show a rapid increase in the size of the intra-granular bubbles from a mean radius of ~1 nm to a mean radius of >20 nm in less than 10 minutes after heating to temperatures of ~1800°C as shown in Figure 2. A corresponding decrease in bubble density of about 10^3 is also observed, as illustrated in Figure 3. Their results also indicate that gas bubble growth kinetics is dependent more on the burnup and proximity to grain boundaries than on the annealing temperature or heating rate. As a consequence, these results imply that structural defects such as dislocations and grain boundaries, which may act as sinks and/or sources of vacancies, interstitials, and gas atoms, play an important role in gas in the evolution of the intra-granular bubble size and density.

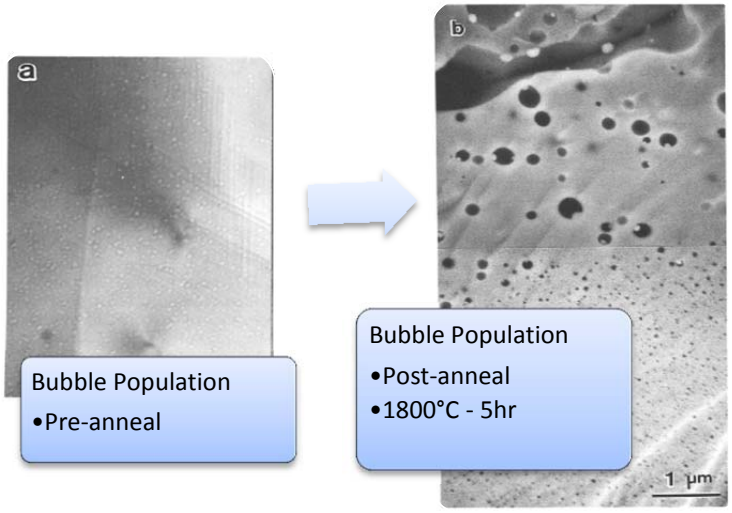

Figure 2. Intra-granular bubble behavior from Kashibe et al. [26].

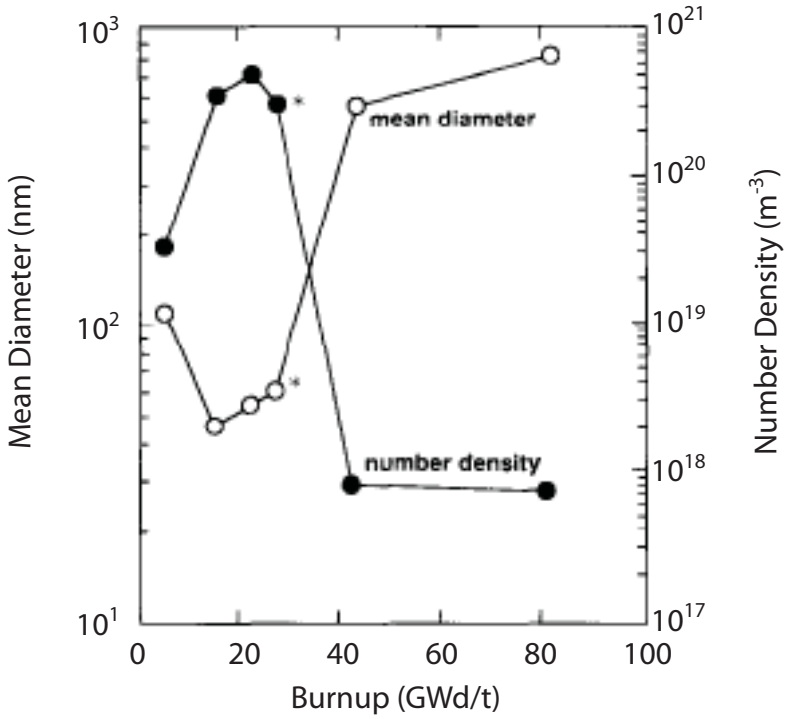

Figure 3. Burnup dependence of mean diameter and number density after annealing at 1800°C for 5 hours. (*) Annealing at 1700°C C-1800°C C for ~60 minutes [26].

White et al. [24] reported similar intra-granular gas bubble growth kinetics in post-irradiation annealing experiments with UO_2. In the experiments, specimens of UO_2 fuels were subjected to transient heating at a ramp rate of 0.5°C C/s and 20°C C/s to target temperatures between 1600°C and 1900°C. The bubble size distribution was measured from 17 specimens, which entailed the measurement of nearly 26,000 intra-granular bubbles. The major findings include the following: 1) the bubble densities decreased approximately 10^3-10^5 from the low temperature irradiation condition during annealing, independent of the annealing temperature; and 2) the bubble size distribution exhibits long exponential tails in which the largest bubbles are present in concentrations of 10^4 or 10^5 lower than the concentrations of the average sized bubbles. These results are not consistent with the presence of thermal resolution from bubbles. Under thermal annealing conditions, thermal resolution of gas atoms from the bubbles back into the matrix (or Ostwald ripening) is one possible mechanism for bubble growth and coarsening. However, because the irradiated UO_2 may be far away from equilibrium state, White et al. argued that thermal resolution is not adequate to explain the intra-granular bubble behavior in post-irradiation annealing. They suggested that 1) the bubble growth is driven by competition between vacancy sinks at the bubbles and vacancy sinks at dislocations, and 2) the bubble growth is severely restricted by vacancy starvation effects under out-of-pile conditions.

From the above mentioned experimental reports we can conclude that intra-granular gas bubble growth and coarsening under post-irradiation annealing is a complex process, due in large part to the fact that the initial system is far from equilibrium at the end of irradiation. A number of factors or material processes appear to affect the gas bubble growth kinetics. For instance, the gas bubbles formed during irradiation at low temperature have large over-pressure conditions when heated to the annealing temperature. The high

pressure within the gas bubble causes gas resolution from gas bubbles and local strain gradients. Vacancy and gas concentrations in an irradiated UO_2 matrix may also be much higher than the equilibrium concentrations. The presence of these conditions means that gas bubbles, which are larger than a critical size, will grow at the beginning of the annealing process. However, as White et al. [24] suggest, the growth in intra-ganular bubbles is terminated due to vacancy starvation caused by the different defect sink strengths for vacancies and gas atoms. Therefore, simple Ostwald ripening with a constant gas bubble volume fraction cannot describe the intra-granular gas bubble growth kinetics during post-irradiation annealing tests.

In the evaluation of the mesoscale methods, we have focused on developing a mesoscale benchmark problem to simulate the intra-granular gas bubble growth mechanisms and kinetics by taking into account the main mechanisms in the process, including vacancy and gas atom diffusion, vacancy starvation/emission, internal pressure in gas bubbles, and elastic interactions associated with lattice mismatches of distributed vacancy, gas atoms, and gas bubbles. The mesoscale methods used in this benchmark problem include the Fastest Fourier Transform in the West (FFTW)-based PF model, finite element method (FEM)-based PF model, Potts method, and kMC method. Note that different modeling methods describe the processes involved in this benchmark problem differently because of their intrinsic limitations and their current state of development, making direct comparisons of modeling results difficult. However, the simulation results obtained highlight the unique features of each method in terms of capability, numerical accuracy, and efficiency. The results of this study will help develop more efficient and accurate mesoscale methods for use in simulating microstructure evolution in nuclear material.

3. DESCRIPTION OF THE MESOSCALE BENCHMARK PROBLEM

The first phase of demonstrating the predictive capabilities of mesoscale methods for irradiated material behavior focuses on the intra-granular gas atom diffusion and gas bubble evolution kinetics in post-irradiation thermal annealing conditions. Post-irradiation conditions eliminate the complexities of dynamic fission-induced damage occurring simultaneously with the diffusion and trapping of fission gas atoms. Furthermore, the requirement to consider intra-granular bubble nucleation is removed by concentrating on post-irradiation conditions. Both of these mechanisms are difficult to incorporate in atomistic and mesoscale methods and, as such, will be deferred until later exercises.

Defining the benchmark problem includes specifying an idealized set of initial conditions, boundary conditions, and thermodynamic data that are representative of intra-granular fission gas bubbles and Xe atoms dissolved in a matrix of UO_2. Benchmark Problem 1 consists of simulating the diffusion of Xe atoms and vacancies that control the growth and coarsening of intra-granular bubbles within a grain of UO_2 material. The grain is assumed to be infinite in size to eliminate the need to consider interactions with the grain boundaries. Grain boundaries can be sinks for fission gas atoms and sources of vacancies during thermal annealing. Future benchmark problems will include grain boundary interactions.

Initial conditions for the benchmark problem were obtained from experimental measurements for gas bubble density, gas bubble size distribution, and dislocation density from Kashibe et al. [26], and a

calculation of the Xe atom concentration based on a 30% fission yield and a burnup of 23 GWd/MTU. The vacancy concentration in irradiated materials may strongly affect the bubble growth kinetics according to Olander and Wongsawaeng [21]. Because this concentration is unknown, it was treated as a specified parameter in the simulations. The gas density and pressure within the bubbles is calculated with the equation of state for Xe given by Ronchi [36], which includes the Xe gas compressibility. Table 1 lists the initial conditions for Benchmark Problem 1. A temperature ramp from 800°C to 1800°C at 2°C/sec (500-second heating time) is specified to change the conditions from the irradiated state (irradiation temperatures were ~800°C) to the thermal annealing temperature. For simplicity, we assume that 1) periodic boundary conditions (all gradients = zero) are imposed in the x-,y-, and z- directions of the simulation cell; 2) dislocation distribution, which is related to sinks and sources for vacancies and gas atoms, is uniform in the matrix; and 3) vacancy emission rate depends on the spatial distribution and density of dislocations, vacancy concentration, and mobility.

.

Table 1. Initial condition of intra-granular fission gas bubble coalescence during thermal annealing.

Description	Value
Initial bubble density [26]	$9x10^{23}/m^3$
Initial gas concentration in matrix	0.0042
Initial U/O vacancy concentration in matrix	Model parameters
Dislocation density and types [23]	$2x10^{14}/m^3$
Initial gas atom concentration in bubbles	0.7
Initial bubble distribution	Normal distribution
Mean bubble radius [26]	1 nm

The mechanisms controlling the microstructure evolution under consideration in Benchmark Problem 1 include the following:

- single gas atom diffusion;
- gas atom or vacancy trapping by defects and dislocations;
- gas atom and vacancy absorption into nanometer-sized gas bubbles;
- gas atom and vacancy resolution back into the matrix from nanometer-sized gas bubbles;
- non-equilibrium pressure conditions in gas bubbles;
- elastic interactions between defects and bubbles.

Gas bubble growth requires a supply of both vacancies and gas atoms. Starvation of either vacancies or gas atoms will limit the bubble growth. Due to the high pressure in the gas bubbles and large lattice mismatch of Xe atoms and U vacancies, elastic interaction could be an important driving force or resistance for the diffusion of vacancies and Xe atoms. Defects such as dislocations can act as either sinks or sources of vacancies. The spatial distribution and density of dislocations affect the sink or emission strength of vacancies, hence the concentration of vacancies. Each of the mesoscale methods

must take these physics into account in order to appropriately represent the microstructure evolution of intra-granular fission gas.

3.1 Thermodynamic and Kinetic Properties of Defects in UO_2

This section briefly reviews the thermodynamic and kinetic properties defined for the benchmark problem. Table 2 lists the thermodynamic data used in the problem. Details can be found from appendix E.

3.1.1 Oxygen interstitials and vacancies

From both simulations [4, 37, 38] and experiments [39-41] it is clear that oxygen (O) vacancies and interstitials move several orders of magnitude faster through the UO_2 lattice than cations or fission gases. The migration barriers for anion vacancies and interstitials are ≈0.5 [39, 42] and ≈0.9-1.3 eV [39, 42, 43], respectively, while the lowest barrier for cations (a cluster of two U vacancies that can form under irradiation) is predicted to be 2.6 eV [4] and the barrier for migration of single U vacancies is 4.5-4.8 eV [4, 38].

3.1.2 Uranium interstitials and vacancies

Migration of U interstitials was recently investigated using DFT calculations [38] and the barrier was calculated to be 3.7 eV for the indirect interstitial mechanism, which is lower than the barrier for single U vacancies but about 1 eV higher than for clusters of U vacancies (see below). Under thermal equilibrium conditions the contribution from interstitials to cation diffusion is very small due to the negligible concentration of such defects compared to vacancies [38]. The activation energy for the U interstitial diffusion mechanism in stoichiometric UO_2 was calculated to be as high as 15-16 eV [38].

Experiments typically quote 2.4 eV as the migration barrier of U ions via a vacancy mechanism [40, 41], which was derived by studying the recovery of UO_2 samples exposed to irradiation. If non-equilibrium clusters form under such conditions the measured barrier could refer to, for example, the migration of U vacancy clusters rather than isolated vacancies. This was confirmed by recent DFT calculations, which predicted a barrier of about 4.5-4.8 eV for single U vacancies and about 2.6 eV for two nearest neighbor U vacancies [4]. Even though the agreement between theory and experiments was rather good [4], the model used for calculating the activation energies from the calculated thermodynamic and kinetic data was incomplete. The most up to date activation energy for U diffusion in UO_2 is 4.4 eV [44] and 4.1-4.9 eV [38]. The effective value of the U vacancy formation energy, 2.69 eV, which depends on stoichiometry and chemical environment, was suggested for strictly stoichiometric UO_2.[4]

3.1.3 Fission gas

Miekeley and Felix [45] performed early experiments on the release of Xe during post-irradiation diffusion annealing from $UO_{2\pm x}$ with a range of different stoichiometry (x). Perhaps the most striking conclusion from their work was that the activation energies for release exhibited unique values in the

UO_{2-x} (6.0 eV), UO_2 (3.9 eV), and UO_{2+x} (1.7 eV) regimes, respectively, while they were almost constant within each of these composition sets.

The DFT+U methodology was used to study the diffusion of Xe under a variety of conditions [4]. Particularly, the thermodynamic model originally derived by Catlow [1] is applied to calculate activation energies for Xe in the UO_{2-x}, UO_2, and UO_{2+x} ranges. This transport model requires calculation of the binding energy of a second U vacancy to the Xe trap site and the barrier for moving one of the constituent U vacancies to another location such that net transport is enabled. This diffusion mechanism involves three components: the U vacancy formation energy, the binding energy of this vacancy to the Xe trap site, and the intra-cluster migration barrier for the individual U vacancies bound to this cluster. That is, the rate-limiting step is not Xe motion within the cluster, but the migration of the second vacancy within the cluster; without the motion of the second bound U vacancy Xe does not diffuse. The barriers for moving one of the U vacancies from one part of the Xe trap site to another is 3.91, 5.00, and 5.51 eV for the XeU (Xe occupies one U vacancy), XeUO (Xe occupies one U and one O vacancy) and $XeUO_2$ (Xe occupies one U vacancy and two O vacancies) trap sites, respectively. The corresponding defect formation energies of XeU is 4.35 eV for strictly stoichiometric UO_2 [4].

Fission gases can also diffuse via interstitial mechanisms. Due to the large size of Xe atoms, however, it is unlikely that such mechanisms are important at high temperature because the interstitial Xe atoms would quickly recombine with U vacancies. If the Xe atom stays in interstitial positions it may diffuse with a rather low barrier (1.6 eV) compared to vacancy mechanisms [46].

In summary, the diffusions of Xe atom and U vacancy in are very complicated processes. The activation energy of defects strongly depends on the diffusion mechanisms, irradiation environment or thermal concentration of defects, and the deviation from thermodynamic equilibrium. Considering the fact that 1) O vacancy and interstitials have much higher mobility than the U vacancy and Xe atom; 2) the concentration of U interstitials is negligible compared to the U vacancy concentration under thermal equilibrium conditions, it can be assumed that the gas bubble evolution is controlled by U vacancy and Xe atom diffusion. We further assume that U vacancy diffuses through vacancy-complex diffusion mechanisms, while Xe diffuses by interstitial mechanisms in a vacancy-starvation environment and by vacancy-complex diffusion mechanisms. Table 2 lists the thermodynamic and kinetic properties of single defects, and defect complex in stoichiometric and non-stoichiometric UO_2. The formation volumes of defects were calculated according to the definition of the corresponding defect formation energies by Andersson et al. [4].

Table 2. Thermodynamic and kinetic properties of defects in $UO_{2\pm x}$.

Description	Value
Xe interstitial migration energy in UO_{2-x}	1.6~6.0 eV
U_V/O_V/Xe complex migration energy	3.91~5.51 eV
Xe interstitial formation energy	3.~4.35 eV
U vacancy formation energy	2.69 eV
Formation volume of O vacancy	1.79 [$Å^3$]

Formation volume of U vacancy	42.3 [$Å^3$]
Formation volume of Schottky defect (unbound)	45.8 [$Å^3$]
Formation volume of Schottky defect (bound)	41.9 [$Å^3$]
Formation volume of Xe	52.8 [$Å^3$]
Interfacial energy of gas bubbles	0.6 J/m^2
Elastic constants C_{11}, C_{12} and C_{44} of UO_2 [47, 48]	395 GPa, 121 GPa, 64 GPa

3.2 Assessment of the Thermodynamic Parameters

Based on classical nucleation theory, chemical free energy, elastic energy, and interfacial energy determine the critical size of gas bubbles. As a means to ensure that the Benchmark Problem was specified in a manner that would yield results that are consistent with experimental observations, a simplified PF analysis was performed to evaluate the effect of concentration and elastic interaction on the critical size of the fission gas bubbles. In the checkout simulation, a gas bubble with different sizes is embedded at the center of a three-dimensional (3-D) simulation cell $96\Delta x \times 96\Delta y \times 96\Delta z$. Periodic boundary conditions in the x-, y-, and z- directions are imposed on the model and the simulation is performed at 2100 K. Four different cases were evaluated: Xe matric concentrations of 0.001 and 0.0042 and with and without elastic interaction. The time evolution of the gas bubble radius is plotted in Figure 4(a), which shows that a gas bubble with a radius less than 0.4 nm shrinks for all four cases. When the radius of the gas bubble is larger than 0.8 nm the gas bubble grows in all four cases. Gas bubbles with radii between 0.4 nm and 0.8 nm may grow or shrink depending on the concentration and elastic interaction. Therefore, the critical size of gas bubble is about 0.8 nm for the given free energy, interfacial energy, and elastic interaction energy components used in this analysis. The results shown in Figure 4(a) indicate that the critical bubble size increases with decreasing vacancy and Xe concentrations. Pressure and shear stress distributions on the x-y planes that cross the center of the gas bubble are presented in Figure 4(b). The calculated pressure inside the gas bubble is about 1.6 GPa, which is consistent with the equation of state. In addition, the pressure inside the gas bubble causes a long-range elastic field near the gas bubble, which may affect the gas bubble growth kinetics as well as the critical size of the gas bubble during coarsening. The results in Figure 4(a) show that the elastic interaction increases the critical size of the gas bubble.

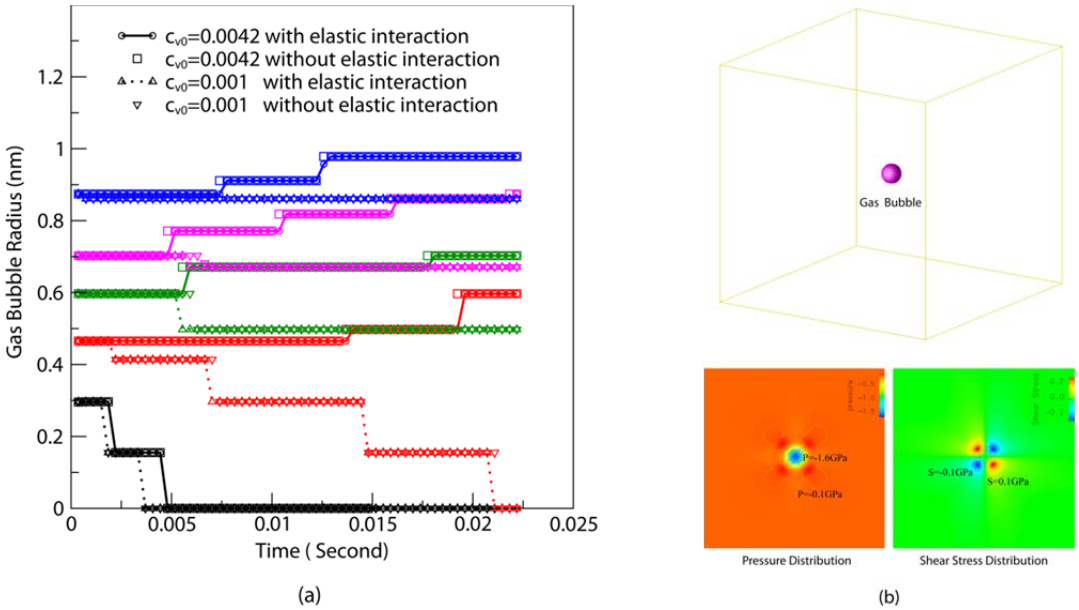

Figure 4. (a) Concentration and elastic interaction dependence of gas bubble critical size, and (b) pressure and shear stress around the gas bubble.

4. SUMMARY OF MESOSCALE METHODS AND BENCHMARK PROBLEM RESULTS

4.1 Mesoscale Methods

During the past few decades different modeling methods—from atomistic, meso- and macro-scales, including ab initio, MD, kMC, objective kMC, discrete dislocation dynamic, rate theory, crystal plasticity, micro-mechanic, and macro-mechanic methods—have been developed to study microstructure and property evolution in irradiated materials. One of the grand challenges in multi-scale modeling is the lack of physics-based modeling methods that enable the prediction of 3-D microstructure evolution in the mesoscale. At the mesoscale, the time and length scales are much larger than those of atomistic simulations, and much smaller than those of macroscale methods. The typical mesoscale time scale is from seconds to a few hours, and the typical length scale is from nanometers to several tens micron meters. The mesoscale PF approach, which is informed by the thermodynamic and kinetic properties of the system from atomistic simulation and experiments, is a mesoscale modeling method. This method has been successfully used in predicting 3-D microstructure evolution such as solidification, grain growth, martensitic transition [49], precipitation, ferroelectric/ferromagnetic transition [50], dislocation dynamics, deformation twin, and sintering [51]. The advantages of the PF approach are that 1) making assumptions of microstructure morphology is not needed; 2) explicitly tracking the interface and topological changes compared to sharp interface methods is not needed; and 3) The continuous description of energy landscape makes it convenient to take into account of both short-range and long-range interactions. The Potts kMC method is another mesoscale modeling method that is based on statistic mechanics and populates a lattice with an ensemble of discrete particles to represent and evolve the 3-D microstructure.

The particles evolve in a variety of ways to simulate microstructural changes. The kMC methods have proven themselves to be versatile, robust, and capable of simulating various microstructural evolution processes. They have the advantage of being simple and intuitive, while still being rigorous methods that can incorporate all of the thermodynamic, kinetic, and topological characteristics to simulate complex processes. They are easy to code, readily extendable from two dimensions to three dimensions (2-D to 3-D), and can simulate the underlying physics of many materials evolution processes based on the statistical-mechanical nature of the model. These processes include curvature-driven grain growth [52, 53], anisotropic grain growth [54], recrystallization [55], grain growth in the presence of a pinning phase [56, 57], Ostwald ripening [58-60], and particle sintering [11, 61-63].

The following sections describe the mesoscale approaches used to simulate the intra-granular gas bubble evolution in Benchmark Problem 1. The description includes a short summary of the modeling/mathematical approach, assumptions, and key input variables. A more detailed description is included in Appendixes. A collection of the results and comparison of the different methods is presented in Section 4.2.

4.1.1 Phase-field model used by PNNL

4.1.1.1 Key assumptions

a) Gas bubble growth needs continuously supply of U/O vacancies and Xe atoms. Xe atoms may occupy a U vacancy lattice or interstitial lattice, which one depends on valid U vacancy and Xe concentrations. For the simplicity of description, we assume that Xe atoms occupy interstitial lattices. Thus, the XeU (Xe occupies one U vacancy) is described by a cluster of a U vacancy and an interstitial Xe atom. Therefore, a two-sublattice model is used to describe the vacancies and Xe atoms, which allow one to study the effect of vacancy starvation and vacancy emission on gas bubble growth.

b) Xe interstitial, U vacancy, and the XeU (Xe occupies one U vacancy) have very different mobilities, as reviewed in Section 3.1. In addition, other complexes such as XeUO (Xe occupies one U and one O vacancy) and $XeUO_2$ (Xe occupies one U vacancy and two O vacancies) are also mobile and contribute to the diffusion of vacancies and Xe atoms. So the effective mobilities of U vacancies and Xe atoms are used in the model. In the present simulations the effective migration energy, 3.9 eV, for both U vacancy and Xe atom is used, but different mobilities of U vacancies and Xe atoms can also be used.

c) Gas bubbles formed during low temperature irradiation may be unstable at annealing temperature. So the initial size distribution of gas bubbles may dramatically affect the results of gas bubble size and density evolution. In our simulations, a normal (Gaussian) distribution with a mean radius of 1 nm and standard deviation of 1 nm is used to generate the initial gas bubble size distribution.

d) Chemical potential gradient is one driving force for vacancy and Xe diffusion. Kim's model [37] is used to describe the chemical free energy of matrix and gas phases. To efficiently solve the PF

evolution equation, we use two parabolic functions to approximate the ideal solution free energy of the matrix with vacancies and Xe atoms and the free energy of the gas bubble phase, which is calculated from the equation of state.

e) Dislocations are sinks or sources of vacancies. Because of the lack of sink and emission strengths, the emission rate of vacancies from dislocations is taken as a model parameter in the simulations.

f) Experiments [24] suggested that vacancy emission could be an important mechanism that affects the gas bubble evolution kinetics. Therefore, we assumed that the initial vacancy concentration is a model parameter.

g) O vacancy has much higher mobility than the U vacancy and Xe atom. But it is not a rate-limiting species in gas bubble growth. Therefore, we neglected O vacancies. Its effect is accounted for in the effective diffusivity of U vacancies and Xe atoms.

h) The contribution of small gas bubble migration at high temperature to gas bubble evolution is ignored in this model. However, a PF model of void migration can be extended to describe gas bubble migration [34, 64].

4.1.1.2 Description of the model

Three field variables—U vacancy concentration $c_v(\mathbf{r},t)$, Xe concentration $c_g(\mathbf{r},t)$, and order parameter $\eta(\mathbf{r},t)$—are used to describe the microstructure, including the spatial distributions and time evolution of gas bubbles, U vacancies, and Xe atoms. Inside the gas bubbles, vacancy concentration is 1 (i.e., $c_v(\mathbf{r},t)=1$); gas concentration is 0.7 (i.e., $c_g(\mathbf{r},t)=0.7$), which is calculated from the equation of state of Xe gas phase; and the order parameter is 1 (i.e., $\eta(\mathbf{r},t)=1$). Outside the gas bubble, the concentrations of the vacancy and Xe atom and the order parameter are $c_v(\mathbf{r},t)$, $c_g(\mathbf{r},t)$, and 0, respectively. The lattice mismatches $\varepsilon_{ij}^{*}(\mathbf{r},t)$ associated with distributed U vacancies and Xe atoms, and the internal pressure inside gas bubbles are described by a stress-free tensor. The initial vacancy concentration c_{v0} and vacancy emission rate $\dot{\omega}$ from distributed dislocations are used as model parameters in the simulations.

Assuming that the microstructure evolution is driven by the minimization of total energy of the system, the evolution equations can be described by the Chan-Hilliard and Allen-Cahn equations[65, 66]:

$$\frac{\partial c_v}{\partial t}=\nabla\cdot\left\{M_{vv}\nabla\left(\frac{\partial\left(F+U^{def}\right)}{\partial c_v}\right)\right\}+\dot{\omega}(\rho_{dis},c_v,\sigma_{ij}), \tag{1}$$

$$\frac{\partial c_g}{\partial t}=\nabla\cdot\left\{M_{gg}\nabla\left(\frac{\partial\left(F+U^{def}\right)}{\delta c_g}\right)\right\}, \tag{2}$$

$$\frac{\partial \eta}{\partial t}=-L\left(\frac{\partial F}{\partial \eta}+\frac{\partial U^{def}}{\partial \eta}-\kappa^2\nabla^2\eta\right), \tag{3}$$

where M_{vv} and M_{gg} represent the mobility of vacancies and gas atoms; F and U^{def} are chemical free energy density and elastic energy density, respectively; κ is the gradient coefficient; L is the interface mobility coefficient; and $\dot{\omega}(\rho_{dis,}c_v,\sigma_{ij})$ is the vacancy emission rate which usually depends on dislocations ρ_{dis}, local stress σ_{ij}, and vacancy concentration $c_v(\mathbf{r},t)$.

With the input of initial gas bubble density, gas bubble size distribution, gas concentration, and annealing conditions, the evolution equations are solved by the implicit FFTW method [67], which was proved to be an efficient numerical method. The effect of initial vacancy concentration, vacancy emission, elastic interaction, and annealing conditions on gas bubble evolution kinetics is simulated in 2-D and 3-D.

The PF model describes the following mechanisms:

- diffusion of U vacancies and Xe atoms;
- absorption and dissolution of vacancies and Xe atoms at gas bubbles;
- vacancy emission from distributed dislocations;
- elastic interaction among gas bubbles, vacancies, and Xe atoms;
- gas bubble growth;
- gas bubble coalescence.

4.1.2 Phase-field model used by INL

4.1.2.1 Key assumptions

a) Xe atoms in the UO_2 lattice tend to be located within a Schottky defect composed of one U vacancy and two O vacancies. Also, at high temperature, the Xe is transported through vacancy diffusion. Therefore, the Xe atom is assumed to occupy a U vacancy.

b) Sufficient, fast-moving U/O vacancies are assumed to be present in the material such that Xe is the only rate-limiting species. Thus, the kinetics could be captured by only representing the Xe atoms in the model. In addition, the model does not consider the Brownian motion of the bubbles, and therefore primarily considers bubble growth due to Ostwald ripening.

c) The effect of the pressure could have a significant effect on the early stages of the bubble growth. However, as the bubbles grow, the pressure will decrease and the effect of pressure will become less significant. To simplify the simulations, the effect of pressure is ignored.

d) An eighth-order polynomial free energy is used to approximate the free energy:

$$F = k_b T(c_g \ln c_g + (1-c_g)\ln(1-c_g)) + wc_g(1-c_g), \quad (4)$$

where *w* is assumed to equal the formation energy of Xe in the UO_2 matrix (~4.35 eV).

4.1.2.2 Description of the model

One field variable—Xe atom concentration—$c_g(\mathbf{r},t)$ is used to describe the microstructure of gas bubbles and Xe distribution in the UO_2. Inside the gas bubble, gas concentration is assumed to be 1.0 (i.e., $c_g(\mathbf{r},t)=1.0$). Outside the gas bubble, Xe concentration is $c_g(\mathbf{r},t)$. The microstructure evolution is described by the Cahn-Hilliard equation [65]:

$$\frac{\partial c_g}{\partial t} = \nabla \cdot M\nabla\left(\frac{\delta(E)}{\delta c_g}\right) = \nabla \cdot M\nabla\left(\frac{\partial F}{\partial c_g} + \frac{\kappa}{2}\nabla^2 c_g\right), \tag{5}$$

where M represents the mobility of gas atoms, E is the total energy of the system, F is chemical free energy density, and κ is the gradient coefficient, which is determined by interfacial energy.

To solve the PF equations, the FEM is used to discretize the domain. In addition, we use implicit time integration. Thus, the Cahn-Hilliard equation (5) must be expressed as a residual equation and be converted to a "weak" form,

$$\begin{aligned} \mathrm{R}(c_g) = & \quad \frac{\partial c_g}{\partial t} - \nabla \cdot M\nabla\left(\frac{\partial F}{\partial c_g} + \frac{\kappa}{2}\nabla^2 c_g\right) = 0 \\ = & \left(\frac{\partial c_g}{\partial t}, \phi_i\right) + \left(M\nabla\frac{\partial F}{\partial c_g}, \nabla\phi_i\right) + \left(\frac{\kappa}{2}\nabla^2 c_g, \nabla\cdot\left(M\nabla\phi_i\right)\right) \end{aligned} \tag{6}$$

where the boundary terms are not shown. Due to the second-order derivative in the weak form, this system must be discretized using higher-order elements. In the simulations, the third-order Hermite element is used. Note that more information about solving the PF equations using the MARMOT framework can be found in the articles by Tonks et al. [68].

The PF model is able to describe the following mechanisms:

- diffusion of Xe atoms
- absorption and dissolution of Xe atom at gas bubbles
- gas bubble growth
- gas bubble coalescence

4.1.3 Potts model used by SNL

4.1.3.1 Key assumptions

a) During irradiation of LWR fuels, Xe atoms are formed due to fission of U. Xe has extremely low solubility in UO_2, estimated to be an order of magnitude of 10^{-10}. It is thought that the Xe atom present in the UO_2 lattice has associated with it a large strain energy field as it "stuffs" itself into the UO_2 lattice. Thus, under irradiation conditions, the Xe atom will precipitate out onto almost any imperfection or feature to which it can attach. Furthermore, once Xe atoms start to precipitate to form bubbles, more Xe will precipitate to enlarge the bubble. The exact behavior and details of these events will be dictated by the local temperature, fission rate density, and the local defect density [69].

b) The irradiated fuel contains bubbles under high pressure. When the fuel is heated to 1800°C, smaller bubbles dissolve at higher temperature and can impact the result of gas bubble size and density distributions.
c) The remaining bubbles grow by Ostwald ripening type mechanism. They can also grow by random walk and coalescence, but only the very small bubbles random walk sufficient distances to give growth by coalescence.
d) Diffusion is simulated by a random walk of pixels. Only diffusion of Xe atoms is considered in this simulation as it is assumed to be the rate limiting step; however, U and O diffusion can easily be incorporated into the Potts kMC model.
e) Chemical potential gradients are one of the driving forces for bubble growth. This is inherent to the Potts model as gradients in the ensemble composition simulate this gradient.
f) Two- and multi-component system with low solubility and with one phase of very low volume fraction, as is the case in this simulation, is computationally expensive for the Potts model. The hybrid model is being developed to address this issue and some other limitations.

4.1.3.2 Description of the model

One field variable—spin $q(\mathbf{r},t)$—is used to describe the microstructure in UO_2 in the Potts digitization scheme. All lattice sites are filled with the same integer value of spin = 5, which designates all the sites as belonging to a single grain. Gas atoms are placed in the simulation space at random locations to match the desired volume fraction and have a spin = 3. In the Potts model bobbles coarsen by randomly walk and coalescence, and by the gas in the bubbles dissolving back into the lattice and re-precipitating out on other bubbles. During each Monte Carlo step, each bubble site attempts to exchange places with one of its neighboring sites chosen at random from its 26 neighboring sites. If the chosen neighboring site happens to be a grain site, then the change in energy ΔE is evaluated by

$$E = \frac{1}{2}\sum_{i=1}^{N}\left[F_i + U_i + \sum_{j=1}^{26} J\left(1-\delta(q_i,q_j)\right)\right], \tag{7}$$

where U_i is the strain energy density for site i, $U_i = \frac{P_{o,i}^2 l^3}{2E}$ in the solid lattice, and $U_i = P_{o,i} l^3$ in the gas bubble. $P_{o,i}$ is the pressure at site i, which has volume l^3. F_i is the bulk free energy of the material at site i and is a function of the local composition and temperature. The standard Metropolis algorithm is used to determine whether the attempted exchange is executed or not. Boltzmann statics are used to calculate the probability W of the exchange.

$$W = \begin{bmatrix} 1 & \Delta E \le 0 \\ \exp\left(\frac{-\Delta E}{k_B T}\right) & \Delta E > 0 \end{bmatrix}. \tag{8}$$

In this way, all the materials transport mechanisms that are active in bubble coarsening are simulated.

For simplicity and because no more details are available, F_i and U_i are assumed to be the following. F_i is assumed to be only due to the entropy of mixing of the two components, UO_2 and Xe gas. U_i is assumed

to be constant. This is true within the bubble, but not so in the lattice. However given the stress state in lattice, the Potts model can easily incorporate the lattice stress effects using equation (7).

The Potts model is able to simulate the following mechanisms:

- diffusion of Xe atoms;
- absorption and dissolution of Xe atom at gas bubbles;
- gas bubble growth;
- gas bubble coalescence.

4.1.4 kMC model used by ORNL

4.1.4.1 Key assumptions

a) All the gas atoms reside inside the bubble sites; there is no solubility of Xe in the matrix during annealing.

b) The bubble sites are initially at equilibrium, that is, the pressure exerted by the gas atoms inside the bubble elements balances the surface tension of the bubble-matrix interface. Therefore, there are no long-range stress fields in the matrix associated with pressurized bubbles.

c) The system largely evolves by random migration of the bubbles driven by the surface diffusion of U atoms based on an exchange between the void sites and the matrix sites. When two bubbles coalesce, the pressure equilibrium is violated. Restoring the equilibrium occurs by the pressurized bubbles acquiring a void site.

d) The exact mechanism by which the non-equilibrium bubbles acquire void sites is not modeled rigorously; it is assumed that the probability of acquiring a void is proportional to the energy change associated with creating additional void-matrix interface.

e) The effect of matrix dislocations and fission fragments on pinning bubble motion is considered by introducing a fraction of pinning sites in the simulation volume.

4.1.4.2 Description of the model

Three elements—matrix volume element, void element, and bubble element—are used to describe the microstructure in UO_2. The Potts/kMC model developed at ORNL is based on the simulation approach published recently by Suzudo et al. [70]. The mesoscale simulation domain consists of three "species"—the matrix volume elements that are made of UO_2, "void" volume elements that are made up of a collection of condensed vacancies (green), and "bubble" elements that consist of a collection of vacancies and gas atoms (red). The formation of larger "extended bubbles" occurs through a collection of voids and bubble sites. The simulation approach defines three types of Monte Carlo moves:

- exchange of a void and a matrix site to simulate surface diffusion;
- exchange of a void and a bubble site to simulate Xe diffusion inside the bubble;
- creation or destruction of a void site at the bubble-matrix interface.

In the kMC simulations, the flip of sites associated with the three MC moves is made as usual according a probability given by

$$p = \begin{bmatrix} 1 & \Delta E \le 0 \\ \exp\left(\frac{-\Delta E}{kT}\right) & \Delta E > 0 \end{bmatrix}, \quad (9)$$

where ΔE is the change in energy associated with the flip and kT is the reduced lattice temperature. The Hamiltonian for the system, in the absence of dissolved gas atoms and long-range volume diffusion and concentration gradients, reduces to the surface energies of the various moving interfaces. The first step in the calibration process is to obtain the relationship between kT in equation (9) and K_bT_R where K_b is the Boltzmann constant and T_R is the real temperature in Kelvin. In the model, "pinning sites" inside the matrix to account for the drag on the migrating bubbles due to dislocations or fission fragments is considered.

The Potts /kMC model is able to simulate the following mechanisms:

- surface diffusion of Xe atom and vacancy;
- dislocation pinning;
- gas bubble growth;
- gas bubble coalescence.

4.2 Summary of Different Methods and Simulation Results

The mesoscale methods described in Section 4.1 are used to simulate the intra-granular gas bubble growth kinetics in post-irradiation annealing. Due to the difference in microstructure description in different models, slightly different initial conditions and thermodynamic and kinetic properties are used in the simulations. Table 3 and Table 4 summarize the used inputs. The computational effort and mechanisms considered in the different models are listed in Table 5 and Table 6 for the sake of comparison. In this section, we present the main results obtained from the different simulation methods.

Table 3. Initial condition used in simulations.

Description	PNNL	INL	SNL	ORNL
Initial bubble density [26]	$9x10^{23}/m^3$	$9x10^{23}/m^3$	$9x10^{23}/m^3$	$9x10^{23}/m^3$
Initial gas concentration in matrix	0.0042	0.005	.0042	0.0
Initial U/O vacancy concentration in matrix	0.001~0.0042		~.003	0.0 – all vacancies condense into voids/bubbles
Dislocation density and types [23]	$2x10^{14}$ /m^3			Qualitative – see report
Initial gas atom concentration in bubbles	0.7	1.0	.0015	39.56 cc/mole
Initial bubble distribution	Normal	Uniform	Normal	Single sites with diameter

	distribution of radius	distribution of radius	distribution of volume	of 2.0 nm
Mean bubble radius[26]	1 nm	1 nm (2-D) and 1.5 nm (3-D)	0.8 nm	1nm

Table 4. Thermodynamic and kinetic properties of defects in UO_2 used in simulations.

Description	PNNL	INL	SNL	ORNL
Xe migration energy in UO_2	3.9, 4.5 eV	3.9 eV		Surface diffusion dominated by U – 2.66 eV
U_V/O_V/Xe complex migration energy	3.9, 4.5 eV		constant	
Xe formation energy	3.0 eV	4.35 eV	0.7 eV	
U vacancy formation energy	3.0 eV			
Formation volume of O vacancy				
Formation volume of U vacancy	42.3 [Å^3]			
Formation volume of Schottky defect (unbound)				
Formation volume of Schottky defect (bound)				
Formation volume of Xe	50.15 [Å^3]			
Interfacial energy of gas bubbles	0.6 J/m^2	4.2~4.4J/m^2		1.0 J/m^2
Critical gas bubble size	0.8 nm		No need. Is inherent.	
Elastic constants C_{11}, C_{12} and C_{44} of UO_2	395 GPa, 121 GPa, 64 GPa		No elastic strain energy	

Table 5. Computation efforts made in the simulations.

Description	PNNL	INL	SNL	ORNL	Experiments
Temperature const. (C)/ramp (R)	C/R	R	C	C	C/R
Mean bubble radius	x	x	x	x	x
Bubble density	x	x	x	x	x

Simulation cell	256x256 (2-D) 128x128x36 (3-D)	Adaptive mesh	500x500x500 (3-D)	300x300x30 (3-D)	
Physical domain	256x256 (nm^2) 128x128x36(nm^3)	300x300 (nm^2) 20x20x20 (nm^3)	100x100x100 (3-D) (nm^3)	600x600x60 (3-D) (nm^3)	
Adaptive time		x			
Adaptive grids		x			
No. of cores	1 (2.66 GHz)	64 (2.4 GHz)	100	64, 512	
CPU time	260 h	38.5 h	24 h	22.4 h	
Simulated time	12 min (R)	9.06 min (R)	0.58 sec	40 sec	5 h
Total time steps	$2.8x10^7$	19,348	$1.8x10^6$		

Table 6. Mechanisms considered in the simulations.

	PNNL	INL	SNL	ORNL
Xe gas diffusion	x	x	x	
Vacancy diffusion	x		x	
Bubble migration			x	x
Gas bubble growth	x	x	x	x
Ostwald ripening	x	x	x	x
Vacancy emission	x			
Dislocation pinning				x
Gas bubble pressure	x		x	x
Elastic interaction	x			

4.2.1 Results from PNNL's phase-field modeling

4.2.1.1 Evaluation of the thermodynamic model by testing gas bubble evolution kinetics in 3-D at 2100 K

As shown in Figure 4, we have validated that the PF model with the thermodynamic properties, including chemical free energy, interfacial energy and elastic energy, predicts 1) the critical size of gas bubble is about 0.8 nm; 2) the critical size increases with the decrease of vacancy and Xe concentration; 3) the pressure inside the gas bubble is about 1.6 GPa, which is consistent with the equation of state; and 4) the

elastic interaction increases the critical size of gas bubble. All the results are reasonably acceptable. Here we test gas bubble growth kinetics at constant temperature 2100 K in 3-D. The simulation started with a random gas bubble distribution in a simulation cell 128x128x36 grids with gas concentration of 0.0042, different vacancy concentration of 0.001 or 0.0042, and with elastic/without elastic interaction. The results are presented in Figure 5. The gas bubble evolution can be divided into three stages as marked in Figure 5(b). In the first stage, gas bubbles with sizes smaller than the critical size quickly dissolve; in the second stage gas bubble growth is due to super saturation of the vacancy and Xe atom in the matrix; and in the third stage the gas bubble is coarsening (Ostwald ripening). The sharp decreases of the gas bubble number and gas bubble volume fraction at an early stage corresponds to the first stage, as shown in Figure 5(a,b,c). The ensuing increase of gas bubble volume fraction and constant or slowly decreasing gas bubble number corresponds to the second growth stage. During a perfect growth stage, it is expected that the number of gas bubbles keep constant. However, simulation results show that the number decreases slowly. The reason for this could be inhomogeneous spatial distribution of initial gas bubbles, which causes local Ostwald ripening in an early time. Although the modeling has not yet reached the final Ostwald ripening stage, the thermodynamic model indicates that the gas bubble volume fraction should remain constant while the number of gas bubble decreases slowly. In addition, 1) the gas bubble density reduces faster with decreasing vacancy concentration and 2) elastic interaction speeds up the reduction of gas bubble density shown in Figure 5(a,b). These results are consistent with their effect on the critical size of gas bubbles.

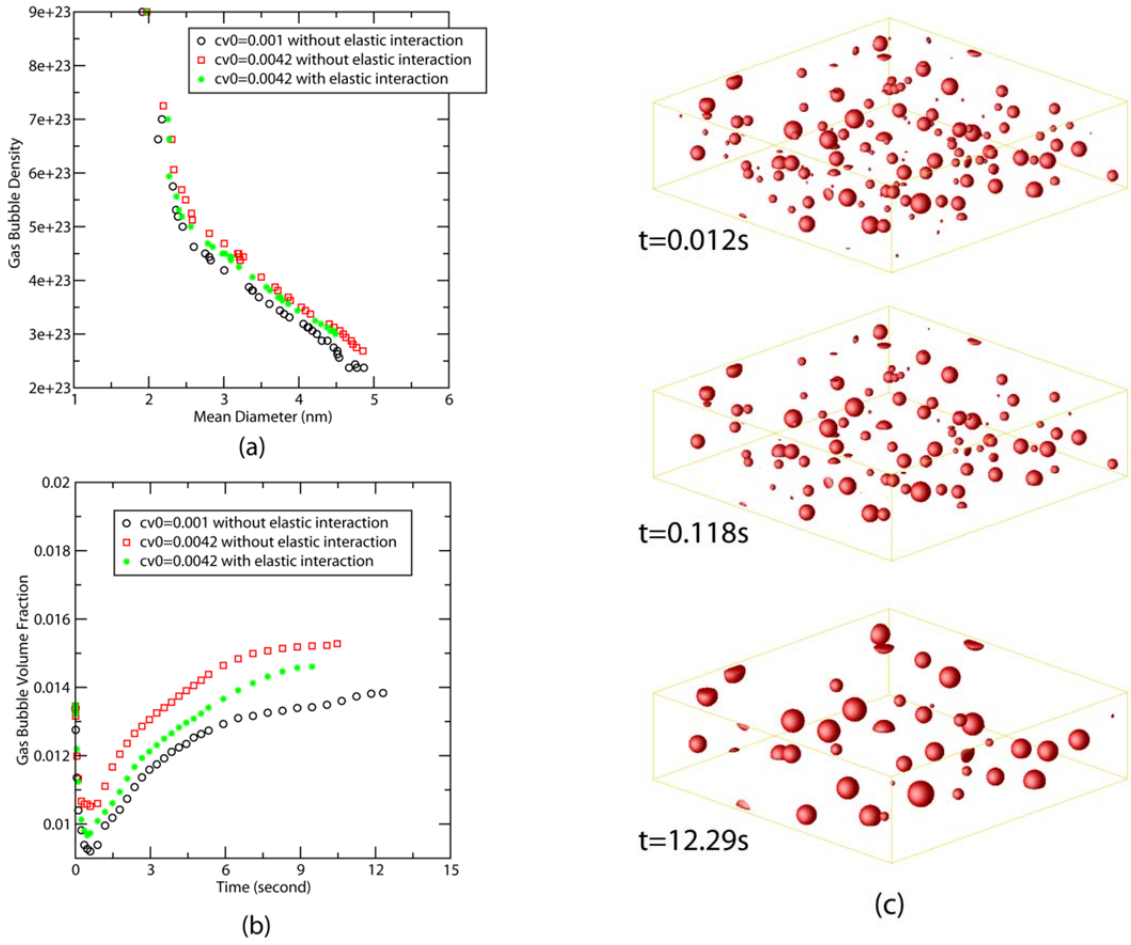

Figure 5. (a) Gas bubble density in a function of gas bubble mean diameter, (b) gas bubble volume fraction vs time, and (c) time evolution of gas bubble morphology for the case $c_{v0} = 0.001$ with elastic interaction.

Kashibe et al. [26] found that a linear relationship between the double logarithmic bubble number density and mean bubble diameter fit well their experimental data:

(10) $$\log N_b = -2.6 \log d_b + 25.1 \quad \text{or} \quad \log N_b = \log(d_b)^{-2.6} + 25.1,$$

where N_b is bubble density in a cubic meter volume and d_b is mean bubble diameter. Figure 6 plots the fitted experiment results and our simulation results. The simulation results also show a linear relationship between the double logarithmic gas bubble density and mean gas bubble diameter, but in a different slope. One reason for the slop difference between the results from experiments and simulations could be due to different initial gas bubble density and size distribution. A 2-D result in INL's PF modeling shows that the slope strongly depends on an initial gas bubble density. The slop reaches the experimental one with the increased initial gas bubble density. Reducing vacancy concentration makes the slope closer to the experimental relationship.

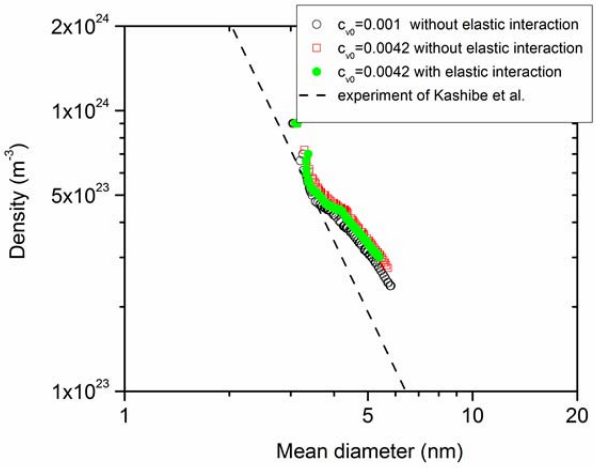

Figure 6. Gas bubble density in a function of gas bubble mean diameter.

4.2.1.2 Effect of vacancy emission on gas bubble evolution in 2-D at 2100 K

Experiments [7] suggested that gas bubble growth is severely restricted by vacancy starvation effects under out-of-pile conditions. The effect of vacancy concentration and vacancy emission from dislocations on gas bubble evolution was simulated. The simulations considered two cases. One was homogeneous vacancy emission. In this case, there was uniform vacancy generation with a generation rate $\dot{\omega} = \omega_0^2 \rho$ where ρ is dislocation density and ω_0^2 is emission strength. In the other case was, inhomogeneous vacancy emission, the vacancy emission was from individual dislocation with an emission rate $\dot{\omega} = \omega_0^2$ at dislocations. Figure 7 shows the snap shots of the gas bubble morphology at t=2 minutes.

The results confirmed that vacancy emission from dislocations leads to a faster growth of gas bubbles near dislocation, as shown. This may explain the experimental observation [7] that the bubble size distribution exhibits long exponential tails in which the largest bubbles are present in concentrations of 10^4 or 10^5 lower than the concentrations of the average sized bubbles.

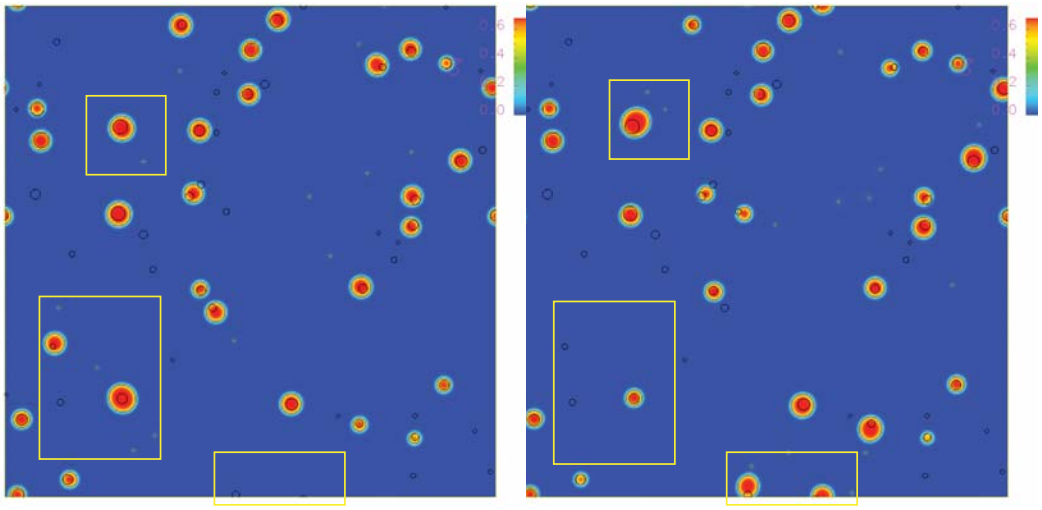

(a) (b)

Figure 7. Gas bubble morphology a) and b) with vacancy emissions from different distributed dislocations. The light blue dots denote the location of dislocations while the black circles identify the initial gas bubbles. The framed parts illustrate the obvious difference due to the local emission of vacancies.

4.2.1.3 Gas bubble growth kinetics in 2-D during annealing from 1100 K to 2100 K

Gas bubble evolution during annealing was also simulated in two dimensions. The simulation cell and initial gas bubble distribution were the same as those described in previous section. The vacancy and gas concentrations were 0.0042. The annealing started from 1100 K and temperature increased at a rate of 2K/s. Three simulations with different initial gas bubble distributions were run. The evolution of gas bubble number and gas volume fraction are plotted in Figure 8. Figure 8(a) shows that at low temperature the gas bubble is frozen due to its small diffusivity. With increasing temperature, the small bubbles become unstable, and a sharp drop of gas bubble number is observed at T=1400 K. After that there is a short period when the number of gas bubbles is almost constant. Then the bubble number linearly decreases. The volume fraction evolution in Figure 8(b) also shows the freezing, dissolving, and growing stages. A comparison of the experimental and modeling results of gas bubble density and mean gas diameter is plotted in Figure 9. A linear relationship between the double logarithmic bubble density and mean bubble diameter during the gas bubble growth was observed, which is qualitatively in agreement with the experimental results.

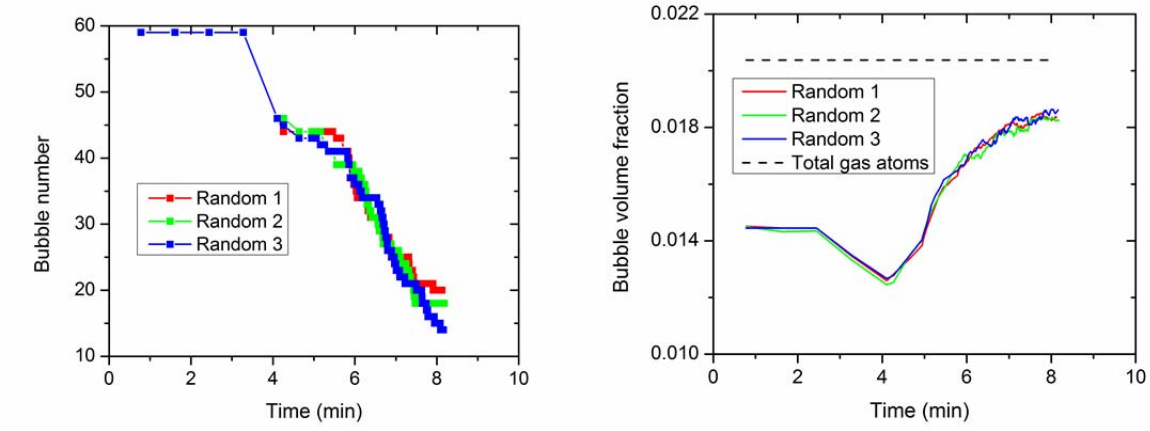

(a) (b)

Figure 8. Evolution of bubble number and bubble gas atom volume fraction with time.

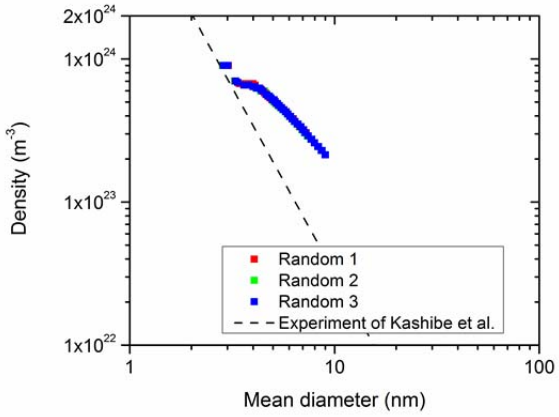

Figure 9. Comparison of gas bubble density vs mean diameters from PF modeling and experiments.

4.2.1.4 Evaluation of computational efficiency with FFTW

We have investigated the numerical efficiency of FFTW. Table 7 lists the central processing unit (CPU) time for 10,000 simulation time steps in 2-D and 3-D. We found that calculating the driving force due to elastic interaction only takes about small percentage of total CPU time, which is one of advantage of the FFTW method compared to the FEM.

Table 7. CPU time with 2.66-GHz core for 10,000 simulation time steps.

Description	CPU Time

2-D simulation domain: 256*256 without elastic interaction	0.0742 h
2-D simulation domain: 256*256 with elastic interaction	0.0757 h
3-D simulation domain: 128*128*36 without elastic interaction	1.24 h
3-D simulation domain: 128*128*36 without elastic interaction	1.36 h

4.2.2 Results from INL's phase-field modeling

4.2.2.1 Gas bubble kinetics in 2-D and 3-D during annealing from 1100 K to 2100 K

To model post-irradiation annealing in UO_2, we used 2-D and 3-D simulations. The 2-D simulations started with a random gas bubble distribution in a 300-nm by 300-nm simulation domain with two representative thicknesses in the z-direction (necessary to calculate the bubble density). We conducted one simulation with a z-thickness of 1 nm with 81 initial bubbles and one with a z-thickness of 10 nm with 841 initial bubbles. Both simulations started with an average bubble radius of 1 nm, although the initial radius varied randomly by up to ±25%. We also conducted a 20-nm by 20-nm by 20-nm 3-D simulation with eight initial bubbles with a 1.5-nm mean initial radius. The 1-nm thickness 2-D simulation and the 3-D simulation were run until one bubble remained. The 10-nm thickness 2-D simulation was run until 4 bubbles remained. See Figure 10 for examples of the bubble growth for the 10-nm thickness 2-D simulation.

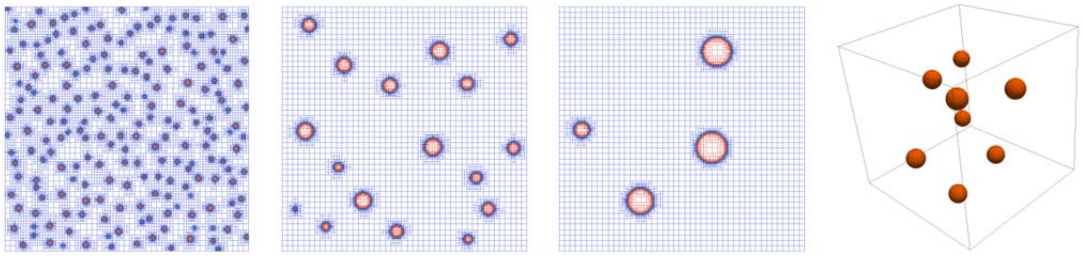

Figure 10. Images of the bubble growth during the annealing of the 10-nm thickness 2-D simulation. Note that the adapted mesh is also shown in the simulations. The initial condition of the 3-D simulation is also shown.

For the 2-D simulations, the bubble density and the average bubble radius were plotted as a function of time, as shown in Figure 11. The bubble density first begins to decrease after 3.5 minutes for the 10-nm thickness simulation but after 2.5 minutes for the 1 nm thickness. The decrease in bubble density coincides with the increase in mean bubble radius for the 10-nm thickness simulation but not for the 1-nm thickness. We suspect that the delay in the radius increase is due to the time required for the gas atoms to

migrate across the large distance between bubbles. The bubble density decreases by nearly two orders of magnitude by the end of both simulations.

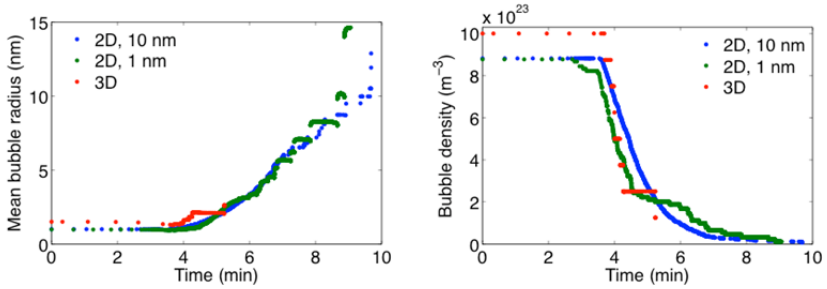

Figure 11. Post-irradiation annealing results, with the average bubble radius vs. time on the left and the bubble density vs. time on the right.

We also compared our results to the linear fit of the logarithm of the bubble number density to the logarithm of the mean bubble diameter from Kashibe et al. [26] (see Figure 12). As shown, the 10-nm thickness 2-D simulation predicts a linear relationship throughout the simulation, while the 1 nm thickness 2-D simulation predicts a linear relationship only after the mean diameter exceeds 6 nm. The linear slopes of both 2-D simulations are equal and are less than the slope of the experimental fit. The 3-D result has a linear relationship throughout the simulation and the slope is identical to the experimental fit. Thus, it appears that 2-D simulations under-predict the decrease in the bubble density with increasing diameter, probably because they only capture the gas atom flux in the x-y plane.

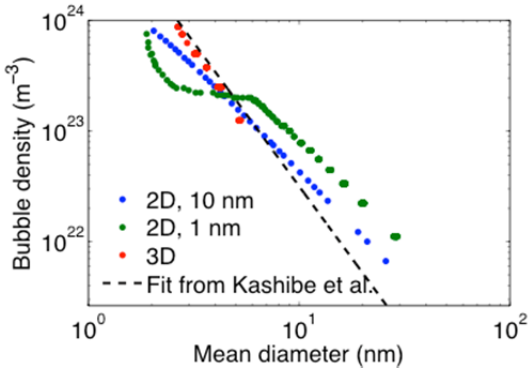

Figure 12. Gas bubble density as a function of the gas bubble mean diameter, comparing the experimental fit from Kashibe et al. [26] to our 2-D and 3-D simulation results. The 3-D results are a better fit with the experimental fit.

4.2.2.2 Evaluation of the effectiveness of mesh and time step adaptivity

During the simulations, we employed the time and mesh adaptivity capabilities in MARMOT. With the mesh adaptivity, the smallest element size is 0.42 nm and the largest is 6.67 nm. We began the simulation with a time step of 40 seconds, but as the temperature increases, the time step must be decreased. In addition, modeling the disappearance of a bubble requires a smaller time step. Therefore we employed

time step adaptivity as well. Both the mesh and time step adaptivity are described in more detail by Tonks et al. [68].

To demonstrate the effect of mesh and time step adaptivity, we plotted the degrees of freedom (DOFs) in the simulation vs. time as well as the time step size vs. time for the 10-nm thickness 2-D simulation, as shown in Figure 13. In Figure 13(a), the DOFs are plotted together and the number of bubbles vs. time is shown for reference. From this plot it is clear that each time a bubble disappeared, fewer DOFs were needed to accurately represent the system. Thus, as time went on, the computational expense reduced dramatically. Due to the increase in the diffusion constant as the temperature increased, the time step reduced by many orders of magnitude over time (see Figure 13(b) to see the time step size and the inverse of the diffusion constant). Although the time step size is quite noisy, due to the small time step required every time a bubble disappears, there is a clear relationship between it and the value of the diffusion constant.

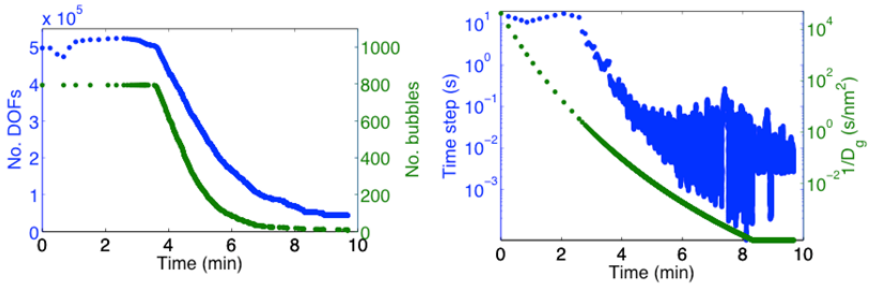

(a) (b)

Figure 13. The results of mesh and time step adaptivity for the 10-nm thickness 2-D simulation, where (a) shows the decrease in the number of degrees of freedom with time due to adapting the mesh, with the number of bubbles shown for reference, and (b) shows the time step size with time, with the inverse of the diffusion constant shown for reference.

4.2.2.3 Evaluation of the impact of the initial bubble positions and size distribution

Detailed information about the initial bubble positions and size distribution was not available from Kashipe et al. [26], therefore we have made assumptions for these parameters. In order to determine the sensitivity of the bubble growth relative to these assumptions, we conducted several simulations on a 100-nm by 100-nm domain with 100 initial bubbles. In these simulations, we randomly varied the initial bubble positions by various amounts and we also varied the maximum amount of variation in the bubble radius.

By comparing the change in the bubble density with time, we found that the bubble configuration has little effect on the bubble growth, as shown in Figure 14(a). However, the initial bubble size distribution does have an effect (Figure 14(b)). As the variation in the initial bubble radius increases, the time at which the first bubble disappears, changes from 4 to 3 minutes. In addition, the rate at which the bubble density decreases with time decreases with increasing variation. However, this difference is no longer

evident once the bubble density has reached 30% of its original value. Thus, the selection of the initial bubble configuration has little effect on our simulations, but the bubble size distribution has a significant effect on the initial stages of the bubble growth.

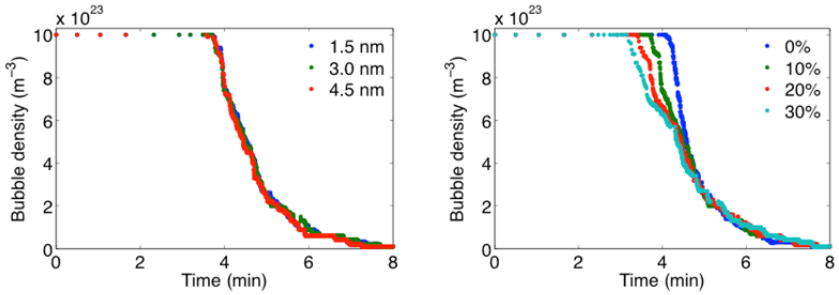

(a) (b)

Figure 14. Investigation of the effect of the initial condition of the bubbles using a 100-nm by 100-nm 2-D domain, where (a) shows the effect of the variation in the bubble position and (b) the effect of variation in the bubble radius.

4.2.3 Results from SNL's Potts modeling

4.2.3.1 Gas bubble growth kinetics in 3-D

The microstructures showing bubble coarsening are shown in Figure 15. A portion of the simulation space, 200 x 200 x 200 lattice sites corresponding to 40 nm x 40 nm x 40 nm, is imaged because the entire space is too large and this section shows sufficient detail and extent to illustrate the behavior well. The small red dots are the "dissolved" gas in the lattice. The bubbles are the spherical, large, red features. As can be clearly seen the bubbles are coarsening. The bubble growth curve is shown in Figure 16. As expected, the bubbles are coarsening. The time scale for this simulation was determined by estimating that the bubble would coarsen to 10 nm in 10 minutes. The simulation started with a total of 1176 bubbles with average radii $\langle r \rangle$ = 0.8 nm and ended with 142 bubbles of $\langle r \rangle$ = 2.2 nm. The size distribution of the bubbles is shown in Figure 17 at different times during the simulation. The skewedness of the distribution at the later times is surprising. The skewedness was anticipated to be to the larger sizes because it is at short times during annealing.

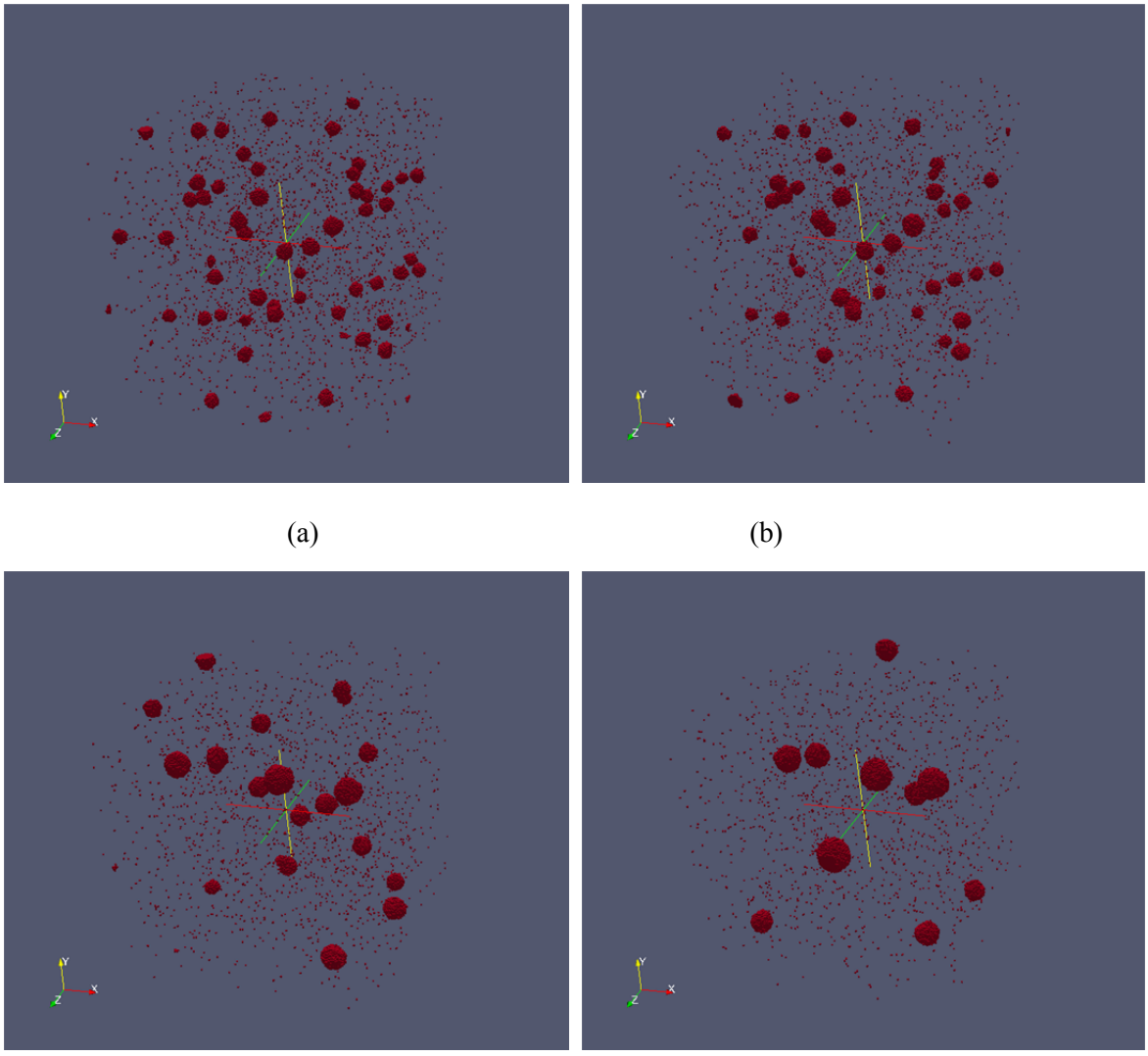

(a) (b)

(c) (d)

Figure 15. Microstructure of bubbles coarsening (only a portion of the simulation space is imaged, $200^3\ l^3$ corresponding to 40 nm x 40 nm x 40 nm).

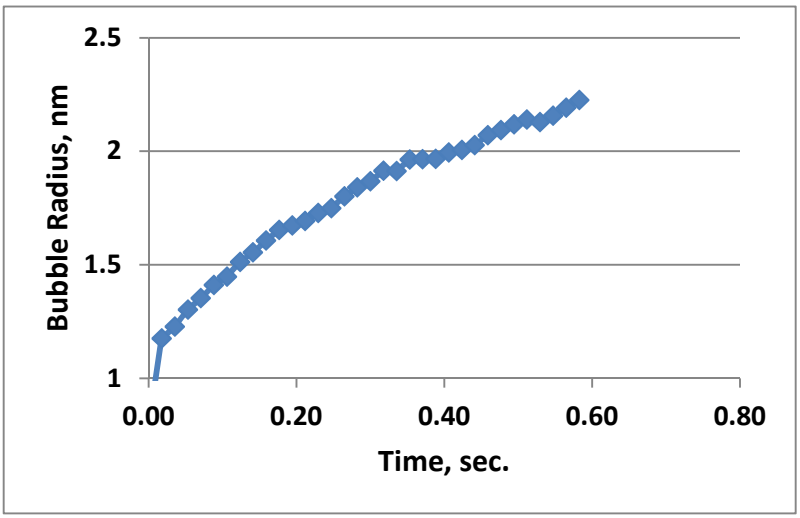

Figure 16. Average bubble radius as a function of time.

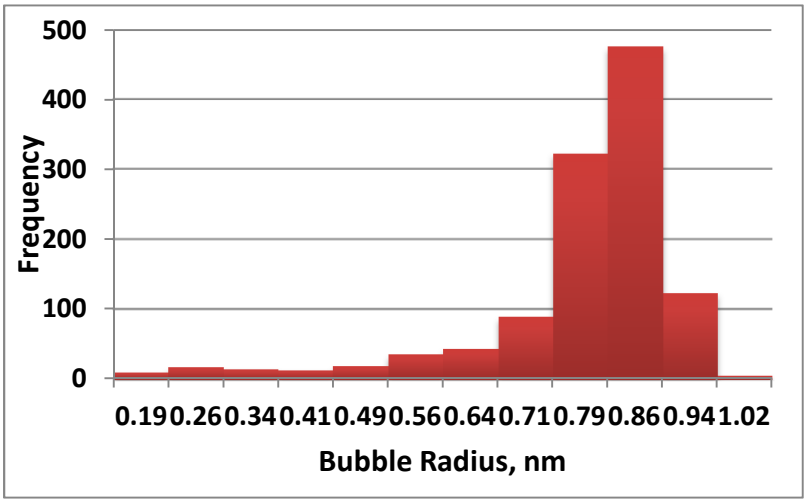

(a) Time = 0.0 sec, <*r*> = 0.79

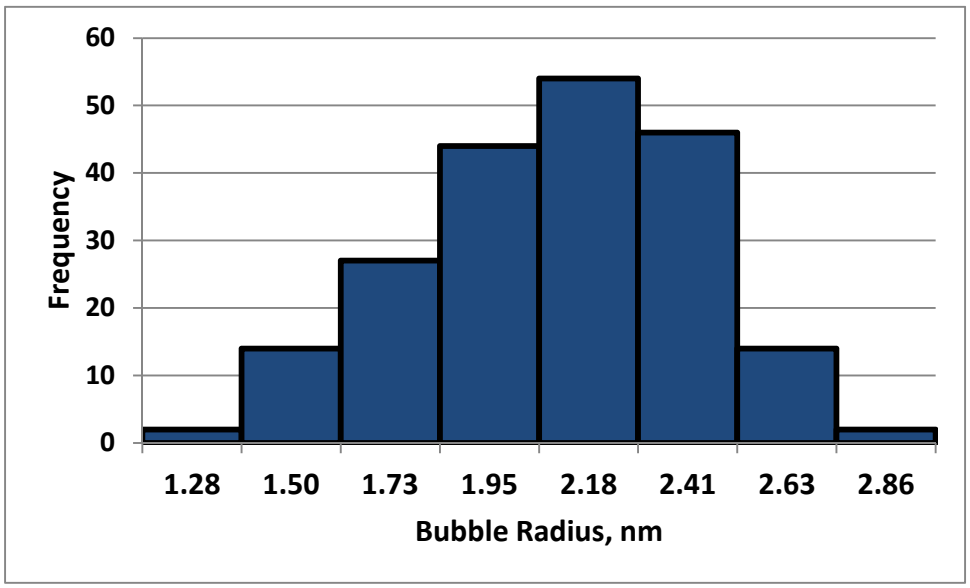

(b) Time = 0.35 sec, <*r*> = 2.0

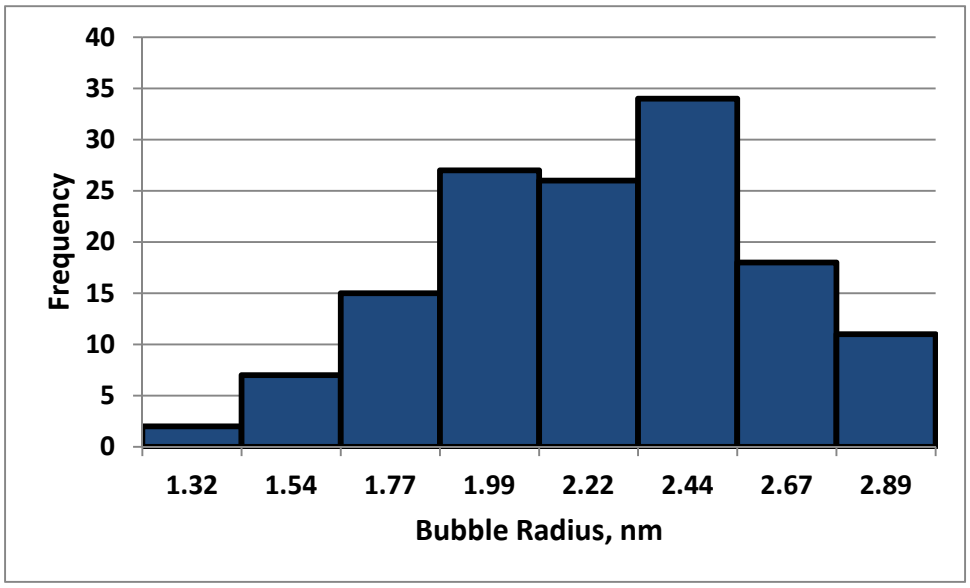

(c) Time = 0.58 sec, <*r*> = 2.2

Figure 17. Bubble size distributions as the bubbles coarsen.

4.2.4 Results from ORNL's Potts/kMC modeling

4.2.4.1 Gas bubble growth kinetics in 3-D at 1800 K

Large 3-D runs were made with a 208 x 208 x 208 sites using 512 processes. The size of each site was again 2.0 nm. Figure 18 shows the growth kinetics of the bubbles. Figure 18 also shows the growth curve in the presence of a small volume fraction (0.005) of "dislocated" sites acting as pinning sites. In these simulations, it was assumed that contact with "dislocated" sites would completely suppress surface diffusion locally for the site. It is clear that pinning reduces the growth kinetics. However, it is not clear at this point how to correlate the dislocation density with the fraction of "dislocated" sites. Also, the long-range stress fields associated with the dislocations have to be considered unless the dislocations are present in the form of a recovered low-angle grain boundary network at the annealing temperature. By adjusting the volume fraction of the dislocated sites, it is possible to match the simulation and annealing data of Kashibe et al. [26]. The bubble size distribution with time can be seen in Figure 19.

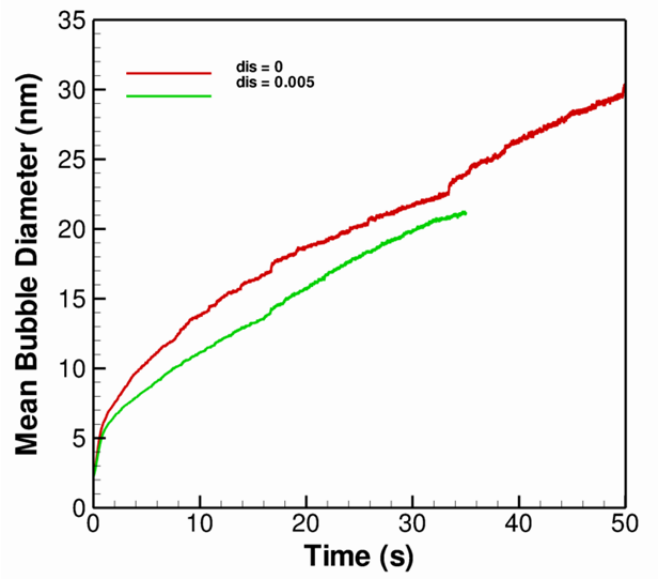

Figure 18. Bubble growth kinetics in a 416- x 416- x 416-nm^3 simulation volume.

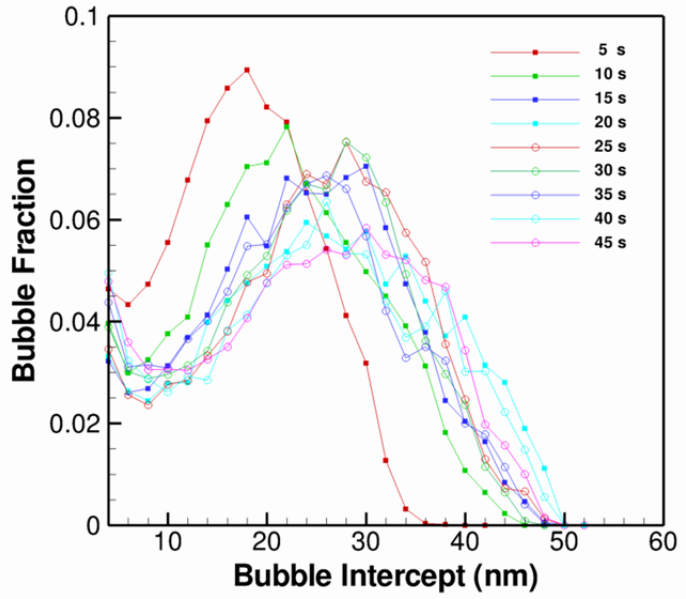

Figure 19. Bubble size distribution obtained using the 416- x 416- x 416-nm^3 run.

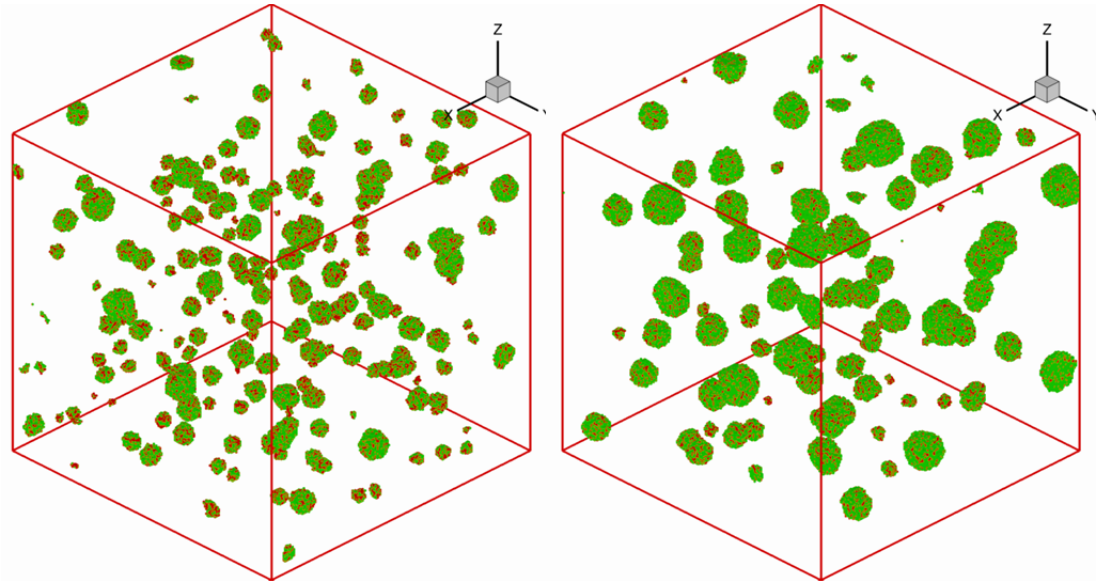

5 sec 15sec

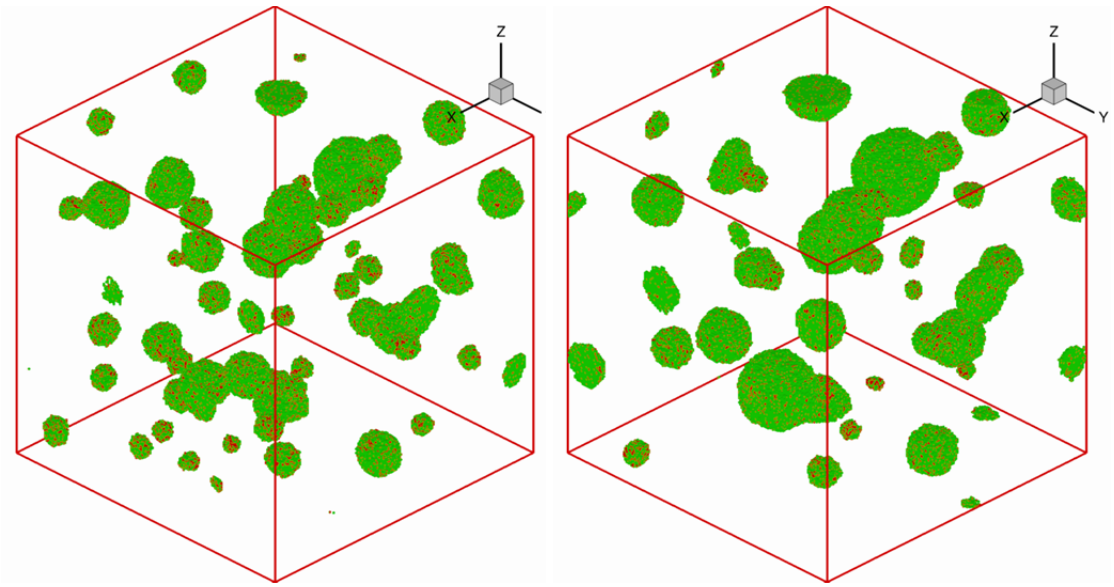

30 sec 45 sec

Figure 20. Temporal evolution of the bubbles in the 416- x 416- x 416-nm^3 run showing the migration and coalescence mechanism operating throughout the simulation time.

The temporal evolution of the bubbles is shown in Figure 20 for the larger run. It is clear that the cylindrical bubbles that formed in the smaller domain do not form and there is no sudden increase in the growth rate as observed in the smaller run. However, a few growth bumps are seen in Figure 18 that correspond to rare coalescence events associated with large bubbles.

The calibration of the Potts/kMC code can be rescaled at any time during the simulation, assuming that each simulation cell now corresponds to a larger bubble size. The structure should be re-mapped so that the spatial distribution of the bubbles is preserved. With this re-mapping, it is now possible to change the relationship between the Monte Carlo time (MCS) and the real time such that each MCS now corresponds to a longer real time. Such an approach has been demonstrated for simulating grain growth in steels [71]. Therefore the models can be used efficiently to simulate the microstructure evolution at hours of annealing time.

4.3 Assessment of Mesoscale Modeling Methods

As with most modeling and simulation methods, the mesoscale approaches can be broken down into three main elements. These elements are: 1) the system of equations used to describe the mechanisms, 2) the numerical method applied to solve for the unknowns, and 3) the geometric representation of the physical domain. The assessment of the mesoscale methods has been organized around each of these elements and describes how each element impacts the benchmark problem calculation results.

The idealized mesoscale method benchmark problem was developed to approximate the behavior of intra-granular fission gas bubbles under post-irradiation, isothermal annealing conditions. The UO_2 microstructure behavior under these conditions is a bubble growth and coarsening process. Kashibe et al. [26] and White [24] have both studied the behavior of intra-granular bubbles under post-irradiation annealing and have found a complex response that is governed primarily by vacancy supply and the local non-equilibrium state of the bubble pressure. At long time anneals with sufficient vacancy supply, Ostwald ripening behavior leads to bubble growth and coarsening. This has been observed in the vicinity of grain boundaries. However, neither of these evaluations observed purely Ostwald ripening or bubble coalescence in the center region of the grains. In these regions, the growth and coarsening behavior was found to follow a vacancy, dislocation, and bubble non-equilibrium interaction process. The bubble density as a function of the mean bubble diameter was found by Kashibe et al. [26] to have a slope of -2.6 on a log-log plot. Equilibrium conditions representing Ostwald Ripening generally exhibit a coarsening slope of -3 on a log-log plot [72]. A coarsening slope greater than -3 indicates that bubble growth mechanisms are more dominant than coarsening processes when compared to the classical Ostwald behavior. White [24] postulated that the interaction of vacancies with dislocations and the non-equilibrium strain conditions in the vicinity of the intra-granular bubbles causes a vacancy starvation condition that promotes bubble growth over coarsening and broadens the bubble distribution and reduces the bubble coarsening rate.

The PF methods used in this evaluation by PNNL and INL described gas bubble growth and coarsening by bulk diffusion of vacancies and gas atoms driven by minimization of chemical free energy, interfacial energy and elastic energy. The Potts method used in this evaluation by SNL described gas bubble growth and coarsening using atom random walk driven by the minimization of the chemical free energy and interfacial energy. The kMC/Potts method used in this evaluation by ORNL described gas bubble migration and coarsening by surface diffusion driven by the minimization of chemical free energy and interfacial energy. Both the PF and Potts methods have previously been shown to reproduce second phase particle/precipitate growth and coarsening by Ostwald ripening mechanisms [73]. It is envisioned that by applying these methods to the behavior of intra-granular bubble growth and coarsening during post-irradiation annealing conditions, it is possible to demonstrate that these methods can consider more complex microstructure behaviors than those governed completely by Ostwald ripening and produce quantitative results.

Figure 21 compares the simulation results for each method to the data of Kashibe et al. [26], representing typical measured intra-granular bubble behavior. Shown in Figure 21 is the bubble density (N_b) versus mean bubble diameter (D_b) for several expected or measured trends ($N_b \propto D_b^{-n}$ data of Kashibe et al. [26] given by n = 2.6, theoretical Ostwald ripening given by n = 3 and an estimated curve for n = 2). Symbols are used to display the results at the end of the simulation for each method used in this evaluation. It should be noted that the end time in each simulation varied depending on the method used and computer resources available. As noted previously, each method used somewhat different assumptions and initial conditions to perform the simulations, which makes it difficult to compare the results directly and this must be considered in this evaluation. However, the comparison shown in Figure 21 provides a basis for evaluating the methods and their abilities to simulate reliably the microstructure evolution behavior of intra-granular bubbles.

Both the 2-D PF models calculate a bubble growth and coarsening behavior that has a trend of between 1.5 and 2 for the exponent n ($N_b \propto D_b^{-n}$). These results demonstrate a much slower coarsening behavior as compared to either the Kashibe data or the Ostwald ripening mechanism. Without detailed information about the calculated bubble size distribution, the causes of these trends are difficult to identify. The INL 3-D PF calculation exhibits coarsening behavior (n~2.5) that is consistent with the Kashibe data. The PNNL 3-D PF calculation has the same coarsening exponent as the 2-D simulation. The SNL Potts 3-D and the ORNL Potts/kMC 3-D models calculate a growth and coarsening behavior that has a slope equal to or greater than three. These results indicate that the mechanisms were dominated more by Ostwald ripening mechanisms than the data would suggest.

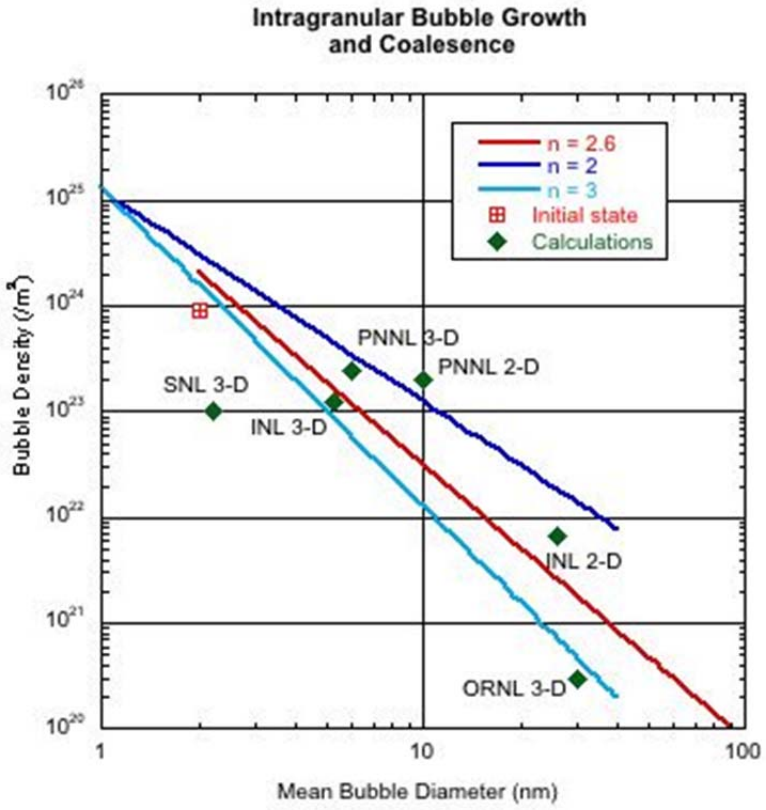

Figure 21. Trend in bubble density versus mean bubble diameter for intra-granular bubble growth and coarsening during post-irradiation annealing. Comparison of results from mesoscale methods and experimental data is indicated.

Some key observations from the comparison are summarized below.

- Results from the PF methods predict that gas bubble growth and coarsening evolution occurs in three stages: unstable gas bubble disappearance, bubble growth, and Ostwald ripening. The calculated kinetics of intra-granular gas bubble density and size during unstable gas bubble disappearance and

bubble growth strongly depends on the initial size and spatial distributions of the intra-granular gas bubbles.

- The two PF methods predict a linear relationship between the logarithm of the bubble density and the logarithm of the mean bubble diameter. Kashibe et al. [26] and others observed similar behavior in measurements obtained from post-irradiation annealing tests. The exponential coefficients predicted by the PNNL 2-D and 3-D simulations and the INL 2-D simulations are smaller than the exponent determined from experiments (~1.5 vs 2.6). Insufficient information is available to identify the reason that the exponent values do not match the experimentally observed values. The PNNL results, however, suggest incomplete representation of the sinks and sources of vacancies in real materials is the cause for the differences. Sensitivity studies performed by PNNL show that vacancy starvation may cause more bubble loss and decrease bubble growth as compared to higher concentrations of vacancies. Similar studies show that elastic interaction also slows down the growth kinetics.
- The exponential coefficient predicted by the INL 3-D PF simulation is very close to the experimentally observed values. On the other hand, the exponential coefficient obtained from PNNL 3-D phase field simulation is almost the same as that predicted from the 2-D method. The dependency of the calculated bubble growth and coarsening behavior on the 2-D and 3-D methods used by INL suggests that the 2-D simulation method only represents gas diffusion in one plane.
- Comparison of the PNNL and INL methods shows that the thermodynamic and kinetic data used to define the parameters of Benchmark Problem 1 are different. For example, the surface energy used in the PNNL model was 0.6 J/m, whereas the INL simulation used ~4 J/m. Typical values of surface energy range between 0.6 J/m and 1 J/m based on past experience. Furthermore, a parabolic function was used in PNNL method to approximate the free energy of ideal solute matrix phase while an 8th order polynomial was used in INL method. The minimization of interfacial energy and chemical free energy is the driving force of gas bubble growth while the minimization of interfacial energy is the driving force of Ostwald ripening. The differences in the sources of the driving forces calculated in these two methods will cause the calculated growth behavior to vary between the two methods. In 3-D, the interfacial energy may play a more important role because the nano-gas bubble has much higher surface fraction in 3-D compared to that in 2-D. In addition, numerical pinning in 3-D could be another reason to reduce the growth kinetics, especially for a small interfacial energy.
- In the SNL Potts method, bubble coarsening is calculated by random walk of atoms and coalescence, and by the gas in the bubbles dissolving back in the lattice and re-precipitation out on other bubbles. The driving force of gas bubble evolution in the SNL Potts method is the minimization of chemical free energy and interfacial energy similar to that used in the PF methods. The 3-D simulations performed by SNL provide the evolution of gas bubble size and size distribution. However, since the model does not use kinetic properties, the time had to be determined indirectly by estimating bubble coarsening kinetics.
- At high temperature, the coarsening of gas bubble may attribute to Ostwald ripening and small gas bubble migration. Ostwald ripening of gas bubbles is through bulk diffusion whereas gas bubble migration by surface diffusion. The reason for Ostwald ripening is the Gibbs-Thomson effect, which leads to smaller particles having a higher solubility than larger particles. Thus, a flux from smaller particles to larger ones due to the concentration gradient leads to the shrinkage of smaller particles

and the growth of larger particles. The PF models and the Potts model from SNL describe Ostwald ripening while the kMC/Potts method developed by ORNL describes gas bubble migration by surface diffusion processes.

- The ORNL kMC/Potts model used bubble migration to describe gas bubble growth and coalescence during post-irradiation annealing. Because ORNL chose to model the processes using largely different mechanisms than those used in the other methods, the comparison of this method with the results from the PF or Potts models is difficult.
- While the results are encouraging, the use of different thermodynamic and kinetic properties in the PF methods employed in this evaluation make formulating definitive conclusions about the predictive capabilities of these methods elusive. Further work is needed to better understand the strengths and areas of improvement in these capabilities. Similar conclusions can be made about the statistical methods applied in this evaluation.

The simulation results for Benchmark Problem 1 demonstrate that the PF and Potts methods can capture several aspects of 3-D intra-granular gas bubble evolution during post-irradiation annealing conditions in both length and time scales for the benchmark problem. The ability of the PF methods to approximate a higher degree of the physical mechanisms operative during the post-irradiation annealing of intra-granular bubbles, allows these methods to represent quantitatively the observed experimental data. The Potts and kMC methods generate results that qualitatively display promising trends. However, neither of these quantum statistical methods represented well the quantitative results for the intra-granular bubble growth and coarsening behavior observed in post-irradiation annealing.

5. MAIN CONCLUSIONS AND FUTURE WORK

The capabilities of several different mesoscale methods were evaluated using Benchmark Problem 1 designed to describe the intra-granular fission gas bubble evolution in UO_2 material under post-irradiation thermal annealing. The purpose of the mesoscale benchmark problem was to provide a common basis to assess the PF and Potts/kMC mesoscale methods with the objective of identifying the strengths and areas of improvement in the predictive modeling of microstructure evolution. Each method considered in this evaluation has its own unique features that provide the capabilities to simulate the evolution of microstructure under different conditions or driving forces. For example, the PF model developed by PNNL considered vacancy and Xe atom diffusion, vacancy emission, and elastic strain-field interactions. The method uses FFTW to solve the system of equations that describe the microstructure behavior. The MARMOT PF model developed by INL considered only Xe atom diffusion and with no attention given to elastic strain field interactions. MARMOT used the FEM combined with adaptive mesh and time step capabilities to solve the system of questions used to describe the gas bubble behavior. The Potts model developed by SNL considers random walk mechanisms while the Potts/kMC model developed by ORNL considers gas bubble migration and coalescence.

The mesoscale Benchmark Problem 1 was constructed to include important microstructural evolution mechanisms on the kinetics of intra-granular fission gas bubble behavior such as the atomic diffusion of Xe atoms, U vacancies, and O vacancies, the effect of vacancy capture and emission from defects, and the elastic interaction of non-equilibrium gas bubbles. An idealized set of assumptions and a common set of

thermodynamic and kinetic data were imposed on the benchmark problem to simplify the mechanisms considered. To assess the robustness of the different methods, the simulation results for mean gas bubble diameter and gas bubble density were compared to the selected experimental results. All the mesoscale methods used in this study were found to have various levels of capabilities to model gas bubble coarsening in UO_2 fuel. The evaluation found that the PF methods, by the nature of the free energy formulation, are able to represent a larger subset of the mechanisms influencing the intra-granular bubble growth and coarsening mechanisms in the idealized benchmark problem as compared to the Potts and kMC methods. The Potts and kMC methods were able to capture some details of the growth and coarsening behavior. However, without adequate treatment of the kinetics of the mechanisms, this study was unable to fully evaluate the predictive capability of these methods. Finally, it is recognized that the mesoscale benchmark problem as formulated does not specifically highlight the strengths of the discrete particle modeling used in the Potts and kMC methods.

While the results of this evaluation to assess mesoscale modeling methods are encouraging, the use of different thermodynamic and kinetic properties in the methods employed in this evaluation make formulating definitive conclusions about the predictive capabilities of mesoscale methods elusive. As a result, the major outcomes of this evaluation are the following future work recommendations:

1) Preliminary simulations demonstrated that interfacial energy, critical size of gas bubbles, initial gas bubble size and spatial distribution, vacancy starvation and emission, and elastic interaction affect the gas bubble growth kinetics within the mesoscale benchmark problem. It is important to systematically examine the models used in each method to represent these mechanisms and describe their effect on the gas bubble kinetics predicted by each method.

2) In this work, the phase field equations were solved with FFTW (PNNL) and with FEM (INL). A comprehensive comparison between these methods needs to be conducted. To ensure a reliable comparison, the same set of PF equations and material parameters should be used with both methods.

3) For the Potts and kMC/Potts methods, it is important (a) to evaluate the approaches used to integrate the representation of potential mechanisms into the methods, and (b) to establish the relation between the method parameters and the thermodynamic and kinetic properties that describe the behavior of the microstructure evolution.

6. ACKNOWLEDGMENTS

This work was supported by the U.S. Department of Energy's Nuclear Energy Advanced Modeling and Simulation (NEAMS) Program at the Pacific Northwest National Laboratory, which is operated by Battelle for the U.S. Department of Energy under Contract No. DE-AC05-76RL01830.

7. APPENDIXES

Appendix A: PNNL – Detailed Mesoscale Phase-Field Model Descriptions and Result Analysis

Appendix B: INL – Phase Field Models

Appendix C: SNL – Potts Model Simulation of Intra-Granular Bubble Coarsening During Post-Irradiation Annealing

Appendix D: ORNL – Detailed Potts/kMC Simulation and Result Analysis

Appendix E: LANL--Data from Atomistic Simulations

REFERENCES

[1] C.R.A. Catlow, P. Roy. Soc. Lond. A 364 (1978) 473.

[2] R.G.J. Ball, R.W. Grimes, J. Chem. Soc-, Faraday Trans. 86 (1990) 1257.

[3] K. Govers, S.E. Lemehov, M. Verwerft, J Nucl Mater 405 (2010) 252.

[4] D.A. Andersson, B.P. Uberuaga, P.V. Nerikar, C. Unal, C.R. Stanek, Phys Rev B 84 (2011) 054105.

[5] D.J. Bacon, A.F. Calder, F. Gao, J Nucl Mater 251 (1997) 1.

[6] B.D. Wirth, G.R. Odette, D. Maroudas, G.E. Lucas, J Nucl Mater 276 (2000) 33.

[7] M.S. Daw, S.M. Foiles, M.I. Baskes, Mater. Sci. Rep. 9 (1993) 251.

[8] E. Yakub, C. Ronchi, D. Staicu, J. Chem. Phys. 127 (2007).

[9] N.D. Morelon, D. Ghaleb, J.M. Delaye, L. Van Brutzel, Philos Mag 83 (2003) 1533.

[10] C.B. Basak, A.K. Sengupta, H.S. Kamath, J. Alloy. Compd. 360 (2003) 210.

[11] V. Tikare, M. Braginsky, E.A. Olevsky, J. Am. Ceram. Soc. 86 (2003) 49.

[12] L.Q. Chen, Ann. Rev. Mater. Res. 32 (2002) 113.

[13] I. Steinbach, B. Bottger, J. Eiken, N. Warnken, S.G. Fries, J Phase Equilib Diff 28 (2007) 101.

[14] A. Karma, W.J. Rappel, Phys Rev E 57 (1998) 4323.

[15] I. Steinbach, Model. Simul. Mater. Sci. Eng. 17 (2009).

[16] M. Kuroda, K. Yoshioka, S. Yamanaka, H. Anada, F. Nagase, H. Uetsuka, J. Nucl. Sci. Tech. 37 (2000) 670.

[17] G.A. Taylor, C. Bailey, M. Cross, Int. J. Numer. Meth. Engng 56 (2003) 507.

[18] C. Bailey, M. Cross, Int. J. Num. Meth. Eng. 38 (1995) 1757.

[19] Y.U. Wang, Y.M. Jin, A.M. Cuitino, A.G. Khachaturyan, Appl Phys Lett 78 (2001) 2324.

[20] V. Tikare, E.A. Holm, D. Fan, L.Q. Chen, Acta Mater 47 (1998) 363.

[21] D.R. Olander, D. Wongsawaeng, J Nucl Mater 354 (2006) 94.

[22] K. Nogita, K. Une, J Nucl Mater 226 (1995) 302.

[23] K. Nogita, K. Une, Nuclear Instruments & Methods in Physics Research Section B-Beam Interactions with Materials and Atoms 91 (1994) 301.

[24] R.J. White, The growth of intra-granular bubbles in post-irradiation annealed UO2 fuel, in: IAEA Technical committee on nuclear fuel behaviour modeling at high burn-up and its experimental support, Lake Windermere, UK, 2000.

[25] M.E. Cunningham, M.D. Freshley, D.D. Lanning, J Nucl Mater 200 (1993) 24.

[26] S. Kashibe, K. Une, K. Nogita, J Nucl Mater 206 (1993) 22.

[27] C. Baker, J Nucl Mater 71 (1977) 117.

[28] J.M. Griesmeyer, N.M. Ghoniem, J Nucl Mater 80 (1979) 88.

[29] D.A. Macinnes, I.R. Brearley, J Nucl Mater 107 (1982) 123.

[30] P. Losonen, J Nucl Mater 304 (2002) 29.

[31] P. Losonen, J Nucl Mater 280 (2000) 56.

[32] S.Y. Hu, C.H. Henager, J Nucl Mater 394 (2009) 155.

[33] S.Y. Hu, C.H. Henager, H.L. Heinisch, M. Stan, M.I. Baskes, S.M. Valone, J Nucl Mater 392 (2009) 292.

[34] Y.L. Li, S.Y. Hu, X. Sun, F. Gao, C.H. Henager, M. Khaleel, J Nucl Mater 407 (2010) 119.

[35] M. Tonks, D. Gaston, C. Perrnann, P. Millett, G. Hansen, D. Wolf, Nucl. Eng. Des. 240 (2010) 2877.

[36] C. Ronchi, J Nucl Mater 96 (1981) 314.

[37] D.A. Andersson, T. Watanabe, C. Deo, B.P. Uberuaga, Phys Rev B 80 (2009) 060101(R).

[38] B. Dorado, D.A. Andersson, C.R. Stanek, B. M., B.P. Uberuaga, G. Martin, M. Freyss, P. Garcia, submitted for publication (2012).

[39] G.E. Murch, C.R.A. Catlow, J. Chem. Soc., Faraday Trans. 2 83 (1987) 1157.

[40] H. Matzke, J. Chem. Soc., Faraday Trans. 2 83 (1987) 1121.

[41] H. Matzke, Radiat. Eff. Defect. S. 53 (1980) 219.

[42] B. Dorado, P. Garcia, G. Carlot, C. Davoisne, M. Fraczkiewicz, B. Pasquet, M. Freyss, C. Valot, G. Baldinozzi, D. Simeone, M. Bertolus, Phys Rev B 83 (2011) 035126.

[43] D.A. Andersson, F.J. Espinosa-Faller, B.P. Uberuaga, S.D. Conradson, submitted for publication (2012).

[44] A.C.S. Sabioni, W.B. Ferraz, F. Millot, J Nucl Mater 257 (1998) 180.

[45] W. Miekeley, F.W. Felix, J Nucl Mater 42 (1972) 297.

[46] X.Y. Liu, B.P. Uberuaga, D.A. Andersson, C.R. Stanek, K.E. Sickafus, Appl. Phys. Lett. 98 (2011) 151902

[47] O.G. Brandt, C.T. Walker, Phys. Rev. 170 (1968) 528.

[48] J.B. Wachtman, M.L. Wheat, H.J. Anderson, J.L. Bates, J Nucl Mater 16 (1965) 39.

[49] Y.M. Jin, A. Artemev, A.G. Khachaturyan, Acta Materialia 49 (2001) 2309.

[50] Y.L. Li, S.Y. Hu, Z.K. Liu, L.Q. Chen, Acta Mater 50 (2002) 395.

[51] S.Y. Hu, C.H. Henager, L.Q. Chen, Acta Mater 58 (2010) 6554.

[52] M.P. Anderson, D.J. Srolovitz, G.S. Grest, P.S. Sahni, Acta Metall Mater 32 (1984) 783.

[53] E.A. Holm, J.A. Glazier, D.J. Srolovitz, G.S. Grest, Phys. Rev. A 43 (1991) 2662.

[54] E.A. Holm, G.N. Hassold, M.A. Miodownik, Acta Mater 49 (2001) 2981.

[55] E.A. Holm, M.A. Miodownik, A.D. Rollett, Acta Mater 51 (2003) 2701.

[56] M. Miodownik, J.W. Martin, A. Cerezo, Philos Mag A 79 (1999) 203.

[57] V. Tikare, M.A. Miodownik, E.A. Holm, J. Am. Ceram. Soc. 84 (2001) 1379.

[58] V. Tikare, J.D. Cawley, Acta Mater 46 (1998) 1333.

[59] V. Tikare, J.D. Cawley, Acta Mater 46 (1998) 1343.

[60] S.B. Lee, J.M. Rickman, A.D. Rollett, Acta Mater 55 (2007) 615.

[61] G.N. Hassold, I.W. Chen, D.J. Srolovitz, J. Am. Ceram. Soc. 73 (1990) 2857.

[62] M. Braginsky, V. Tikare, E. Olevsky, Int. J. of Sol. Struc. 42 (2005) 621.

[63] V. Tikare, M. Braginsky, D. Bouvard, A. Vagnon, Comp. Mater. Sci. 48 (2010) 317.

[64] S.Y. Hu, C.H. Henager, Acta Mater 58 (2010) 3230.

[65] J.W. Cahn, Acta Metall. 9 (1961) 795.
[66] J.W. Cahn, S.M. Allen, Le J. de Phys. Col. 38 (1977) 51.
[67] L.Q. Chen, J. Shen, Comput. Phys. Commun. 108 (1998) 147.
[68] M.R. Tonks, D. Gaston, P.C. Millett, D. Andrs, P. Talbot, Comp. Mater. Sci. 51 (2012) 20.
[69] J. Noirot, L. Desgranges, J. Lamontagne, J Nucl Mater 372 (2008) 318.
[70] T. Suzudo, H. Kaburaki, M. Itakura, E. Wakai, Modelling Simul. Mater. Sci. Eng. 16 (2008) 055003.
[71] B. Radhakrishnan, T. Zacharia, Metall Mater Trans A 26 (1995) 2123.
[72] P.W. Voorhees, J. Statist. Phys. 38 (1985) 231.
[73] D.N. Fan, S.P. Chen, L.Q. Chen, P.W. Voorhees, Acta Mater 50 (2002) 1895.

Appendix A

PNNL--Detailed Mesoscale Phase-field Model Descriptions and Result Analysis

Yulan Li, Shenyang Hu, Robert Montgomery, Fei Gao, and Xin Sun

Pacific Northwest National Laboratory (PNNL)

A-1. Assumptions

Gas bubble growth needs continuous supply of both vacancies and gas atoms. Starvation of either vacancies or gas atoms will limit the bubble growth. Due to high pressure inside of gas bubbles and large lattice mismatch of interstitial Xe atoms and U vacancies, elastic interaction can be an important driving force or resistance for the diffusion of vacancies and Xe atoms. Defects such as dislocations are sinks or sources of vacancies. The spatial distribution and density of dislocations affect the sink or emission strength of vacancies, hence the concentration of vacancies. Our phase-field model takes these physics into account. However, due to the complex of the system and the uncertainty of thermodynamic and kinetic properties, we made the following assumption to simplify the problem.

1) Xe atoms may occupy U vacancy lattices or interstitial lattices that depend on valid U vacancy concentration and Xe concentration. For the simplicity of description, we assume that Xe always occupy interstitial lattice. Thus, the Xe_U (Xe occupies one uranium vacancy) is described by a cluster of a U vacancy and an interstitial Xe atom. Such a two sublattice model allows studying the effect of starvation and vacancy emission on gas bubble growth.
2) Xe interstitial, U vacancy, and the Xe_U (Xe occupies one uranium vacancy) have very different mobility from the calculation of migration energy of defects. In addition, other complexes such as Xe_{UO} (Xe occupies one uranium vacancy and one oxygen vacancy) and Xe_{UO2} (Xe occupies one uranium vacancy and two oxygen vacancies) also contribute the diffusion of vacancies and Xe atoms. So the effective mobility of U vacancies and Xe atoms are used in the model. In the present simulations effective migration energy 3.9 eV for both U vacancy and Xe atom are used. But the model has no limitation of using different mobility of of U vacancies and Xe atoms.
3) Gas bubbles formed at low temperature may be unstable at annealing temperature. So initial size distribution of gas bubbles may dramatically impact the results of gas bubble number and size evolution. In our simulations, a normal (Gaussian) distribution with a mean radius of 1nm and standard deviation of 1nm is used to generate the initial gas bubble size distribution.

4) Chemical potential gradient is one of driving forces for vacancy and Xe diffusion. We use the Kim's model [1] to describe the chemical free energy of matrix and gas phases. To efficiently solving the phase-field evolution equation, two parabolic functions are used to fit the ideal solution free energy of the matrix with vacancies and Xe atoms and the free energy of the gas bubble phase which is calculated from the equation of state.

5) Dislocations are sinks or sources of vacancies. Because of the lack of sink and emission strengths, the emission rate of vacancies from dislocations is taken as a model parameter, like the initial vacancy concentration.

6) Experiments[2] suggested that vacancy emission could be an important mechanism which affects the gas bubble evolution kinetics. Therefore, we assumed that initial vacancy concentration is a model parameter.

7) O vacancy has much higher mobility than U vacancy and Xe atom. But it is not a rate limiting species in gas bubble growth. Therefore, we neglected O vacancies. Its effect is accounted in the effective diffusivity of U vacancies and Xe atoms.

8) The contribution of small gas bubble migration at high temperature to gas bubble evolution is ignored in this model. However, a phase-field model of void migration can be extended to describe gas bubble migration [3, 4].

A-2. Model description

Definition of microstructure and phase field model variables

In the framework of phase-field modeling, the microstructure of intra-granular fission gas bubbles in UO_2 can be described by two sets of field variables. One is the concentration variables describing the concentrations of diffusive vacancies and gas atoms. The other one is the order parameter distinguishing the matrix and gas phases. In reality, there are a number of mobile vacancies in irradiated UO_2 such as single oxygen and uranium vacancies, and small vacancy clusters. Fission reaction also produces a number of fission gas atoms including Xe, Kr, and He which form the gas phase. For simplicity, we use variable $c_v(\mathbf{r},t)$ to describe the overall vacancy concentration which includes O and U vacancies and their vacancy clusters, and $c_g(\mathbf{r},t)$ to describe overall gas atoms (Xe, Kr, He, …) concentration. $\mathbf{r}$ and t are the spatial coordinate and time, respectively. We assume that the vacancies and gas atoms diffuse with effective diffusivity. Thus, two sub lattices, i.e., the host lattice and interstitial lattice, are used to describe the crystal structure. The host lattice is occupied by U or O atom or vacancy while gas atoms occupy the interstitial lattices. The $c_v(\mathbf{r},t)$ and $c_g(\mathbf{r},t)$ are the numbers of moles in the molar volume of UO_2 lattices, respectively. Here, we imply that the ratio of U and O vacancies in the molar

volume remains ½ during absorption, emission and diffusion processes. The order parameter is denoted by $\eta(\mathbf{r},t)$ which is 1 in gas bubble phase and 0 in the matrix phase. Across the interface between a gas bubble and the matrix $\eta(\mathbf{r},t)$ smoothly varies from 1 to 0.

Total free energy

The total free energy of the system includes the chemical free energy, gradient energy terms, and long-range interaction energy and is written as a function of the phase-field variables as

$$E = \int_V \left[F(c_v, c_v, \eta, T) + \frac{\kappa^2}{2}|\nabla \eta|^2 + U^{def}(\varepsilon_{ij}) \right] dV \,, \tag{1}$$

where V is the system volume, $F(c_v, c_g, \eta, T)$ is the chemical free energy density, T is absolute temperature, κ is the gradient coefficient associated with interfacial energy of gas bubbles, U^{def} is the elastic energy density associated with the lattice mismatch of the defects including distributed gas bubbles, vacancies, and gas atoms, and ε_{ij} $(i, j = 1,2,3)$ are elastic strain components.

Following the Kim's solidification model [1], the chemical free energy density of the system is constructed as

$$F(c_v, c_g, \eta, T) = [1 - h(\eta)] f^m\left(c_v^m, c_g^m, T\right) + h(\eta) f^b\left(c_v^b, c_g^b, T\right) + w g(\eta) \,, \tag{2}$$

where (f^m, f^b), $(c_v^m,\ c_g^m)$ and (c_v^b, c_g^b) are the chemical free energy densities, vacancy and gas concentrations of the matrix and of the gas bubble phases, respectively. $g(\eta)$ is a double-well potential, for example, the simplest form is $g(\eta) = \eta^2(1-\eta)^2$ and w is the height of the double well potential. $h(\eta) = 3\eta^2 - 2\eta^3$ is an interpolation function describing the volume fraction of gas bubble phase. The Kim's model assumes that any point within the interface region is considered as a mixture of the matrix and gas bubble phases with the same inter-diffusion potential. Therefore, the concentrations satisfy the following chemical equilibrium and mass balance equations,

$$c_v = [1 - h(\eta)] c_v^m + h(\eta) c_v^b \,, \tag{3a}$$

$$c_g = [1 - h(\eta)] c_g^m + h(\eta) c_g^b \,, \tag{3b}$$

$$\frac{\partial f^m\left(c_v^m, c_g^m, T\right)}{\partial c_v^m} = \frac{\partial f^b\left(c_v^b, c_g^b, T\right)}{\partial c_v^b} \,, \tag{3c}$$

$$\frac{\partial f^m\left(c_v^m, c_g^m, T\right)}{\partial c_g^m} = \frac{\partial f^b\left(c_v^b, c_g^b, T\right)}{\partial c_g^b}. \tag{3d}$$

From eqs. (3a-3d), we can obtain $(c_v^m,\ c_g^m)$ and (c_v^b, c_g^b) for given (c_v, c_g).

Chemical free energies of the matrix and gas bubble phases

With ideal solution assumption, the chemical free energy density of the matrix phase with vacancy and gas concentration $c_v(\mathbf{r},t)$ and $c_g(\mathbf{r},t)$ can be written as

$$\begin{aligned} f^m(c_v^m, c_g^m, T) = \frac{1}{\Omega}\{ & \Re T[c_v^m \ln(c_v^m) + (1-c_v^m)\ln(1-c_v^m)] + N_A E_v^f c_v^m \\ & + \Re T[c_g^m \ln(c_g^m) + (1-c_g^m)\ln(1-c_g^m)] + N_A E_g^f c_g^m \}, \end{aligned} \tag{4}$$

where $\Re = 8.314$ $[\mathrm{J}/(\mathrm{mol}\cdot\mathrm{K})]$ is the gas constant, $N_A = 6.022\times10^{23}$ $[\mathrm{mol}^{-1}]$ is the Avogadro constant. E_v^f and E_g^f are the formation energies of a vacancy and a gas atom, respectively. Ω is the molar volume of UO_2 and Ω=2.53×10^{-5} [m^3/mol].

In simulations, $f^m(c_v^m, c_g^m, T)$ is replaced approximately by parabolic functions as

$$f^m(c_v^m, c_g^m, T) = A_{12}\left(c_v^m - c_v^{m,eq}\right)^2 + B_{12}\left(c_g^m - c_g^{m,eq}\right)^2, \tag{5}$$

where $c_v^{m,eq} = \exp\left(-E_v^f / k_B T\right)$ and $c_g^{m,eq} = \exp\left(-E_g^f / k_B T\right)$ are the thermal equilibrium solubility of vacancies and gas atoms, respectively. k_B =1.381×10^{-23} [J/K] is the Boltzmann constant. Both $f^m(c_v^m, c_g^m, T)$ in eqs. (4) and (5) have the same first derivatives at a given concentration (c_v^0, c_g^0).

If assuming a UO_2 vacancy has the same formation energy as a Xenon atom, $E_v^f = E_g^f = E^f$ =3 eV. In the following simulations, $(c_v^0, c_g^0) = (0.01, 0.01)$, $B_{12} = A_{12}$ and

$$\frac{A_{12}}{C_{44}} = \frac{-a_2 + 3a_1}{4\left(c_v^0 - c_v^{m,eq}\right)} + \frac{a_2 - a_1}{2400\left(c_v^0 - c_v^{m,eq}\right)} T,$$

$$a_1 = 0.178605 - 0.0030782\log\left(1-c_v^0\right) + 0.0030782\log\left(c_v^0\right),$$

$$a_2 = 0.178605 - 0.00923461\log\left(1-c_v^0\right) + 0.00923461\log\left(c_v^0\right),$$

with C_{44}=64 [GPa].

The chemical free energy density of the gas bubble phase, for the sake of simplicity, is assumed to be parabolic functions of c_v^b and c_g^b as

$$f^b\left(c_v^b, c_g^b, T\right) = A_{22}\left(c_v^b\right)^2 + A_{21}c_v^b + A_{20} + B_{22}\left(c_g^b\right)^2 + B_{21}c_g^b + B_{20}. \tag{6}$$

If $c_v^{b,eq}$ and $c_g^{b,eq}$ are the equilibrium concentrations of the gas bubble phase, $c_v^{b,eq} = 1$ and $c_g^{b,eq}$ can be obtained from the equation of state of Xenon. We used Ronchi's results of Xenon [5] to determine $c_g^{b,eq} \approx 0.7$ (see Fig. 1). The left two unknown coefficients (e.g., A_{22} and B_{22}) will be determined by given ($c_v^{cross}, c_v^{cross}; f^{cross}$), i.e., $f^m\left(c_v^{cross}, c_v^{cross}, T\right) = f^b\left(c_v^{cross}, c_v^{cross}, T\right) = f^{cross}$. Therefore,

$$A_{22} = \frac{A_{12} f^{cross}}{\left(\sqrt{A_{12}}\left(c_v^{m,eq} - c_v^{b,eq}\right) + \sqrt{f^{cross}}\right)^2}, \quad B_{22} = \frac{B_{12} f^{cross}}{\left(\sqrt{B_{12}}\left(c_g^{m,eq} - c_g^{b,eq}\right) + \sqrt{f^{cross}}\right)^2}.$$

If $\frac{f^{cross}}{C_{44}} = 0.5$, then

$$T = 1100\ K,\ \frac{f^m\left(c_v^m, c_g^m, T\right)}{C_{44}} = 7.63367\left(c_v^m - c_v^{m,eq}\right)^2 + 7.63367\left(c_g^m - c_g^{m,eq}\right)^2,$$

$$\frac{f^b\left(c_v^b, c_g^b, T\right)}{C_{44}} = 0.90311\left(c_v^b - c_v^{b,eq}\right)^2 + 2.5355\left(c_g^b - c_g^{b,eq}\right)^2;$$

$$T = 1800\ K,\ \frac{f^m\left(c_v^m, c_g^m, T\right)}{C_{44}} = 6.80856\left(c_v^m - c_v^{m,eq}\right)^2 + 6.80856\left(c_g^m - c_g^{m,eq}\right)^2,$$

$$\frac{f^b\left(c_v^b, c_g^b, T\right)}{C_{44}} = 0.940819\left(c_v^b - c_v^{b,eq}\right)^2 + 2.71669\left(c_g^b - c_g^{b,eq}\right)^2;$$

$$T = 2100\ K,\ \frac{f^m\left(c_v^m, c_g^m, T\right)}{C_{44}} = 6.45494\left(c_v^m - c_v^{m,eq}\right)^2 + 6.45494\left(c_g^m - c_g^{m,eq}\right)^2,$$

$$\frac{f^b\left(c_v^b, c_g^b, T\right)}{C_{44}} = 0.960011\left(c_v^b - c_v^{b,eq}\right)^2 + 2.1188\left(c_g^b - c_g^{b,eq}\right)^2.$$

Their plots can be seen in Fig. 2.

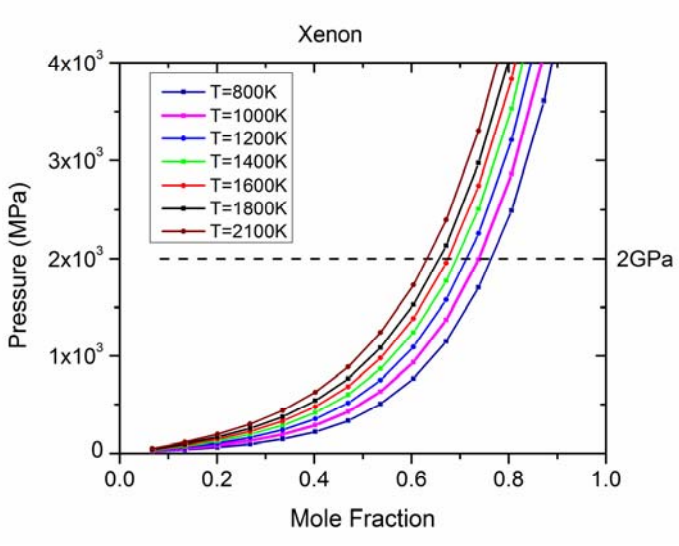

Fig. 1. Pressure versus Xenon mole fraction at different temperature. [5]

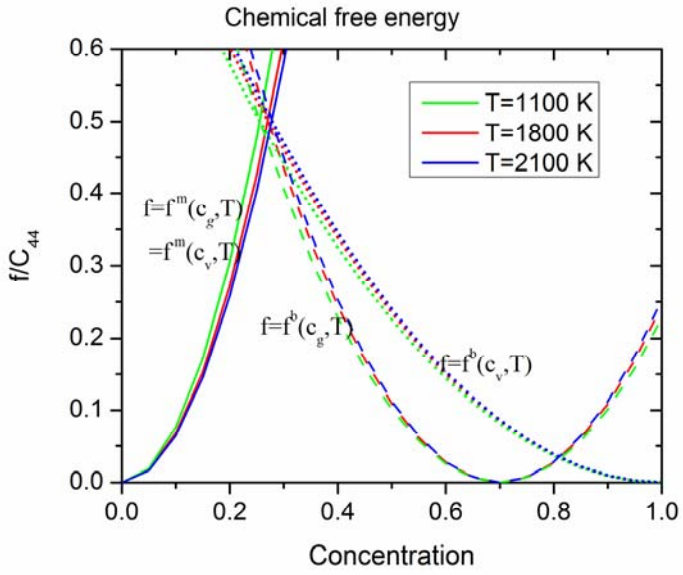

Fig. 2. Chemical free energies used in our simulations.

Elastic energy density

The last term of the right side of eq. (1) is the elastic energy. If we assume that the variation of stress-free lattice parameter of the matrix phase, a, with the given concentrations of vacancies and gas atoms, obeys the Vegard's law, the local stress-free strain caused by the defect inhomogeneity is given by

$$\varepsilon_{ij}^{*m} = \left[\varepsilon^{v0}\left(c_v - c_v^{m,eq}\right)\delta_{ij} + \varepsilon^{g0}\left(c_g - c_g^{m,eq}\right)\delta_{ij}\right](1-h(\eta)), \tag{7}$$

where $\varepsilon^{v0} = (1/a)da/dc_v$ and $\varepsilon^{g0} = (1/a)da/dc_g$ are the expansion coefficients of the lattice parameter due to the introduction of vacancies and interstitials, respectively, and δ_{ij} is the Kronecker-delta function. The vacancy and gas concentrations are high in the gas bubble phase where the Vegard's law may no long be applicable. The stress-free strain in the gas bubble phase is described as

$$\varepsilon_{ij}^{*b}(\mathbf{r}) = \varepsilon^{b0}(c_g, T)\delta_{ij}h(\eta), \tag{8}$$

where $\varepsilon^{b0}(c_g, T)$ can be estimated as $\varepsilon^{b0}(c_g, T) = P/(C_{11} + 2C_{12})$ where *P* is the pressure inside of the gas bubble phase and can be obtained from the equation of state, and C_{11} and C_{12} are the elastic constants of the gas bubble phase. Thus, the total stress-free strain tensor is

$$\begin{aligned}\varepsilon_{ij}^{*} &= \varepsilon_{ij}^{*m} + \varepsilon_{ij}^{*b} \\ &= \left[\varepsilon^{v0}\left(c_v - c_v^{m,eq}\right)\delta_{ij} + \varepsilon^{g0}\left(c_g - c_g^{m,eq}\right)\delta_{ij}\right]\left[1-h(\eta)\right] + \varepsilon^{b0}(c_g, T)\delta_{ij}h(\eta).\end{aligned} \tag{9}$$

The elastic energy density U^{def} is calculated by:

$$U^{def} = \frac{1}{2}\lambda_{ijkl}\varepsilon_{ij}^{el}\varepsilon_{kl}^{el}, \tag{10}$$

where the summation convention over the repeated indexes is used. λ_{ijkl} is the elastic constant tensor of the system (its Voigt notation is C_{ij}). ε_{ij}^{el} is the elastic strain which is calculated by

$$\varepsilon_{ij}^{el} = \bar{\varepsilon}_{ij} + \delta\varepsilon_{ij}(\mathbf{r}) - \varepsilon_{ij}^{*}(\mathbf{r}), \tag{11}$$

where $\bar{\varepsilon}_{ij}$ is the homogeneous strain characterizing the macroscopic shape and volume change, $\delta\varepsilon_{ij}(\mathbf{r})$ is the heterogeneous strain of $\int_V \delta\varepsilon_{ij}(\mathbf{r})dV = 0$. For elastic inhomogeneous solids, such as UO_2 matrix with voids and gas bubbles, the elastic solution can be obtained using iteration methods [6]. For simplicity, we assume the gas phase has the same elastic constants as UO_2 and of cubic anisotropy with C_{11}/C_{44}=6.17, C_{12}/C_{44}=1.89. [7]

Kinetic equations

In all phase-field models, the temporal and spatial evolution of the field variables follows the same set of kinetic equations. A conserved field, e.g., concentration field c, evolves with time according to the Cahn-Hilliard equation [8], whereas a non-conserved field, e.g., the order parameter field η, is governed by the Allen-Cahn equation [9]. The evolution equations of c_v, c_g, and η are written as

$$\frac{\partial c_v}{\partial t} = \nabla \cdot \left\{ M_{vv} \nabla \left(\frac{\partial \left(F + U^{def} \right)}{\partial c_v} \right) \right\} + \dot{\omega}(\rho_{dis}, c_v, \sigma_{ij}), \tag{11}$$

$$\frac{\partial c_g}{\partial t} = \nabla \cdot \left\{ M_{gg} \nabla \left(\frac{\partial \left(F + U^{def} \right)}{\delta c_g} \right) \right\}, \tag{12}$$

$$\begin{aligned} \frac{\partial \eta}{\partial t} &= -L \frac{\delta E}{\delta \eta} = -L \left(\frac{\partial F}{\partial \eta} + \frac{\partial U^{def}}{\partial \eta} - \kappa^2 \nabla^2 \eta \right) \\ &= -L \left\{ -\kappa^2 \nabla^2 \eta + w g'(\eta) + h'(\eta) \left[-\left(f^m - f^b \right) + (c_v^m - c_v^g) \frac{\partial f^m}{\partial c_v^m} + (c_g^m - c_g^g) \frac{\partial f^m}{\partial c_g^m} \right] + \frac{\partial U^{def}}{\partial \eta} \right\}, \end{aligned} \tag{13}$$

where M_{vv} and M_{gg} represent the mobility of vacancies and gas atoms and are determined from the diffusivity by $M_{vv} = D / \left(\frac{\partial^2 f^m}{\partial c_v^2} \right)\Big|_{c_v = c_v^{m,eq}}$ and $M_{gg} = D / \left(\frac{\partial^2 f^m}{\partial c_g^2} \right)\Big|_{c_g = c_g^{m,eq}}$. L is the interface mobility coefficient.

$\dot{\omega}(\rho_{dis,} c_v, \sigma_{ij})$ is the vacancy emission rate which depends on dislocations ρ_{dis}, local stress σ_{ij}, and vacancy concentration $c_v(\mathbf{r}, t)$.

Diffusivity, Mobility and interfacial energy

Assume vacancies and gas atoms have the same diffusivity of $D = 0.5 \times 10^{-4} \exp\left[-11604.5 E_m / T \right]$ [m^2/s] with E_m being vacancy or gas atom migration energy in eV. Their temperature dependence and the corresponding mobility $M_{vv} = M_{gg} = M$ can be seen in Fig. 3 and Fig. 4, respectively. Taking $t = l_0^2 / (C_{44} M)$, as a real time scalar with l_0= 1 nm, this scalar has a huge difference between T=800 K and T=2200 K as shown in Fig. 5.

In the Kim's model, the interfacial energy γ and interface thickness 2λ are associated with the gradient coefficient κ and the height w of the double well potential as

$$\gamma = \frac{\kappa\sqrt{w}}{3\sqrt{2}}, \tag{14}$$

$$2\lambda = \alpha\sqrt{2}\frac{\kappa}{\sqrt{w}}, \tag{15}$$

where α is a dimensionless coefficient and takes value of ~2.2.

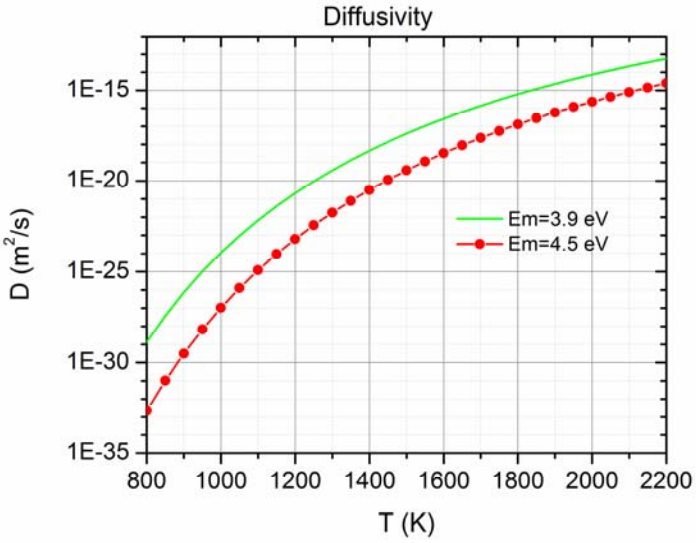

Fig. 3. Diffusivity versus temperature.

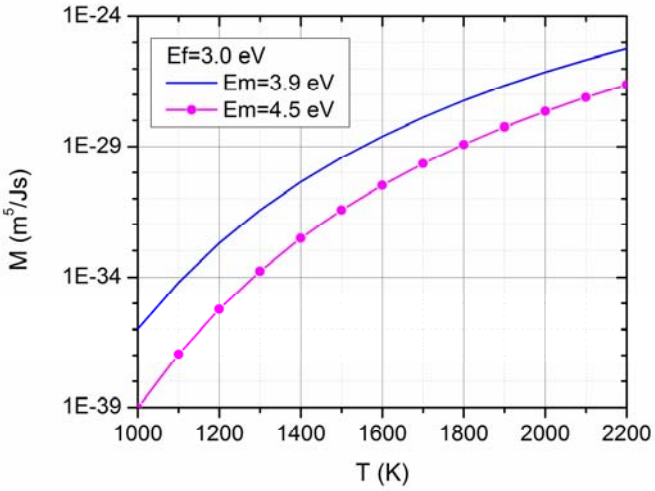

Fig. 4. Mobility versus temperature.

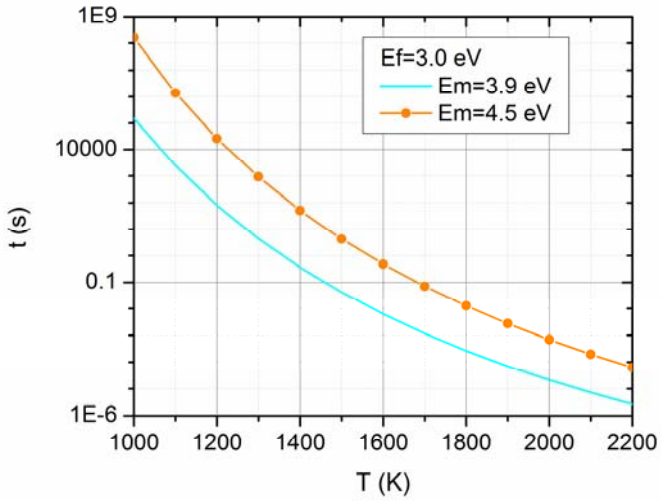

Fig. 5. Time scalar versus temperature.

A-3. Simulation results and analysis

Evaluation of the thermodynamic model by testing the critical sizes of gas bubbles

Based on classical nucleation theory chemical free energy, elastic energy and interfacial energy determine the critical size of gas bubbles. Before we simulate the gas bubble growth kinetics, we first evaluate the effect of concentration and elastic interaction on the critical size of gas bubbles. In the simulations, a gas bubble with different sizes was embedded at the center of a three dimensional simulation cell 96dx×96dy×96dz. Periodic boundary conditions in x-,y- and z- directions were imposed. Grad size dx=dy=dz=0.25 nm was used. The simulation was performed at 2100 K. The evolution of gas bubble radius versus time is plotted in Figure 6a. The initial vacancy concentration and Xe concentration in the matrix were given with the same value. It is seen from Figure 6a that when the radius of gas bubble is less than 0.4nm the gas bubble shrinks for the studied four cases with different vacancy and Xe concentrations in the matrix and with/without elastic interaction; when the radius of gas bubble is larger than 0.8nm the gas bubble grow for studied four cases. Gas bubbles with the radius between 0.4nm and 0.8nm may grow or shrink depending on the concentration and elastic interaction. Therefore, the critical size of gas bubble is about 0.8nm for the given free energy, interfacial energy and elastic interaction energy. The critical size increases with the decreasing vacancy and Xe concentrations. Pressure and shear stress distributions on the xy plane which crosses the center of the gas bubble are presented in Figure 6b. We found that the pressure inside the gas bubble is about 1.6GPa that is consistent with the equation of state. In addition, the pressure inside the gas bubble causes a long range elastic field near the gas bubble, which affects gas bubble

growth kinetics as well as critical size of gas bubbles. The results in Figure 6a show that the elastic interaction increases the critical size of gas bubble.

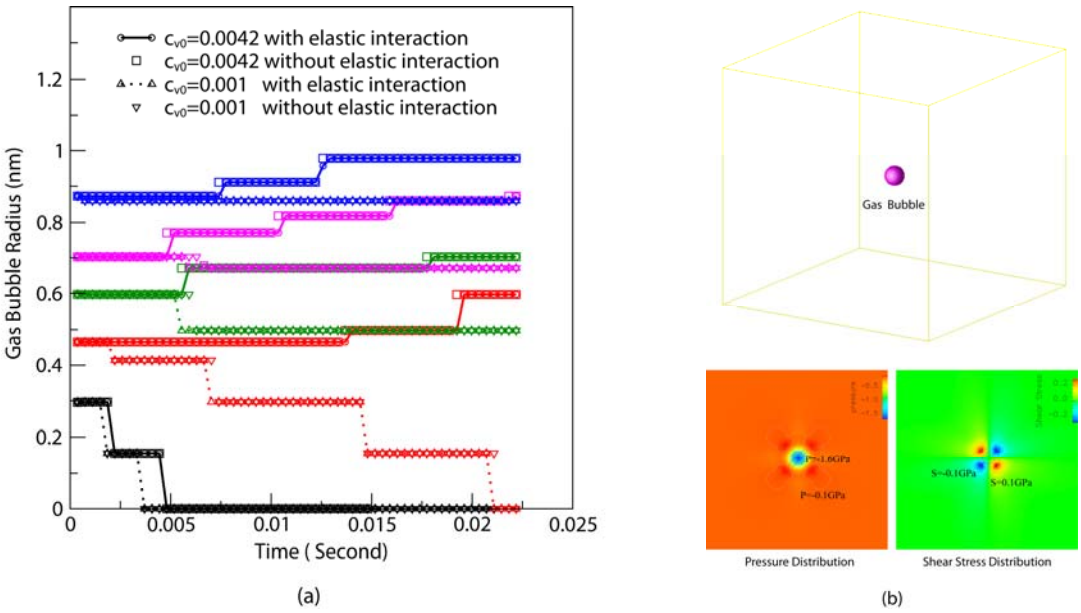

Fig. 6. (a) Concentration and elastic interaction dependence of gas bubble critical size, (b) pressure and shear stress around the gas bubble.

Evaluation of thermodynamic model by testing gas bubble evolution kinetics in 3D at 2100K

Gas bubble growth kinetics was examined at constant temperature 2100K in 3D. The simulation started with a random gas bubble distribution in a 128dx×128dy×36dz simulation cell. Grad size dx=dy=dz=1nm was used. The initial gas concentration was 0.0042. The effect of elastic interaction and initial vacancy concentration on gas bubble growth kinetics is shown in Fig. 7. The gas bubble evolution can be divided into three stages as marked in Fig. 7(b). At first stage, gas bubbles with sizes smaller than the critical size quickly dissolve; the second stage is gas babble growth due to the super saturation of vacancies and Xe atoms in the matrix; and the third stage is gas bubble coarsening (Ostwald ripening). The sharp decreases of gas bubble number and gas bubble volume fraction at early stage corresponds to the first stage as shown in Figs. 7(a,b,c). The following increase of gas bubbles volume fraction and constant or slowly decrease of gas bubble number correspond to the second growth stage. During a perfect growth stage, it is expected that the number of gas bubble keeps constant. However, simulation results show that it decreases slowly. The reason for this could be inhomogeneous spatial distribution of initial gas bubbles which causes local Ostwald Ripening at an early stage. Although the modeling has not yet reached the final Ostwald ripening stage, it is expected by the thermodynamic model that the gas bubble volume fraction

should keep constant while the number of gas bubbles decreases slowly. In addition, it is found that 1) the gas bubble density reduces faster with decreasing vacancy concentration and 2) elastic interaction also speeds up the reduction of gas bubble density shown in Figs. 7(a,6). These results are consistent with their effect on the critical size of gas bubbles.

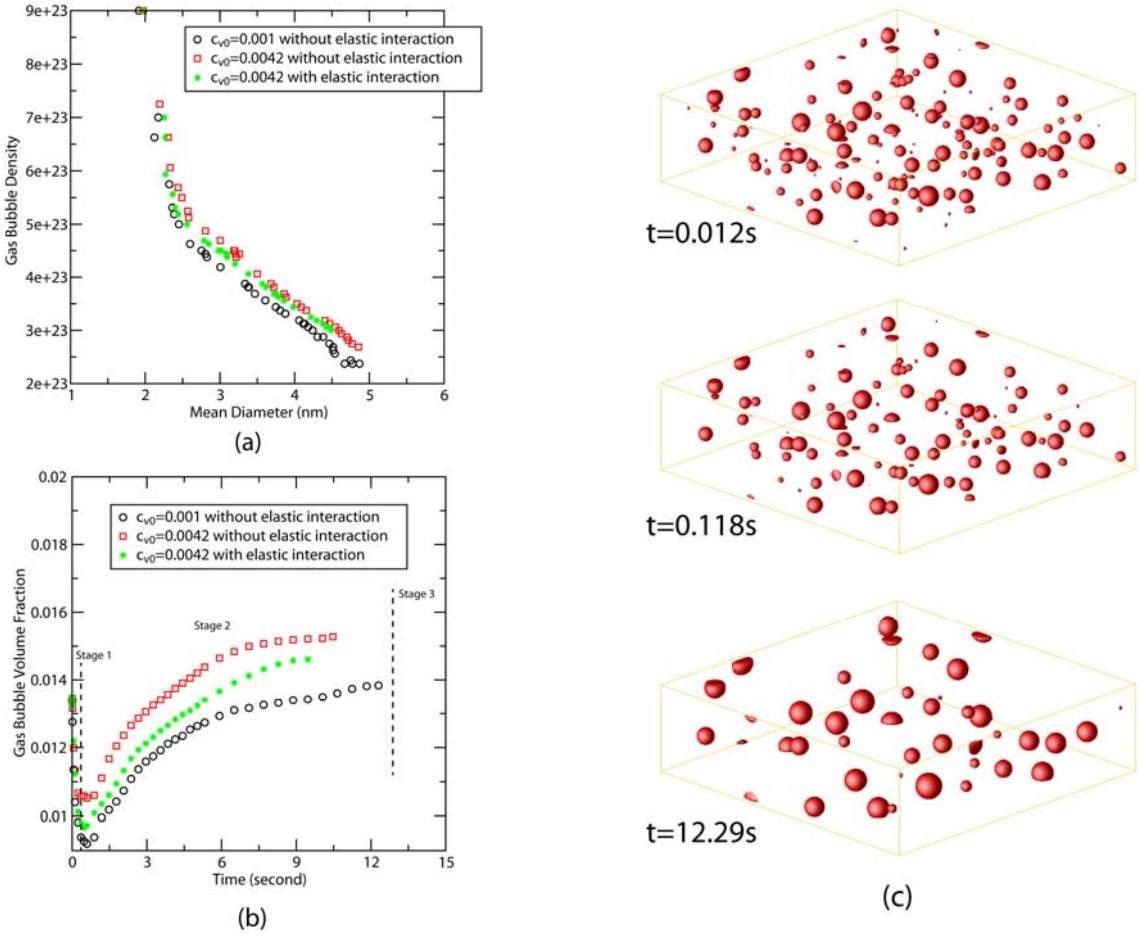

Fig. 7. (a) Gas bubble density in a function of gas bubble mean diameter; (b) gas bubble volume fraction vs time, and (c) time evolution of gas bubble morphology for the case $c_{v0} = 0.001$ with elastic interaction.

Kashibe et al. [10] found that a linear relationship between the double logarithmic bubble number density and mean bubble diameter fitting well their experimental data:

$$\log N_b = -2.6 \log d_b + 25.1 \quad \text{or} \quad \log N_b = \log(d_b)^{-2.6} + 25.1$$

where N_b is bubble density in a cubic meter volume and d_b is mean bubble diameter. Figure 8 plots the fitted experiment results and our simulation results. The simulation results also show a linear relationship between the double logarithmic gas bubble density and mean gas bubble diameter but in a different slop. It is noticed that reducing vacancy concentration makes the slop closer to the experimental relationship.

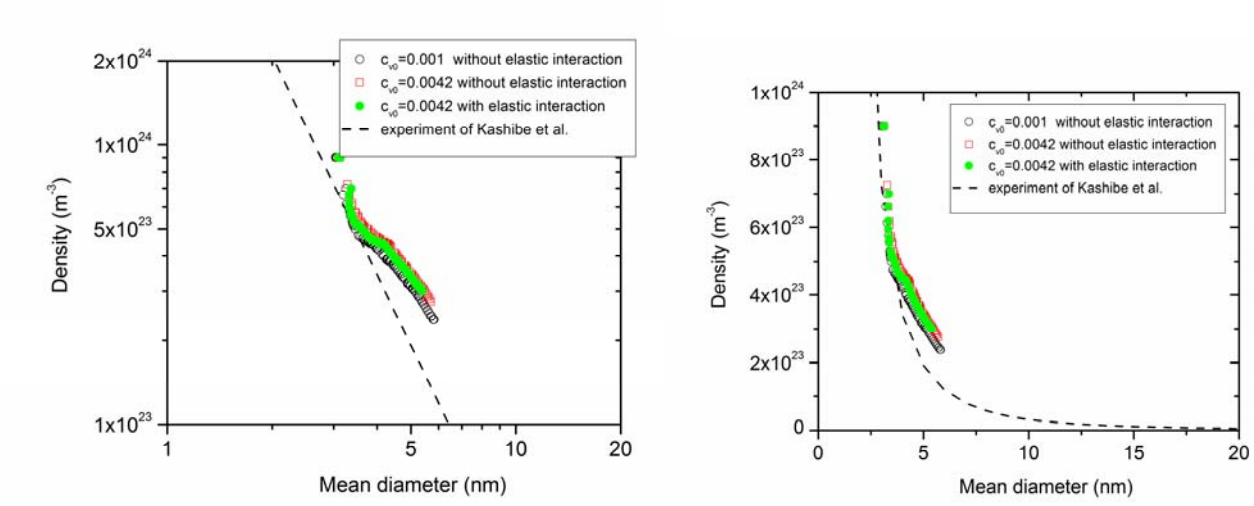

Fig. 8. Relationship between gas bubble density and mean gas bubble diameter from experiments and simulations.

Effect of vacancy emission on gas bubble evolution in 2D at 2100K

Experiments [2] suggested that gas bubble growth is severely restricted by vacancy starvation effects under out-of-pile conditions. The effect of vacancy concentration and vacancy emission from dislocations on gas bubble evolution is simulated. The simulations consider two cases. One is homogeneous vacancy emission. In this case, there is uniform vacancy generation with a generation rate $\dot{\omega} = \omega_0^2 \rho$ where ρ is dislocation density, and ω_0^2 is emission strength. The other way is inhomogeneous vacancy emission. In this case, the vacancy emission is from individual dislocation with an emission rate $\dot{\omega} = \omega_0^2$. Figures 9 and 10 show the snap shots of the gas bubble morphology at t=2 minutes. The simulations were done in 2D with a simulation cell 256dx×256dy at 2100K, and dx=dy=1nm. Initially 59 gas bubbles were randomly distributed in the simulation cell with gas concentration 0.0042 and vacancy concentration 0.001. Dislocations act as sources of vacancy emission. It is clear that gas bubbles in Fig. 9(a) grow bigger with vacancy emission compared to Figure 9(a) without vacancy emission. Smaller gas bubbles still survive although their counterparts already disappeared without vacancy emission.

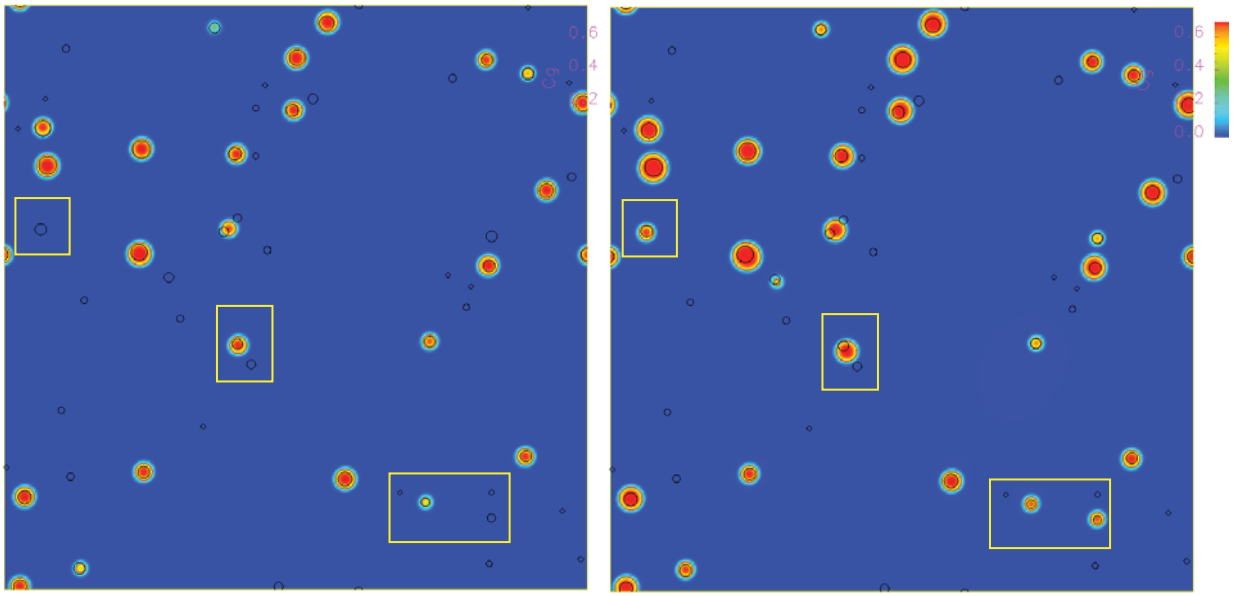

(a) (b)

Fig. 9. Gas bubble morphology (a) without vacancy emission, and (b) with homogeneous vacancy emission. The black circles identify the initial gas bubbles. The framed parts illustrate the obvious difference between without and with vacancy emission.

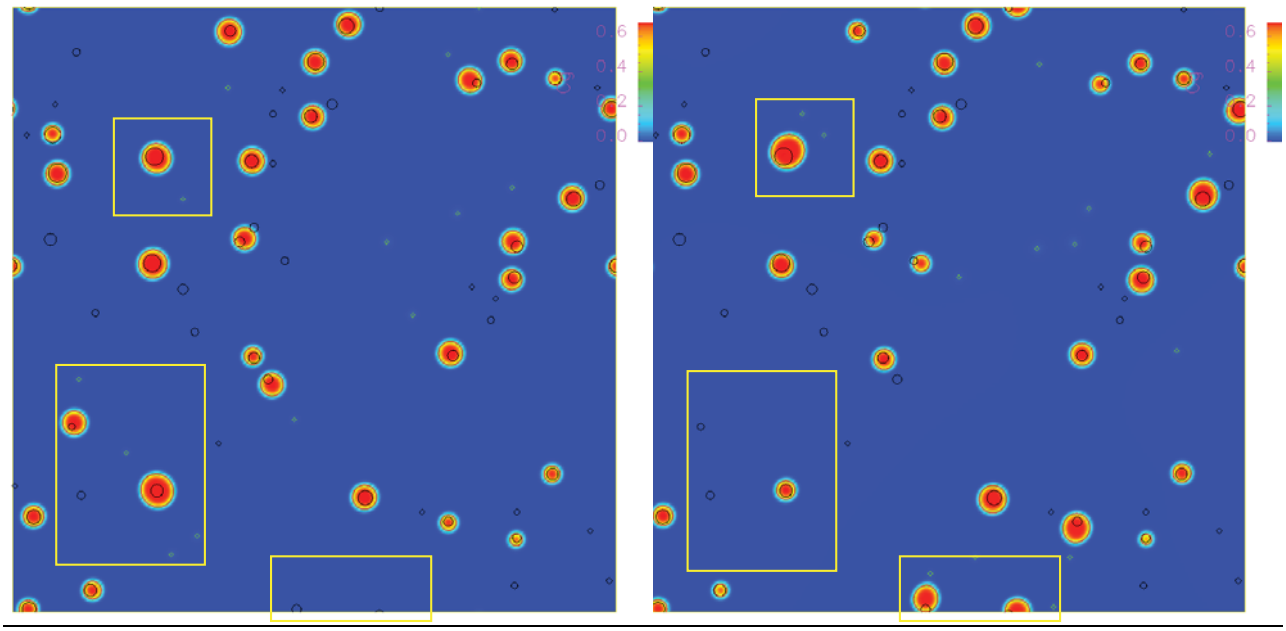

(a) (b)

Fig. (10). Gas bubble morphology (a) and (b) with vacancy emission from different distributed dislocations. The light blue dots denote the location of dislocations while the black circles identify the initial gas bubbles. The framed parts illustrate the obvious difference due to the local vacancy emission.

For inhomogeneous vacancy emission cases, we randomly distributed the dislocations in the simulation cell with a dislocation density $2x10^{14}$. Figure 10 shows the gas bubble morphology for two different dislocation distributions. We can see that inhomogeneous vacancy emission causes the inhomogeneous growth. The gas bubbles near dislocations grow bigger because the dislocation continuously supplies vacancies. Therefore, an abnormal bubble size distribution with a long exponential tail observed in White's experiment [2] may be from the vacancy emission from inhomogeneous dislocation distributions. However, these are qualitative results. For examining the effect of vacancy emission from dislocations, we need the vacancy emission rate from dislocations.

Gas bubble growth kinetics in 2D during annealing from 1100K to 2100K

Gas bubble evolution during annealing is also simulated in two dimensions. The simulation cell and initial gas bubble distribution are the same as that in previous section. The vacancy and gas concentrations are 0.0042. The annealing started from 1100K and temperature increases in a rate of 2K/s. Three simulations with different initial gas bubble distributions were run. Evolution of gas bubble number and gas volume fraction are plotted in Fig. 11. It is seen from Fig. 11(a) that at the low temperature the gas bubble is frozen due to small diffusivity. With increasing temperature, the small bubbles become unstable and a sharp drop of gas bubble number is observed at T=1400K. After that there is a short period when the number of gas bubbles is almost constant. Then the bubble number linearly decreases. The volume fraction evolution in Fig. 11(b) also shows the freezing, dissolving and growing stages. A comparison between experiment and modeling results of gas bubble density and mean gas diameter is plotted in Fig. 12. A linear relationship between the double logarithmic bubble density and mean bubble diameter during the gas bubble evolution was observed.

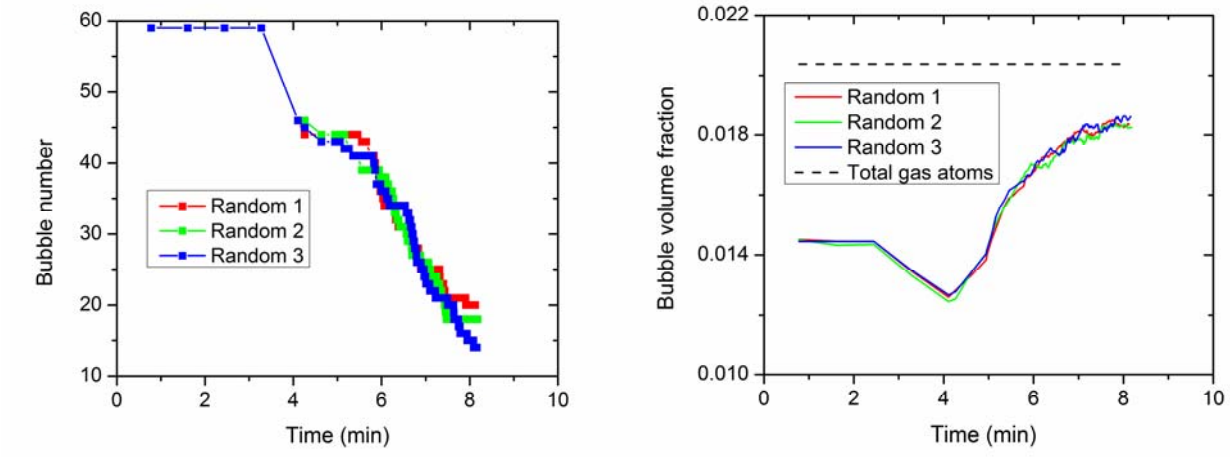

Fig. 11. Evolution of gas bubble number and volume fraction versus time..

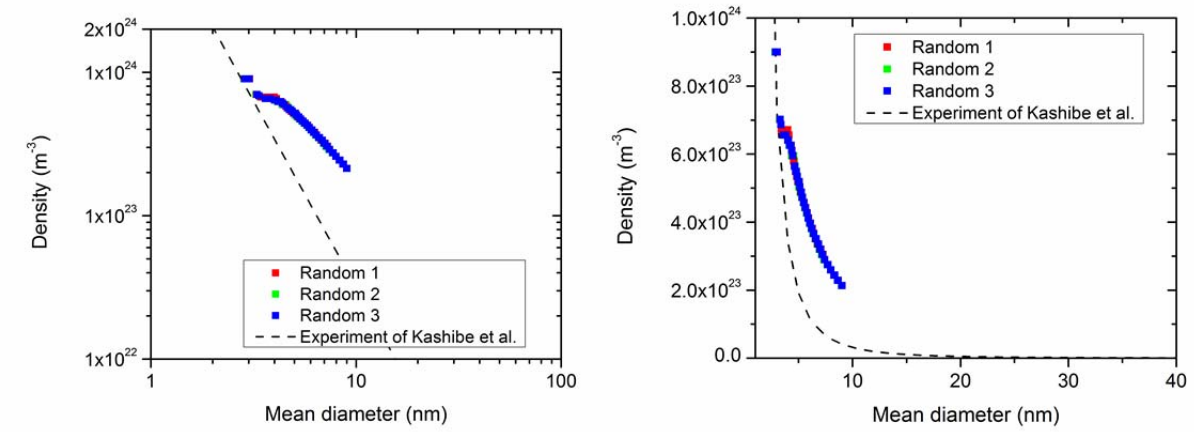

(a) (b)

Fig. 12. Comparison of gas bubble density versus mean diameters from phase-field model and experiments.

Evaluation of computational efficiency with FFTW

We have checked out the numerical efficiency of FFTW. Table 1 lists the CPU time for 10000 simulation time steps in 2D and 3D. What we found is that calculation of elastic interaction driving force takes about few percentage of CPU time.

Table 1. CPU time with 2.66GHz core for 10000 simulation time steps in 2D and 3D with/without elastic interaction.

Description	CPU time
2D simulation domain: 256×x256 without elastic interaction	0.0742h
2D simulation domain: 256×256 with elastic interaction	0.0757h
3D simulation domain: 128×128×36 without elastic interaction	1.24h
3D simulation domain: 128×128×36 without elastic interaction	1.36h

References

[1] S.G. Kim, W.T. Kim, T. Suzuki, Phys Rev E 60 (1999) 7186.

[2] R.J. White, The growth of intra-granular bubbles in post-irradiation annealed UO2 fuel, in: IAEA Technical committee on nuclear fuel behaviour modeling at high burn-up and its experimental support, Lake Windermere, UK, 2000.

[3] S.Y. Hu, C.H. Henager, Acta Mater 58 (2010) 3230.

[4] Y.L. Li, S.Y. Hu, X. Sun, F. Gao, C.H. Henager, M. Khaleel, J Nucl Mater 407 (2010) 119.

[5] C. Ronchi, J Nucl Mater 96 (1981) 314.

[6] S.Y. Hu, L.Q. Chen, Acta Materialia 49 (2001) 1879.

[7] J.B. Wachtman, M.L. Wheat, H.J. Anderson, J.L. Bates, J Nucl Mater 16 (1965) 39.

[8] J.W. Cahn, Acta Metall. 9 (1961) 795.

[9] J.W. Cahn, S.M. Allen, Le J. de Phys. Col. 38 (1977) 51.

[10] S. Kashibe, K. Une, K. Nogita, J Nucl Mater 206 (1993) 22.

Appendix B:

INL--Phase Field Models

Michael Tonks[a], Bulent Biner[a], Paul Millett[a], David Andersson[b]
[a] *Fuel Modeling and Simulation Department, Idaho National Laboratory*
[b] *MST-8, Los Alamos National Laboratory*

For INL's contribution to the FMM benchmark problem, we used the phase field method to represent the benchmark problem. The simulations were carried out using the MARMOT FEM-based phase-field modeling framework [2]. In this document, we begin by outlining our assumptions and describe our model. Then, we show 2-D results of the simulations and compare them to the experimental data. We end with an analysis investigating the sensitivity of the bubble growth to the initial bubble configuration and size distribution and show a small 3-D simulation.

B-1 Assumptions

As stated in section 3, Xe atoms in the UO_2 lattice tend to be located within a Schottky defect composed of one U vacancy and two O vacancies. Also, at high temperature, the Xe is transported through vacancy diffusion.

To completely capture Xe diffusion due to the vacancy mechanism, we would need to predict the evolution of the Xe concentration, as well as the O and U vacancy concentrations. The diffusion constants for the Xe concentration D_g, the U vacancy concentration D_v^U and the O vacancy concentration D_v^O are given in section 3, however we plot these values for reference from 1100 K to 2100 K in Figure 1.

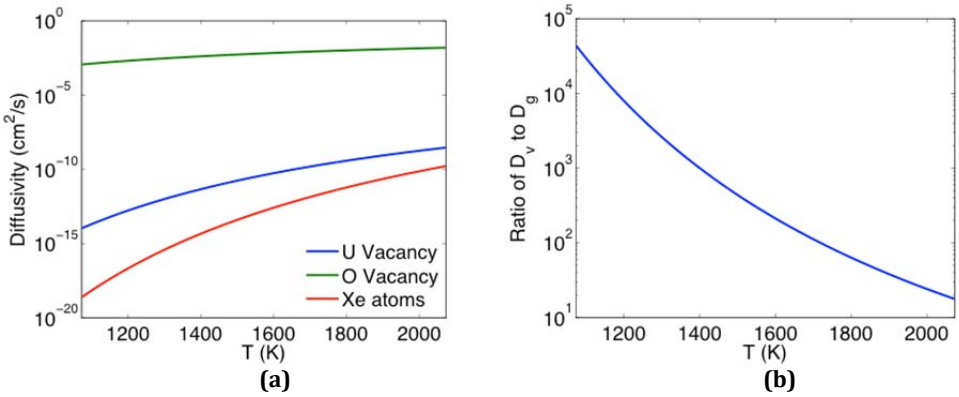

Figure 1: Diffusion constants of point defects in UO_2, where (a) compares the diffusion constants of U vacancies, O vacancies and Xe atoms at various temperatures and (b) shows the ratio of the diffusion constant of U vacancies to that of Xe atoms .

As can be seen in Fig. 1(a), the diffusivity of the O vacancies is over ten orders of magnitude higher than the diffusivity of U vacancies and Xe atoms. Since the highest diffusivities determine the time step size of the problem, this large difference appears to be problematic. The time step size would need to be very small to

capture the O vacancy diffusion, and therefore the total number of time steps needed to capture the bubble growth would be impractically high, even with the implicit time integration scheme used by MARMOT. Thus, in our model we only consider the Uranium sublattice, and we assume that the much faster moving O vacancies will be available for diffusion.

If we compare the diffusivities of U vacancies to Xe atoms, there is still a large difference, as can be seen in Fig. 1(b). The diffusion of the vacancies is nearly five orders of magnitude higher than that of the Xe at 1100 K, though it drops to only twenty times higher at 2100 K. This difference in the diffusivities would also be a significant problem, making it very difficult to reach long simulation times. Therefore, we further simplified our model by assuming that sufficient, fast-moving U vacancies will always be present in the material such that Xe is the only rate limiting species. Thus, the kinetics could be captured by only representing the Xe atoms in the model. In addition, our model does not consider the Brownian motion of the bubbles, and therefore primarily considers bubble growth due to Ostwald ripening rather than coalescence.

As stated in the problem description, the initial 1 nm radius bubbles are highly pressurized, due to their high initial gas concentration. The effect of the pressure could have a significant effect on the early stages of the bubble growth. However, as the bubbles grow, the pressure will decrease and the effect of pressure will become less significant. To simplify our simulations, we neglected the effect of pressure, though we will include the pressure effect in future simulations.

B-2 Model Description

With the simplifying assumptions discussed in the previous section, we now summarize the phase field model employed here. As stated above, we only considered the concentration of Xe atoms, c_g, and we further assumed that the gas concentration c_g = 1 within the bubbles. The free energy of the system is defined as:

$$E = N \int_V \left(F(c_g, T) + \kappa |\nabla c_g|^2 \right) \, dV \tag{2}$$

where N is the number of U sublattice sites per unit volume and the bulk free energy is given by

$$F = k_b T \left(c_g \ln c_g + (1 - c_g) \ln(1 - c_g) \right) + w \, c_g (1 - c_g) \tag{3}$$

In the bulk energy equation, k_b is the Boltzmann constant and w is assumed to equal the formation energy of Xe in the UO_2 matrix, where Ef_g = 4.35 eV. This model correctly represents the U vacancy equilibrium concentration but it does not allow the surface energy to be assigned. The bulk free energy from Eq. (3) can be difficult to solve numerically, due to the natural log terms being undefined at a value of zero. However, polynomial free energy functions have been shown to predict identical void/bubble growth as the free energy from Eq. (3), thus we substitute an eighth order polynomial free energy in place of Eq. (3), as shown in Fig. 2. This polynomial function is defined by

$$f_{loc} = 128\, W_8 \sum_{m=1}^{8} C_m^8\, c^m \tag{4}$$

where the coefficients are a function of the equilibrium concentration ($a = c_{eq}$) according to

$$\begin{aligned} C_8^8 &= 6 \\ C_7^8 &= \frac{96}{7}a - 24 \\ C_6^8 &= 48a + 8a^2 + 40 \\ C_5^8 &= -72a - 24a^2 - 36 \\ C_4^8 &= 30a^2 + \frac{75}{4} + 60a \\ C_3^8 &= -\frac{11}{2} - 20a^2 - 30a \\ C_2^8 &= \frac{3}{4} + \frac{15}{2}a^2 + 9\,a \\ C_1^8 &= -\frac{3}{2}a - \frac{3}{2}a^2 \end{aligned} \tag{5}$$

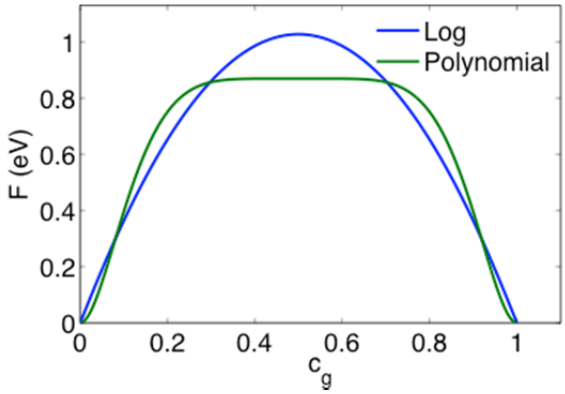

Figure 2: Bulk free energy as a function of gas concentration for the log free energy (Eq. (3)) and the polynomial free energy (Eq. (4)).

The evolution of the gas concentration is determined by solving the Cahn-Hilliard equation

$$\frac{\partial c_g}{\partial t} = \nabla \cdot M \nabla \frac{1}{N} \frac{\partial E}{\partial c_g} = \nabla \cdot M \nabla \left(\frac{\partial F}{\partial c_g} + \frac{\kappa}{2} \nabla^2 c_g \right) \tag{6}$$

The expression for the mobility is obtained with the fact that the migration behavior should follow the diffusion equation for $c_g << 1$, i.e.

$$f_{loc} = 128\, W_8 \sum_{m=1}^{8} C_m^8\, c^m \tag{7}$$

The values for the interfacial parameter κ and the barrier height W_8 were determined as functions of the surface energy and the interfacial width according to the method outlined in Moelans et al. [3]. In our simulations, we used an interfacial width of l_i = 0.7 nm. The value of the surface energy σ was calculated from the free energy defined in Eq. (3) according to the expression (see [3])

$$\frac{\partial c_g}{\partial t} = \nabla \cdot M \nabla \frac{1}{N} \frac{\partial E}{\partial c_g} = \nabla \cdot M \nabla \left(\frac{\partial F}{\partial c_g} + \frac{\kappa}{2} \nabla^2 c_g \right) \tag{8}$$

and its value is plotted vs. temperature in Fig. 3. All of the unique parameters used in our simulations are summarized in Table 1.

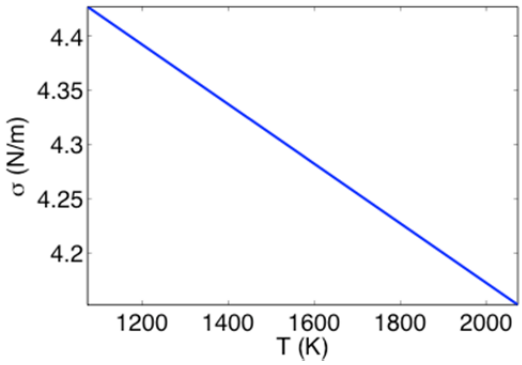

Figure 3: Plot of surface energy (from Eq. (8)) with temperature. Value is calculated from the free energy defined in Eq. (3).

Table 1: Summary of material parameters unique to our phase field model.

Parameter	Description	Value
l_i	Interfacial width	0.7 nm
c_{eq}	Approximate Xe gas equilibrium concentration	$e^{-\frac{\Omega \cdot \frac{3}{2}\sigma}{k_b T}}$
N	Number of U sublattice sites per unit volume	2.5×10^{28} m^{-3}

To solve the phase field equations, we discretize the domain using FEM. In addition, we employ implicit time integration. Thus, the Cahn-Hilliard equation (6) must be expressed as a residual equation and be converted to a "weak" form,

$$\begin{aligned} \mathbb{R}(c_g) = & \quad \frac{\partial c_g}{\partial t} - \nabla \cdot M \nabla \left(\frac{\partial F}{\partial c_g} + \kappa \nabla^2 c_g \right) = 0 \\ = & \quad \left(\frac{\partial c_g}{\partial t}, \phi_i \right) + \left(M \nabla \frac{\partial F}{\partial c_g}, \nabla \phi_i \right) + \left(\kappa \nabla^2 c_g, \nabla \cdot (M \nabla \phi_i) \right) \end{aligned} \tag{9}$$

where the boundary terms are not shown. Due to the second order derivative in the weak form, this system must be discretized using higher-order elements. In our simulations, we use the third-order Hermite element. Note that more information on solving the phase field equations using the MARMOT framework can be found in Tonks et al. [2].

B-3 Results and Discussion

To model post-irradiation annealing in UO_2, we use a 2-D simulation domain. We consider a 300 nm by 300 nm square of material, with two representative thicknesses in the z-direction (necessary to calculate the bubble density). We conduct one simulation with a z-thickness of 1 nm with 81 initial bubbles and one with a z-thickness of 10 nm with 841 initial bubbles. Both simulations start with an

average bubble radius of 1 nm, though the initial radius is varied randomly by ±20% for the 10 nm thickness (according to a uniform distribution) and ±25% for the 1 nm thickness. The initial condition of the simulation is created by uniformly placing the bubbles on a set lattice. The positions are then randomly varied in the x- and y-directions by up to ±4.5 nm for the 10 nm thickness (again, varied uniformly) and ±10.0 nm for the 1 nm thickness. Thus, the initial bubble density in the simulation was 9.3×10^{23} for the 10 nm thickness and 9.0×10^{23} for the 1 nm thickness. The gas concentration within the bubbles was assumed to be 1.0 and the initial gas concentration in the bulk was taken as 0.005.

As mentioned in the previous section, we discretize the domain using FEM. In addition, we take advantage of the adaptive mesh capability available in MARMOT, where the mesh is adapted according to a Laplacian error estimator [2]. The smallest element size used in both simulations is 0.42 nm and the largest is 6.67 nm. See Fig. 4 for the initial bubble configuration as well as a picture of the original mesh for both thicknesses.

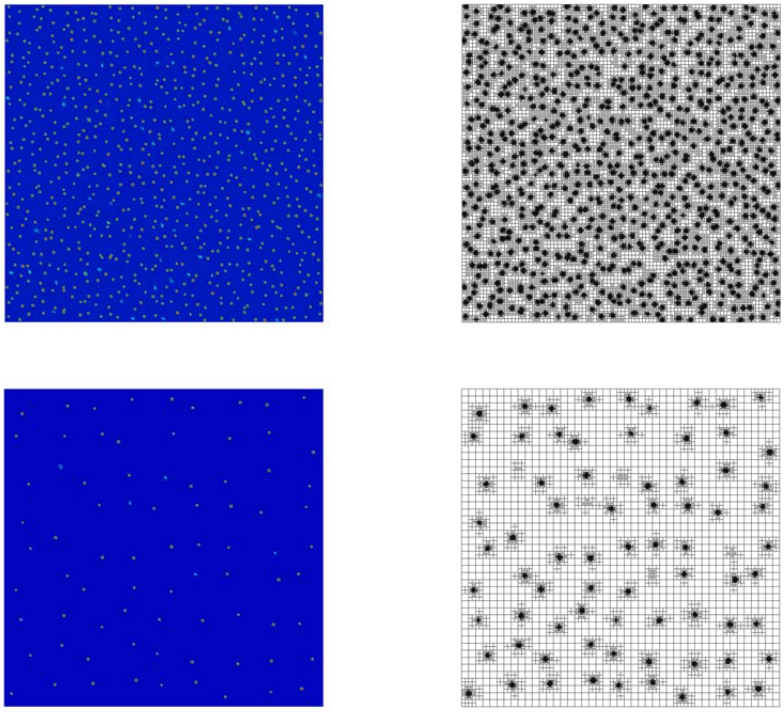

Figure 4: Initial bubble configuration for the 300 nm by 300 nm domain, with the fission gas concentration shown on the left and a view of the mesh on the right, where the 10 nm thickness simulation is shown above the 1 nm thickness.

We begin the simulation with an initial time step of 40 seconds, however as the temperature and diffusion constant increase (see Fig 1a), the time step must decrease. In addition, certain behaviors, such as the disappearance of a bubble, also require a smaller time steps. Therefore, we employ time step adaptivity. The time

step is adapted depending on the ratio of the time required to solve the nonlinear system to the physical time step size. See Tonks et al. [2] for more detail.
The 10 nm thickness simulation was run using 128 2.4 GHz AMD Opteron cores for nearly 2 weeks (320 hours). 12,814 time steps were taken, simulating 9.68 hours of bubble growth, with the number of bubbles going from 841 to 4. The 1 nm simulation was run with 64 2.4 GHz AMD cores for 38.5 hours. 19,348 time steps were taken to simulate 9.06 hours. The number of bubbles went from 81 to 1. Figure 5 shows the final bubble configuration and the final adapted FEM mesh for both thicknesses.

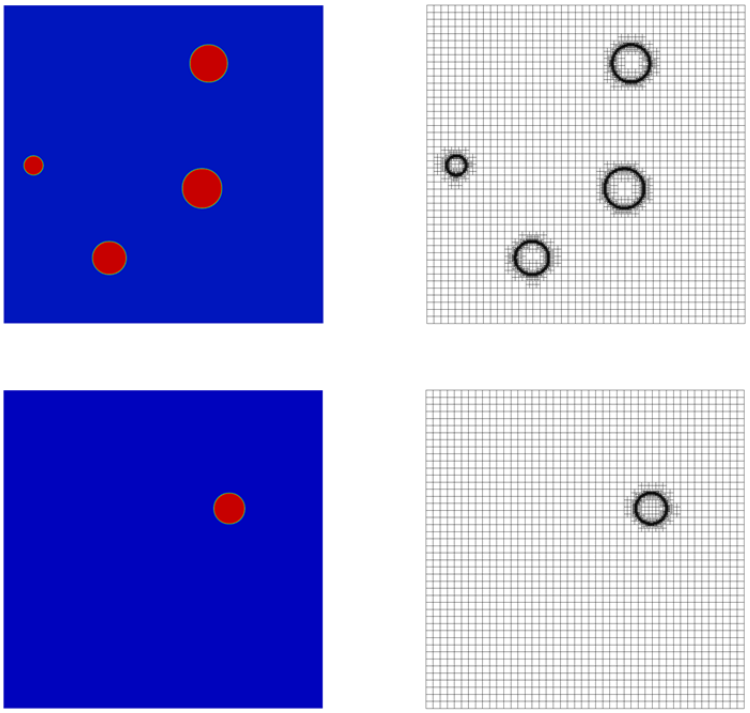

Figure 5: Post-irradiation annealing results, with the final configuration (left) and the final mesh (right), where the 10 nm thickness simulation is shown above the 1 nm thickness.

Throughout the simulations, the average bubble radius and the bubble density were calculated with time (Figure 6). The change in the average bubble radius predicted by the two simulations was nearly identical, with the deviation occurring once the 1 nm thick simulation had less than four bubbles remaining. The radius of the final bubble in the simulation with 1 nm thickness was 14.6 nm and the final mean bubble radius in the 10 nm thickness simulation was 12.9 nm.

The bubble density behavior with time predicted by the two simulations exhibited some significant differences. The bubble density first begins to decrease after 3.5 minutes for the 10 nm thickness simulation but after 3.5 minutes for the 1 nm thickness. The decrease in bubble density coincides with the increase in mean bubble radius for the 10 nm thickness simulation but not for the 1 nm thickness. We suspect that the delay in the radius increase is due to the time required for the gas

atoms to migrate the large distance between bubbles. The decrease in the density in the 1 nm thickness simulation is more rapid than the 10 nm until 4.2 minutes, at which time the decrease slows significantly. The bubble density decreases by nearly two orders of magnitude by the end of both simulations.

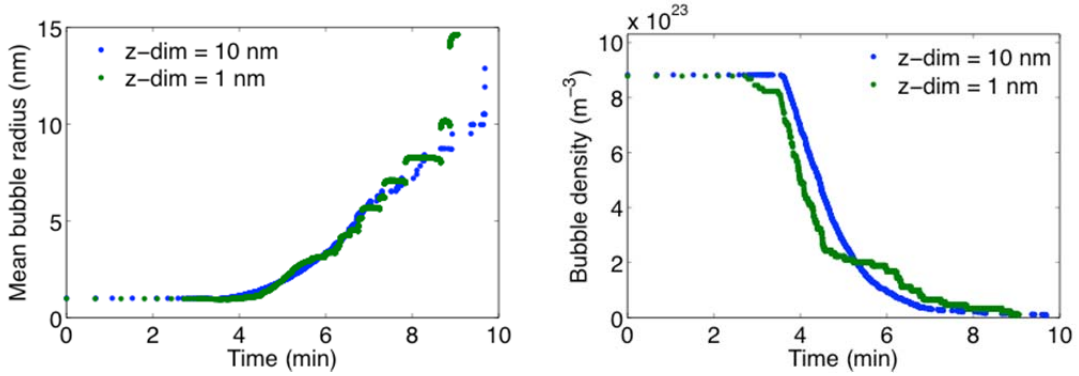

Figure 6: Post-irradiation annealing results, with the average bubble radius vs. time on the left and the bubble density vs. time on the right.

In Kashibe et al. [1], the authors determine a linear relationship between bubble number density and mean bubble diameter using a least-square fit to their experimental data, i.e.

$$\log N_b = -2.6 \log d_b + 25.1. \tag{10}$$

They compare this relationship to the data from other researchers and find good agreement. The results from our 10 nm thickness phase field simulation show fairly good agreement with the fit, as shown in Fig. 7. However, the 1 nm thickness simulation results do not show as good agreement. For the 1 nm thickness, the relationship between mean bubble diameter and bubble density clearly shows the lag between the drop in the density and the increase in the mean diameter due to the time required for diffusion of gas atoms between the bubbles. It is interesting to note that both simulations eventually predict the same slope on the log-log plot.

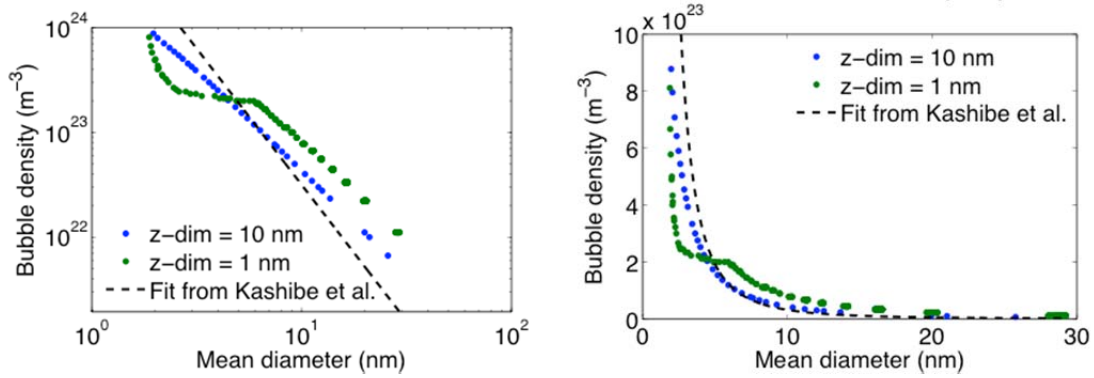

Figure 7: Comparison of the experimental fit of the relationship between bubble density and mean bubble diameter (from Kashibe et al. [1]) to the relationship predicted by our phase field simulations. The same figure is shown as a log-log plot (left) and a linear plot (right).

As mentioned previously, both mesh adaptivity and time step adaptivity were employed in our simulations to reduce the computational expense. To demonstrate their effect, we plot the degrees of freedom (DOFs) in the simulation vs. time as well

as the time step size vs. time for the 10 nm thickness simulation, a shown in Fig. 8. The results for the 1 nm thickness simulation are similar. In Figure 8(a), the DOFs are plotted together with the number of bubbles vs. time. From this plot it is clear that each time a bubble disappeared, fewer DOFs were needed to accurately represent the system. Thus, as time went on, the computational expense reduced dramatically. Due to the increase in the diffusion constant as the temperature increased, the time step reduced by many orders of magnitude over time (see Fig. 8(b) to see the time step size and the inverse of the diffusion constant). Though the time step size is quite noisy, due to the small time step required every time a bubble disappears, there is a clear relationship between it and the value of the diffusion constant.

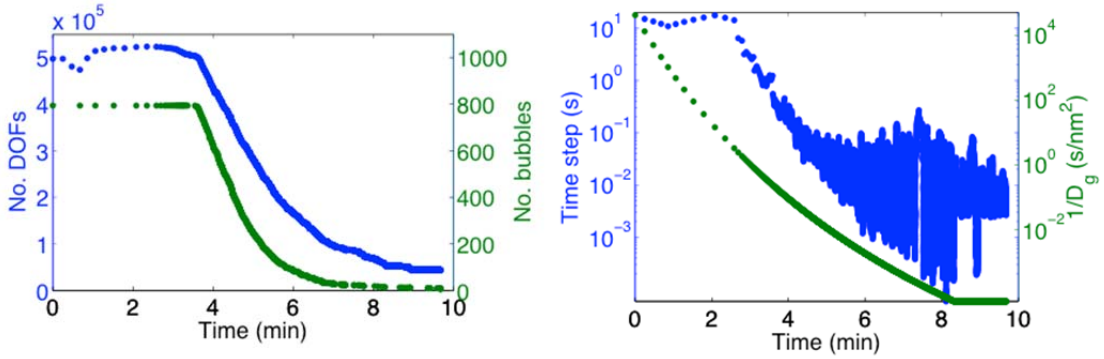

(a) **(b)**

Figure 8: The results of mesh and time step adaptivity for the 10 nm thickness simulation, where (a) shows the decrease in the number of degrees of freedom with time due to adapting the mesh, with the number of bubbles shown for reference, and (b) shows the time step size with time, with the inverse of the diffusion constant shown for reference.

To learn more about the physical behavior in this system, we conducted two additional analyses. The first investigates the impact of the initial condition of the bubbles on the bubble growth and the second investigates the impact of 3-D simulations on the relationship between mean bubble radius and bubble density.

Though the problem definition was formulated based on the experiments from Kashibe et al. [2], many details needed for the simulation were not available. One of these was the initial bubble configuration. The initial bubble density and the mean bubble radius were known, but the spatial configuration of the bubbles and the bubble size distribution were not. Therefore, we have made assumptions for these parameters. In order to determine the sensitivity of the bubble growth to these assumptions, we conducted several simulations on a 100 nm by 100 nm domain with 100 initial bubbles.

To investigate the sensitivity of the bubble growth to the bubble spatial configuration, we randomly varied the bubble locations from a uniform lattice by various amounts, ranging from max values ±1.5 nm to ±4.5 nm. To investigate the effect of the bubble size distribution, we vary the maximum amount of variation in the bubble radius from ±0.0% to ±30.0%. Figure 9 demonstrates three of the initial bubble configurations used in the analysis.

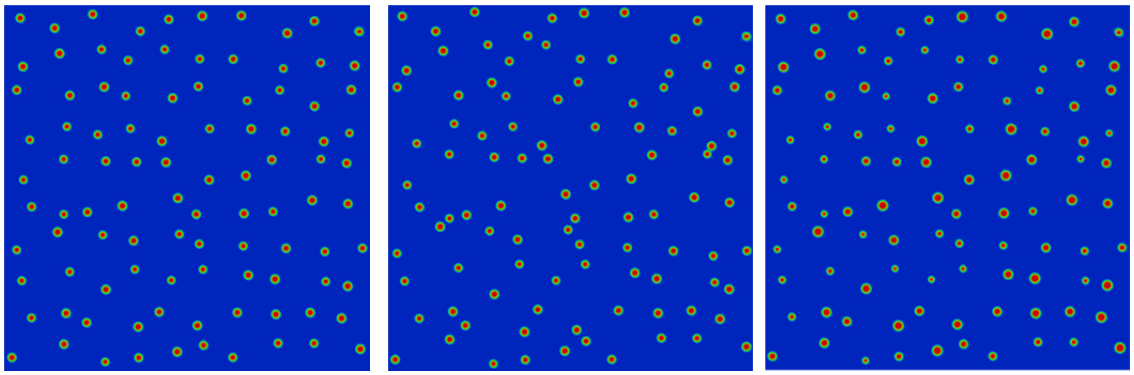

Figure 9: Example domains for the initial condition investigation, showing a 10% radius variation and a 3.0 nm position variation (left), a 10% radius variation and a 4.5 nm position variation (center) and a 30% radius variation and a 3.0 nm position variation (right).

By comparing the change in the bubble density with time, we found that the bubble configuration has little effect on the bubble growth, as shown in Fig. 10a. However, the initial bubble size distribution does have an effect (Fig. 10b). As the variation in the initial bubble radius increases from 0.0% to 40.0%, the time at which the first bubble disappears decreases, going from 4 minutes with 0.0% variation to 3 minutes with 40.0%. In addition, the rate at which the bubble density decreases with time decreases with increasing variation. However, this difference is no longer evident once the bubble density has reached 30% of its original value. Thus, the selection of the initial bubble configuration has little effect on our simulations but the bubble size distribution has a significant effect on the initial stages of the bubble growth.

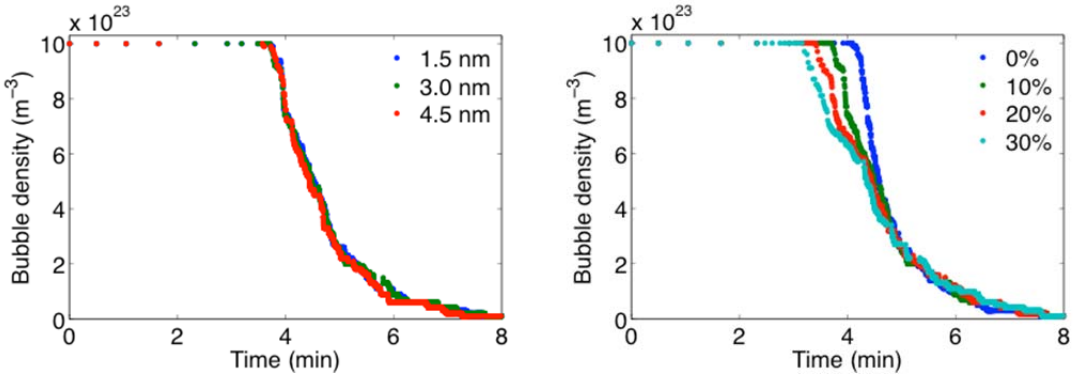

Figure 10: Investigation of the effect of the initial condition of the bubbles using a 100 nm by 100 nm domain, where (a) shows the effect of the variation in the bubble position and (b) the effect of variation in the bubble radius.

We also investigate the effect of a 3-D simulation on the relationship between bubble diameter and bubble density. For the sake of computation time, we simulate the bubble growth in a 20 nm by 20 nm by 20 nm cube of UO_2 with identical conditions and initial bubble density to our 2-D simulations. Thus, 8 initial gas bubbles exist in our domain. We found that unpressurized 1 nm radius bubbles were not stable in our 3-D domain, thus we increased our mean radius to 1.5 nm

with a uniform variation of up to ±10.0%. The bubbles were placed in a uniform lattice and the positions were than varied randomly by up to ±3.0 nm. See Fig. 11(a) to see the initial 3-D bubble configuration

The 3-D simulation was run until a single bubble remained, which occurred after 5.24 minutes of simulation time. We compared the relationship between bubble mean diameter and bubble density for the 3-D simulation to the fit from Kashible et al. [1] and our 2-D results (see Fig. 11(b)). Due to the higher initial radius, the initial point is shifted closer to the fit than for our 2-D simulations. Once the mean diameter begins to increase, the slope of the data seems to compare much better with the experimental fit than the 2-D results. From these results, it 2-D simulations under predict the decrease in the bubble density with increasing diameter. We suspect that this is because the 2-D simulations only capture the gas atom flux in the x-y plane.

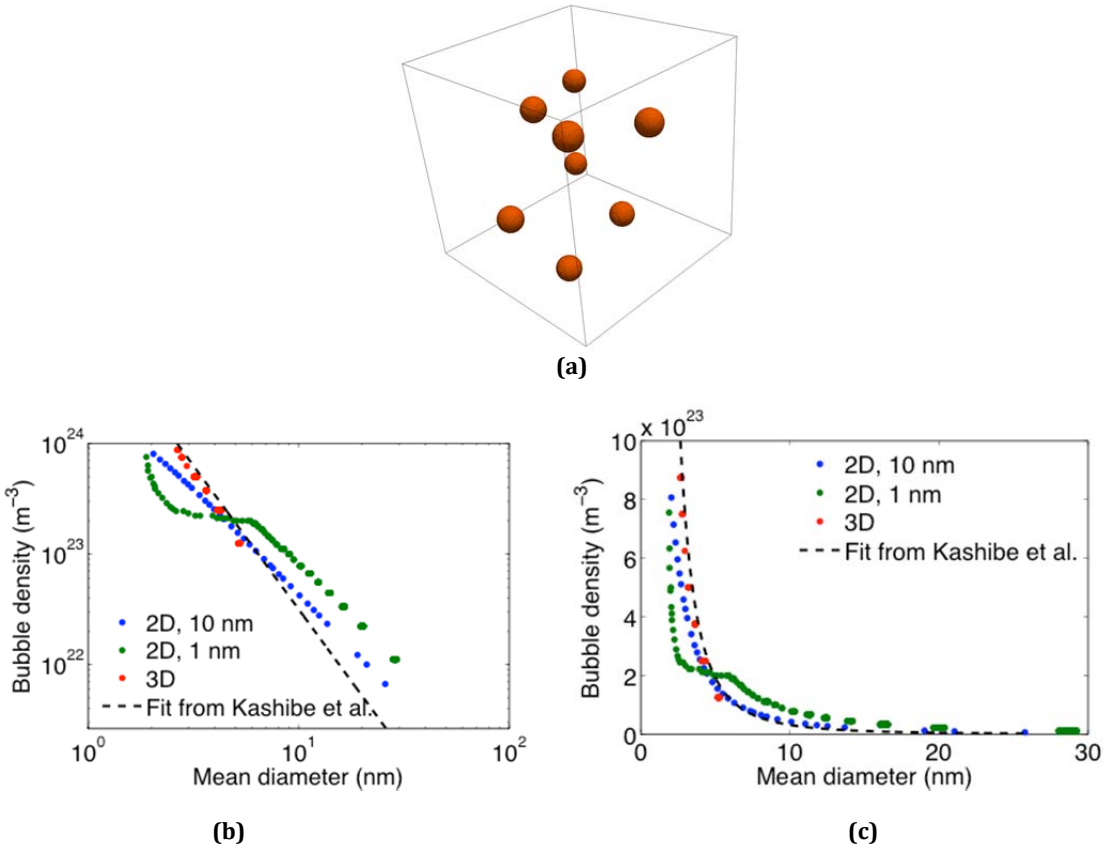

Figure 11: Simulation results from our small 3-D simulation with 8 initial bubbles with the 2-D results shown for reference, where (a) shows the initial bubble configuration and (b) shows the relationship between mean bubble diameter and bubble density, with a log-log plot on the left and a linear plot on the right.

References

[1] S. Kashibe, K. Une, K. Nogita, J. Nucl. Mater. 206 (1993) 22–34.
[2] M. Tonks, D. Gaston, P. Millett, D. Andrs, P. Talbot, Comp. Mat. Sci. 51 (2012) 20–29.
[3] N. Moelans, B. Blanpain, P. Wollants, Phys. Rev. B 78 (2008) 024113.

Appendix C
SNL--Potts Model Simulation of Intragranular Bubble Coarsening During Post-Irradiation Annealing

Veena Tikare
Sandia National Laboratories
March 30, 2012

C-1 Assumptions

During irradiation of LWR fuels, Xe atoms are formed due to fission of U. Xe has extremely very low solubility in UO_2 estimated to be of order magnitude 10^{-10}. It is thought that the Xe atoms present in the UO_2 lattice have associated with it a large strain energy field as it "stuffs" itself into the UO_2 lattice. Thus, under irradiation conditions, the Xe atoms will precipitate out onto almost any imperfection or feature to which it can attach. Furthermore, once Xe atoms start to precipitate to form bubbles, more Xe will precipitate to enlarge the bubble. The exact behavior and details of these events will be dictated by the local temperature, fission rate density and the local defect density[i]. The details of how these occurred and accumulated in the fuel will not be addressed here. However, it is noteworthy that the phenomena being considered here occurs in the center of the fuel pellet where the temperature is highest during irradiation.

The starting point of the benchmark exercise is the case where LWR fuel has been irradiated to 23 GWD/MTU is then subjected to annealing at 1800 ^{o}C. Before annealing, Xe atoms (and some Kr that will be neglected for the present exercise) have formed bubbles that are 2 nm and have a density of $9x10^{23}$ bubbles/m^3. These bubbles are randomly distributed with a distribution in sizes. We assume constant strain energy and free energy of the matrix phase. The only change in free energy is due to mixing. Ideal solution of mixing is assumed.

C-2 Potts kinetic Monte Carlo (kMC) Model

The Potts kinetic Monte Carlo (kMC) is a statistical-mechanical model that populates a lattice with an ensemble of discrete particles to represent and evolve the microstructure. The particles evolve in a variety of ways to simulate microstructural changes. kMC methods have proven themselves to be versatile, robust and capable of simulating various microstructural evolution processes. They have the great advantage of being simple and intuitive, while still being a rigorous method that can incorporate all the thermodynamic, kinetic and topological characteristics to simulate complex processes. They are easy to code, readily extendable from 2D to 3D and can simulate the underlying physics of many materials evolution processes based on the statistical-mechanical nature of the model. These processes include curvature-driven grain growth[ii], anisotropic grain growth[iii], recrystallization[iv], grain growth in the presence of a pinning phase[v], Ostwald ripening[vi], and particle sintering[vii]. The equation of state characterizing the materials in kMC is the sum of the bulk energy of each particle and

the sum of all the interfacial energy of each particle as $E_{kMC} = \sum_{i=1}^{N}\left(E_v(q_i) + \frac{1}{2}\sum_{j=1}^{n} J(q_i, q_j) \right)$ where N is the total number of particles, E_v is the bulk energy of each particle i, J is the neighbor interaction energy of particle i with its neighbor j for a total number of neighbors n and q_i is the grain orientation and or phase of particle i. Highly tailored equations of state for many different types of materials processes can be constructed using this basic equation. The evolution of the microstructures can be described in a simplistic manner as done by mimicking the atomic transport mechanisms that maybe active. For example, for simulation of curvature-driven grain growth, the Potts model particle at a grain boundary can change its state to align itself with the neighboring grain orientation much like an atom at a grain boundary can diffuse a very short distance to align itself with the neighboring grain orientation. These changes are performed using the standard Metropolis algorithm based on Boltzmann statistics.

C-2.1 Initial Microstructure for Gas Bubble Coarsening

The initial microstructure for the simulation is a single grain with periodic boundary conditions. The initial microstructure for the gas bubble coarsening simulation was obtained by a "nucleation and growth" simulation. Nucleation sites are placed randomly in the simulation space with uniform probability of occurring anywhere in the simulation space. The density of the nuclei were chosen to match the parameters of this benchmarking exercise with density i = 9x10^{23} bubbles/m^3. The "dissolved" Xe gas was also distributed uniformly at random lattice sites in the simulation space. The diffusion of Xe atoms was simulated by random walk with no bias. Only local compositional gradients influence diffusion. The starting microstructure is shown in figure 1.

The simulation method to generate the starting microstructure used a cubic lattice of 500 x 500 x 500 sites. This forms the simulation space of 100 nm x 100 nm x 100 nm portion inside a UO_2 grain with a voxel length l = 0.2 nm. The probability of any given site in the simulation being a nucleation site is p_n = 1000 / 500^3 = 8x10^{-6}. Thus the number of bubbles nucleated as approximately 1,000. The volume fraction of bubbles in the simulation is V^b_f = 1000 * 4π/3 * (1nm)^3 /(100nm^3) = .00419. This volume fraction was used for the volume fraction of Xe in the simulation.

The Potts kMC method was used to generate the initial microstructure. The entire simulation space is populated with a single grain structure. Nucleation sites chosen at random. Gas atoms are placed in the simulation space at random locations to match the desired volume fraction. The gas atoms are then allowed to diffuse by random walk. Each gas atom site attempts to exchange places with a neighboring site. Neighboring sites are the 26 1st, 2nd and 3rd nearest neighbors on the cubic lattice. A neighboring site of the gas atom is chosen at random from the 26. If the neighboring site is a grain site, then an exchange is attempted. The energy for this exchange is evaluated based on interfacial energy alone using the following EOS:

$$E = \frac{1}{2}\sum_{i=1}^{N}\sum_{j=1}^{26} J(1 - \delta(q_i, q_j)) \qquad \text{eq. 1}$$

where: N is the total number of sites, 26 is the number of neighbors in the cubic grid, J is a constant weighting the neighbor interaction energy, q_i is the state of the current site, q_j is the state of the j-th neighbor site and δ is the Kronecker delta with: $\delta(q_i, q_j) = 1$ for $q_i = qj$ and $\delta(q_i, q_j) = 0$ for $q_i \neq q_j$. According to this energy definition, only unlike neighbors contribute to energy, i.e. only interfacial energy of the system is defined. The exception is for the nucleation sites; if a gas atoms is a neighbor of a nucleation site, the neighbor interaction between them is $J(q_g, q_n) = 0$. Thus nucleation is encouraged.

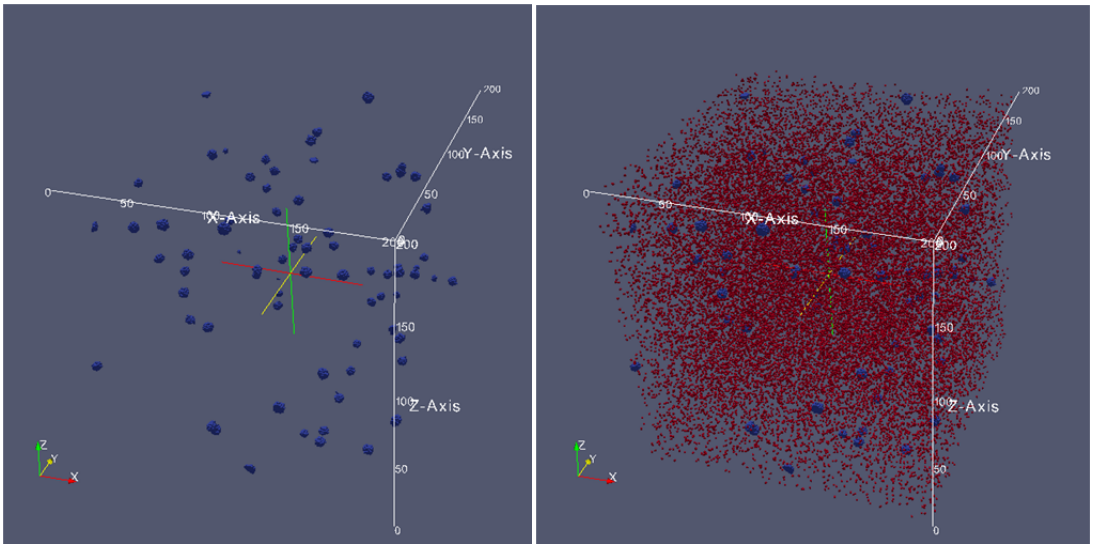

Figure 1. The initial microstructure for the simulation. Only a portion of the simulation space is shown as the entire space is too large. The blue features are gas bubbles and red are the dissolved gas. The volume fraction of gas in the bubbles is 0.0015 and dissolved is 0.0027.

For this special case of generating the initial microstructure for the simulation, all attempted gas diffusion exchanges that result in energy change $\Delta E \leq 0$ are accepted. A portion of the resulting microstructure is shown in Figure 1. While the simulation size is 500 x 500 x 500 lattice sites, a corner of 200 x 200 x 200 lattice sites is shown in Figure 1. Only the bubbles are imaged in Figure 1a and both bubbles and the Xe atoms in solution in the matrix are imaged in Figure1b. Bubbles are randomly distributed in space with a range of sizes. The bubble size distribution is shown in Figure 2 as a histogram of bubble radii. The histogram of bubble volume is almost a normal distribution as required by the benchmark exercise, however the radial histogram is shown as this is conventional for showing the microstructural feature size distributions.

C-2.2 Simulation of Intragranular Gas Bubble Coarsening

The irradiated fuel has bubbles of radius r = ~1nm. The gas in these bubbles is pressurized due to capillarity and the pressure in the bubbles is given by $P = \frac{2\gamma}{r}$. In a

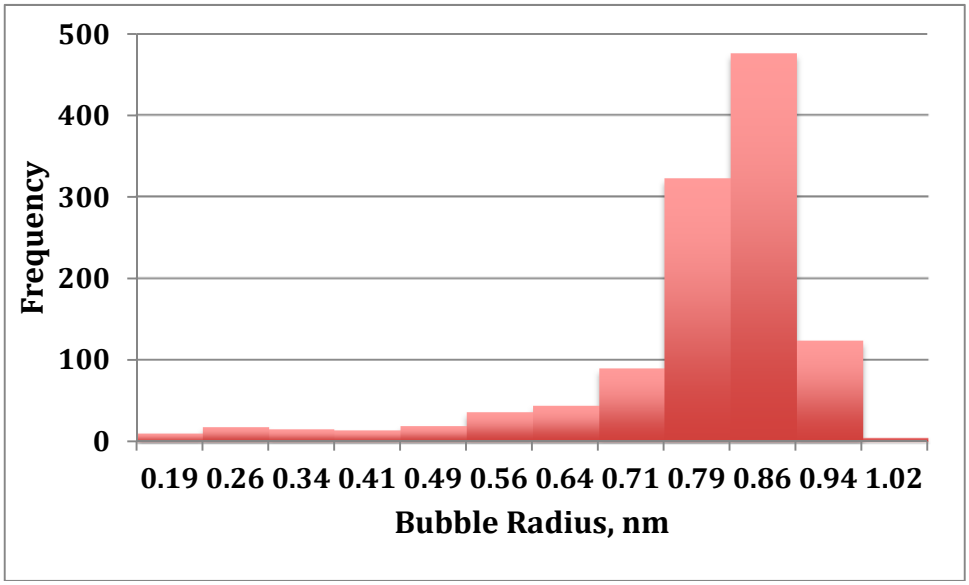

Figure 2. Bubble size distribution of the initial bubble population. Note distribution is near normal when plotted as bubble volume.

LWR fuel where the UO_2 lattice is highly strained by the Xe atoms dissolved in the lattice, precipitation into bubbles greatly reduced the strain in the lattice and the pressure in the gas bubble must be $P = \frac{2\gamma}{r} + P_o$ where the P_o is the pressure in the lattice at the bubble interface. The benchmark problem also outlines the case with uniform dislocation field and vacancy emission from the dislocations. These conditions translate to constant diffusivities in the simulation space.

The starting condition is both the lattice is strained by the extra dissolved Xe atoms and bubbles are under higher stress than that due to capillarity. The stress distribution in the system can be approximated by assuming a strain due to the extra Xe atoms stuffed into the lattice with the boundary condition at the bubble/UO_2 interface being that the pressure in the bubble is the same as that in the lattice at the interface.

During post-irradiation heating, the overall free energy of the system, which is $E = E_{chemical} + E_{interfacial} + E_{strain}$, is minimized along a path that is determined by this initial microstructural state to give microstructural evolution. Note $E_{chemical}$ and E_{strain} are both in the lattice and the gas bubble and $E_{interface}$ is due to the area between them. In this case, the Xe (and other fission product) atoms in the lattice increase both the $E_{chemical}$ and E_{strain}. The fuel before the annealing has a highly strained UO_2 lattice as well as nano-bubbles under high pressure, higher than capillarity would yield. During annealing precipitation of Xe into bubbles reduces the overall free energy of the system by reducing mostly likely E_{strain} and $E_{chemical}$. The coarsening of the bubbles subsequently is primarily to due to decrease in $E_{interface}$.

A Potts kMC model is applied to simulate this problem as follows. Again, an ensemble of particles that populates the simulation lattice grid represents the microstructure. Each particle has a discrete integer value, called spin, that designates which microstructural feature it belongs to. In this simulation, there are only two features, one grain and the bubble phase. Therefore there are only two spins for describing the microstructure. The energy of the system is given by

$$E = \sum_{i=1}^{N} F_i + U_i + \frac{1}{2}\sum_{j=1}^{26} J(1-\delta(q_i,q_j)) \qquad \text{eq. 2}$$

where U_i is the strain energy density for site i,

$$U_i = \frac{P_{o,i}^2 l^3}{2Y}$$

in the solid lattice and

$$U_i = P_{o,i} l^3$$

in the gas bubble. $P_{o,i}$ is the pressure at site i , which has volume l^3. Y is Young's modulus. F_i is the bulk free energy of the material at site i and is a function of the local composition and temperature. (This equation is the same as the free energy function given by the first equation in the section titled *Total Free Energy* in the document *Problem-1_Definition_V2-2-6-12.pdf*. The equation in the document is in the phase-field formulation. This one is the statistical-mechanical equivalent of an ensemble.) For simplicity and because no more details are available F_i and U_i are assumed to be the following. F_i is assumed to be only due to the entropy of mixing of the two components, UO_2 and Xe gas. U_i is assumed to be constant. This is true within the bubble, but not so in the lattice. However given the stress state in lattice, the Potts model can easily incorporate the lattice stress effects using eq. 2.

In the Potts model bubbles coarsen by randomly walk and coalescence, and by the gas in the bubbles dissolving back in the lattice and re-precipitating out on other bubbles. Both these are simulated by random walk of the bubble sites. During each Monte Carlo Step, MCS, each bubble site attempts to exchange places with one of its neighboring sites chosen at random from its 26 neighboring sites. If the chosen neighboring site happens to be a grain site, then the change in energy ΔE is evaluated using eq. 2. The standard Metropolis algorithm is used to determine if the attempted exchange is executed or not. Boltzmann statics are used to calculate the probability W of the exchange.

$$W = 1 \qquad \Delta E \le 0$$

$$W = \exp\left(\frac{-\Delta E}{k_B T}\right) \qquad \Delta E > 0 \qquad \text{eq. 3}$$

In this way, all the materials transport mechanisms that are active in bubble coarsening are simulated. Individual particles that are dissolved in the UO_2 lattice can diffuse by random walk and they can precipitate to onto existing bubbles. The bubble particles can also detach from the bubble surface become dissolved and this process is in proportion to the pressure in the bubble, thus dissolution of gas preferentially from smaller, higher pressure bubbles is simulated. Time in the simulation is also

introduced by this probability function as they probability of a given event during a time step naturally introduces the time scale. Furthermore, if the rates of each of the events is known, then the probability is easily adjusted by adding the known rate term in this probability. In this simulation, since the rates are not well known, we simply chose them to be related only to the free energy change (with no activation energy for any of the processes) as this results the fastest times for this simulation. However a detailed explanation of the rate calculations is given below. The free energy of mixing (1st equation in section titled Chemical free energy of matrix and gas phases) is introduced into the Potts model by the statistical-mechanical nature of its ensemble. The probability of the two types of particles mixing is simulated in the model by equation 3. It gives ideal mixing at low concentrations when "dissolved" particles don't interact with each other with the correct entropy of mixing $K_BT(X_i lnX_i)$.

The diffusion coefficient for the random walk process in this simulation is given here. The diffusion coefficient for the randon walk process is $D = \frac{1}{6}\frac{n}{\tau}l^2$ where n is number of random jumps, τ is the time increment for n jumps and l is the jump distance and is the lattice size. Using n = 1 jump for time τ = 1MCS and l = 0.2 nm, D = 6.7x10^{-17} cm^2/MCS. Thus, the time in these Potts model simulations can be related to real time by determining the proportionality between the MCS and seconds.

C-3 Results and Discussion

This model is applied to simulate bubble coarsening. The microstructures showing bubble coarsening are shown in Figure 3. A portion of the simulation space, 200 x 200 x 200 lattice sites corresponding to 40 nm x 40 nm x 40 nm, is imaged as the entire space is too large and this section shows sufficient detail and extent to illustrate the behavior well. The small red dots in are the "dissolved" gas in the lattice. The bubbles are the spherical, large, red features. As can be clearly seen the bubbles are coarsening. The bubble growth curve is shown in Figure 4. As expected, the bubbles are coarsening. The time scale for this simulation was determined by estimating that the bubble would coarsen to 10 nm in 10 minutes. The simulation started with a total of 1176 bubbles with average radius <r> = 0.8 nm and ended with 142 bubbles of <r> = 2.2 nm. The size distribution of the bubbles is shown in figure 5 at different times during the simulation. The skewness of the distribution at the later times is surprising. The skewness was anticipated to be to the larger sizes as it is at short times during annealing.

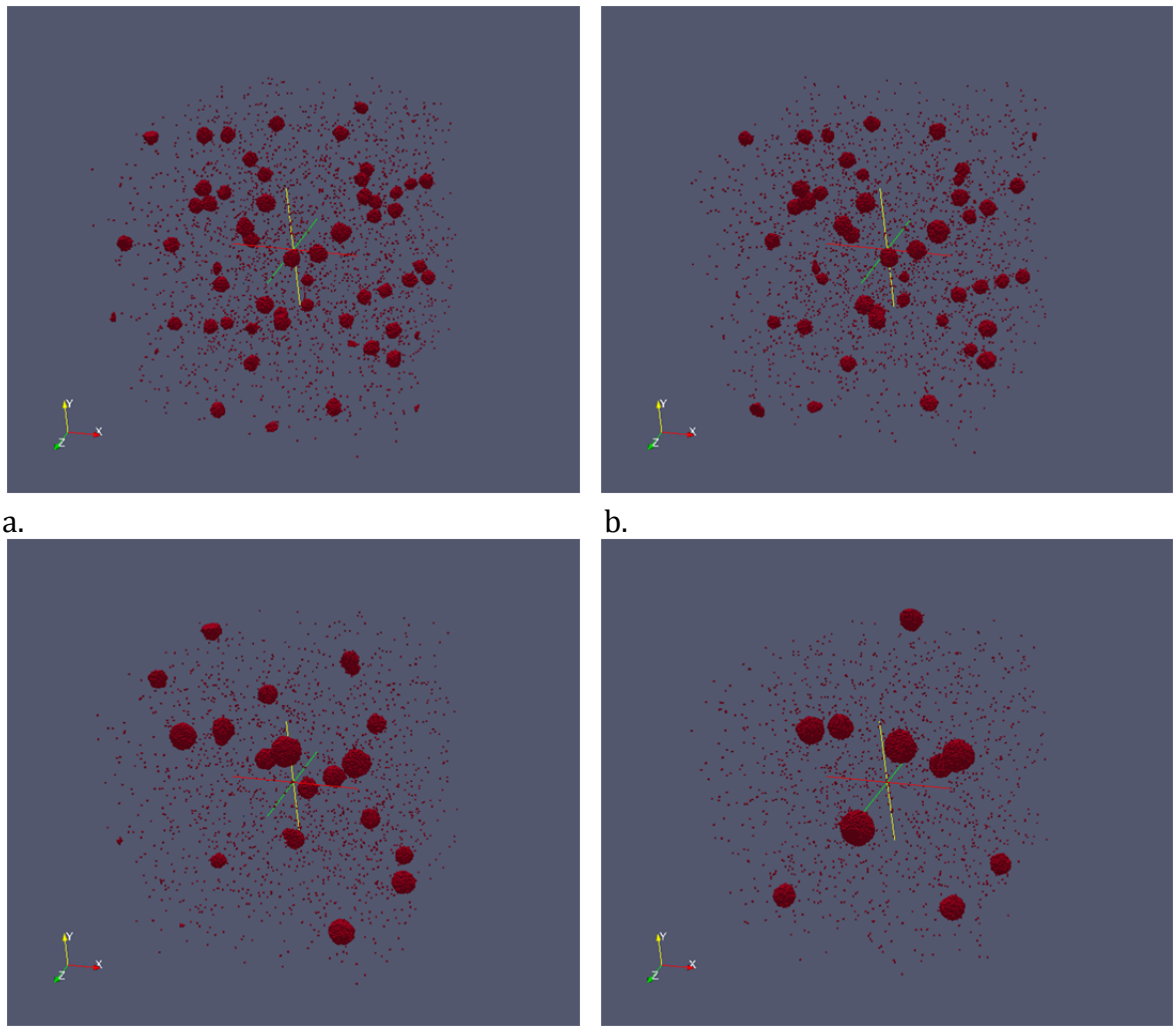

a. b.

c. d.

Figure 3. Microstructure of bubbles coarsening. (Only a portion of the simulation space is imaged, $200^3\ l^3$ corresponding to 40 nm x 40 nm x 40nm).

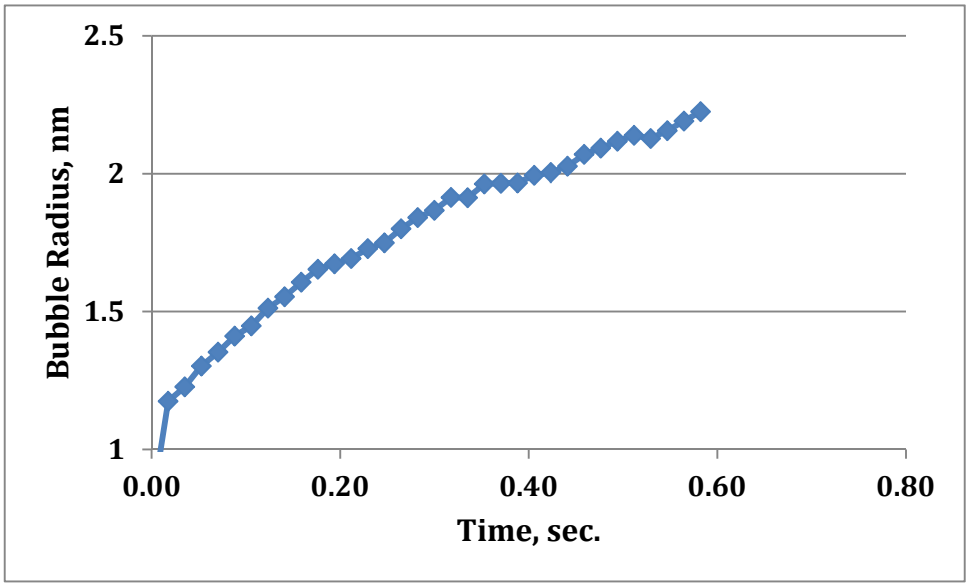

Figure 4. Average bubble radius as a function of time.

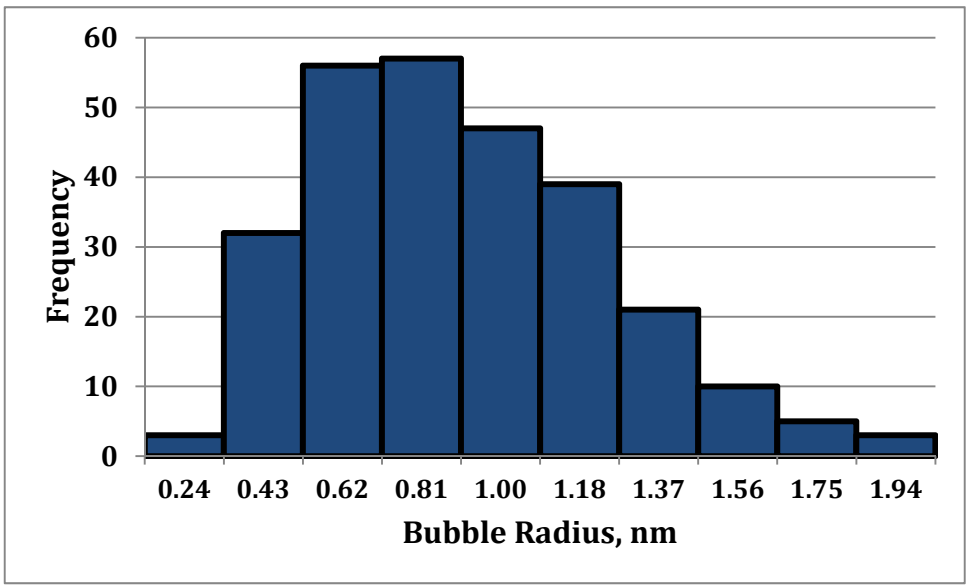

a. Time = 0.18 sec, <*r*> = 1.65

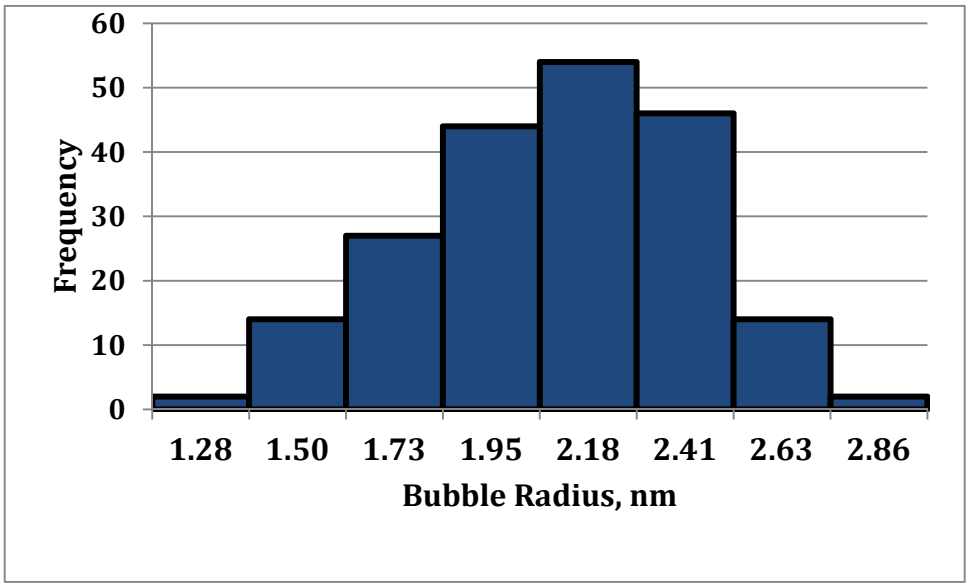

b. Time = 0.35 sec, <*r*> = 2.0

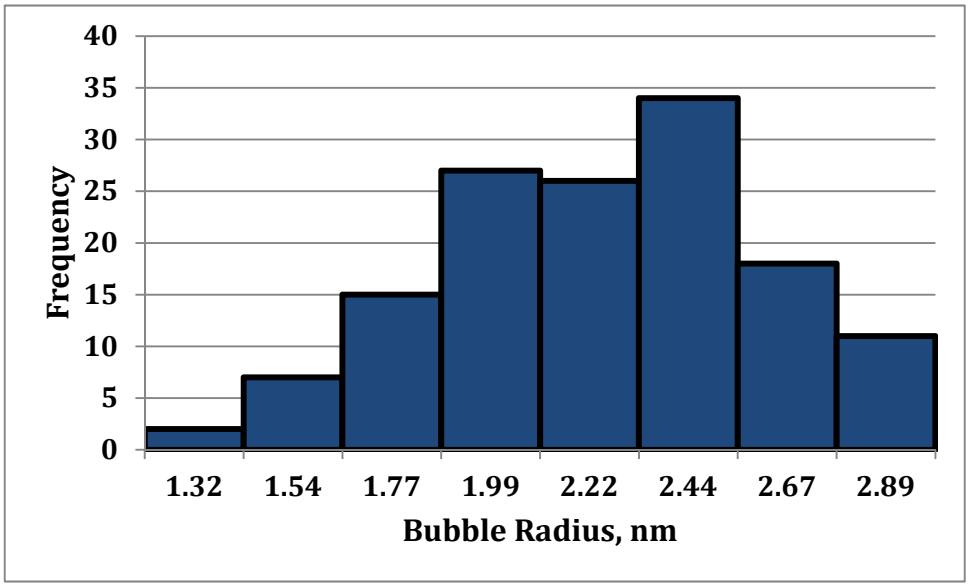

c. Time = 0.58 sec, <*r*> = 2.2

Figure 5. Bubble size distributions as the bubbles coarsen.

This work demonstrates the basic Potts kMC framework and its application to simulation of intragranular gas bubbles. It demonstrates that bubble coarsening by solution-reprecitation transport mechanism. The particular physics of this problem with strain energy-driven transport and coarsening have not been incorporated as the strain energies are not know. However, these can easily be incorporated as they become known or are provided.

No attempt was made to incorporate the Carnahan-Starling EOS which compensates for the non-ideal gas behavior at such high pressure, in this exercise. However, this is fairly easy as it is simply a function of that particular bubble's volume. The pressure of the gas in the bubble is calculated using the Carnahan-Starling EOS and the concentration of the solute in the matrix is adjusted accordingly as $C = C_\infty P_{CS}/P_\infty$ where P_{cs} is the Carnahan-Starling pressure and P_∞ is the pressure and C_∞ is the solubility of a bubble with radius $r = \infty$.

It is noteworthy that this particular problem is not a good demonstration of the capabilities of Potts kMC. The computational resources needed to solve the problem presented above were enormous. The simulation presented above required 24 hours on 100 nodes with 8 processors per node. Due to its statistical mechanical nature, long-range diffusion and low solubility compositions are computationally very demanding for the Potts kMC model. Long-range diffusion is simulated by random-walk of individual particles much like an atom hopping in a lattice. And low concentrations of a second phase requires a large number of lattice sites to resolve the microstructure and composition. However, it can simulate this problem and it can do it correctly by incorporating all the necessary physics. Furthermore, Sandia is developing a hybrid capability for this type of materials physics that will allow faster simulation of problems with long-range diffusion. The mechanical component needed for simulation of the strained lattice and pressurized bubbles can also be easily be introduced into a hybrid by coupling to a FEM or other mechanical solver.

Two-dimensional simulation of the same problem was requested by the benchmark team. The simulation was set up and run in the same manner described above, but in 2D. Equation 2 is now modified to consider the eight 1st and 2nd nearest neighbors instead of the 26 used in 3D simulations. The results are shown here briefly. The simulation size used was 1500 x 1500 sites. This corresponds to 300 nm x 300 nm simulation space. The starting bubble size is r = 0.9 nm with 131 bubbles initially. Figure 6 and 7 show the microstructures and bubble size growth, respectively. The bubble size curve for the 2D simulations is noisy as the number of bubbles is small; the simulation ends with only 11 bubbles.

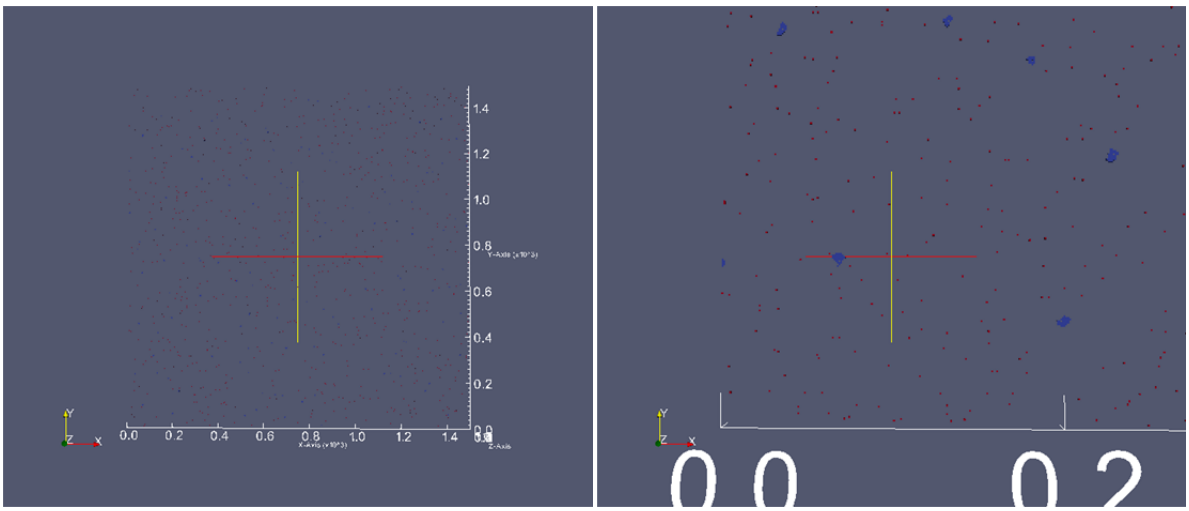

a. **b.**

Figure 6a. The entire microstructure used for the 2D simulation. b. A small quadrant in the lower left side showing the details of the bubbles.

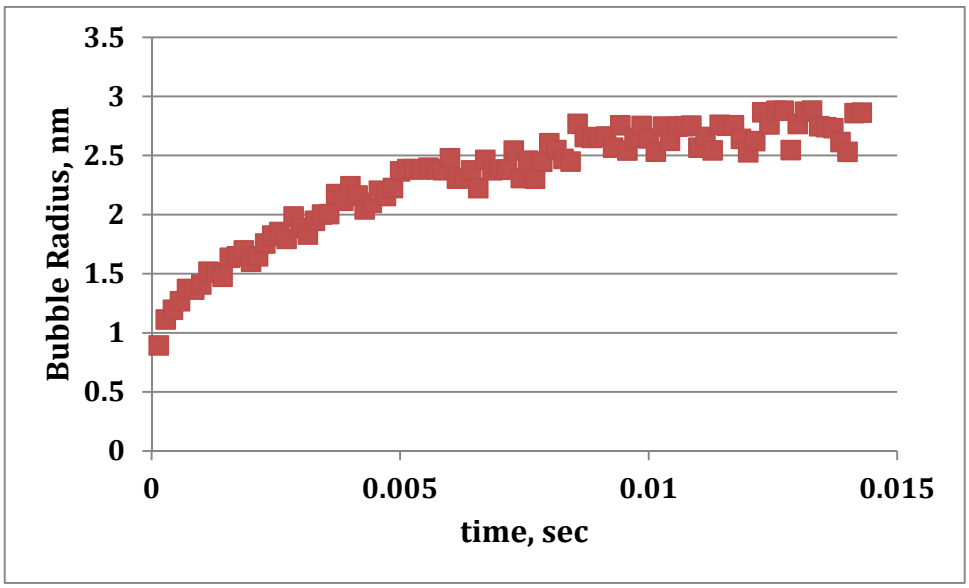

Figure 7. Bubble growth curve for 2D bubbles.

References

[i] J. Noirot, L. Desgranges, J. Lamontagne, *J. Nucl. Mater.,* 2008, 372 318-339.

[ii] M. P. Anderson, D. J. Srolovitz, G. S. Grest, and P. S. Sahni, *Acta Metall.,* 1984, 32, 783-791; E. A. Holm, J. A. Glazier, D. J. Srolovitz, G. S. Grest, *Phys. Rev. A,* 1991, 43, 2662-2668.

[iii] E. A. Holm, G. N. Hassold and M. A. Miodownik, *Acta Mater.,* 2001, 49, 2981-2991

[iv] J. Madison, V. Tikare and E.A. Holm, *J. Nucl. Mater.*, 2011, doi 10.1016/j.jnucmat.2011.10.023; E. A. Holm, M. A. Miodownik and A. D. Rollett, *Acta Mater.,* 2003, 51, 2701-2716.

[v] M. Miodownik, J.W. Martin and A. Cerezo, *Phil. Mag. A*, 1999, 79, 203-222; V. Tikare, M. Miodownik, E. A. Holm, *J. Am. Ceram. Soc.,* 2001, 84, 1379-1385

[vi] V. Tikare and J.D. Cawley, *Acta Mater.* 1998, 46 1333-1342; V. Tikare and J. D. Cawley, *ibid,* 1998, 46, 1343-1356; S-B Lee, J.M. Rickman and A.D. Rollett, *Acta Mater*., 2007, 55[2] 615-626

[vii] G.N. Hassold, I-W. Chen, D. J. Srolovitz, *J. Am. Ceram. Soc.,* 1990, 73, 2857-2864; V. Tikare, M. Braginsky and E.A. Olevsky, *ibid,* 2003, 86, 49-53; M. Braginsky, V. Tikare and E. Olevsky, *Int. J. Sol. Struc.,* 2004, 42, 621-636; V. Tikare, M. Braginsky, D. Bouvard and A. Vagnon*, Comp. Mat. Sci.,* 2010, 48, 317-325.

Appendix D: ORNL-- Detailed Potts/KMC Simulation and Result Analysis

Objective: The objective of this effort is to utilize a Potts/KMC model to solve a test problem [1] that involves simulating the coarsening of intra-granular Xe bubbles during post-irradiation anneal of UO2.

Model Description: The Potts/KMC model developed at ORNL is based on the simulation approach published recently by Suzudo et al [2]. The mesoscale simulation domain consists of three "species" – the matrix volume elements that are made of UO2, "void" volume elements that are made up of a collection of condensed vacancies (green) and "bubble" elements that consist of a collection of vacancies and gas atoms (red). The formation of larger "extended bubbles" occurs through a collection of voids and bubble sites. Based on the simulation approach by Suzudo et al [2], we define three types of Monte Carlo moves:

(1) Exchange of a void and a matrix site to simulate surface diffusion
(2) Exchange of a void and a bubble site to simulate Xe diffusion inside the bubble
(3) Creation or destruction of a void site at the bubble-matrix interface

In the Monte Carlo procedure used, all three events are attempted with the same frequency. However, the success of each flip will depend upon the local energy change associated with the event, as described later. The ability of such an approach to simulate the balance between internal gas pressure and bubble size has been demonstrated. The application of this procedure to the equilibrium bubble configurations for an intra-granular bubble and a bubble situated on a grain boundary obtained using the ORNL code is shown in Fig. 1.

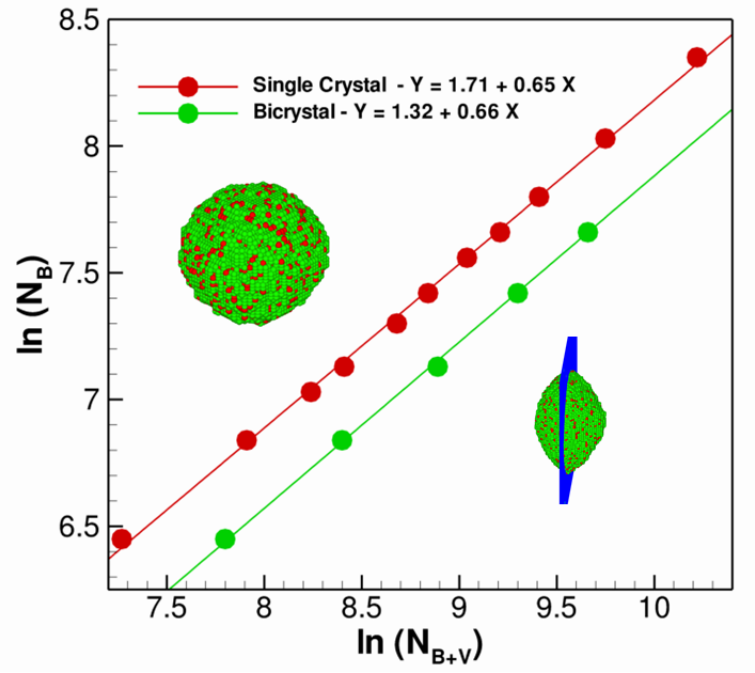

Fig. 1. Equilibrium of single extended bubble in a single crystal and on a grain boundary satisfying equation of state PV = nRT.

The simulations are able to capture the ideal slope of 2/3 for gas bubbles that obey the ideal gas law. However, in the current simulations, the equation of state (EOS) for Xe published by Ronchi [3] was used to represent the relationship between gas pressure and volume at 1800K the temperature of interest in the current benchmark problem. The Potts/KMC code was run in parallel computer using 64 nodes. The code scales efficiently and it is possible to run much larger simulation volumes that are necessary to extend the simulations to polycrystalline grain structures with a fine spatial resolution. In the current simulations, an attempt is also made to include "pinning sites" inside the matrix to account for the drag on the migrating bubbles due to dislocations or fission fragments. This is by no means rigorous, especially for dislocations that involve spatially varying forces, but a formal approach for incorporating such effects into mesoscale simulations would involve longer-term effort. A major requirement for using such a mesoscale approach is establishing a relationship between the simulation time-space parameters and real time-space coordinates. A methodology used to obtain this correlation is described below.

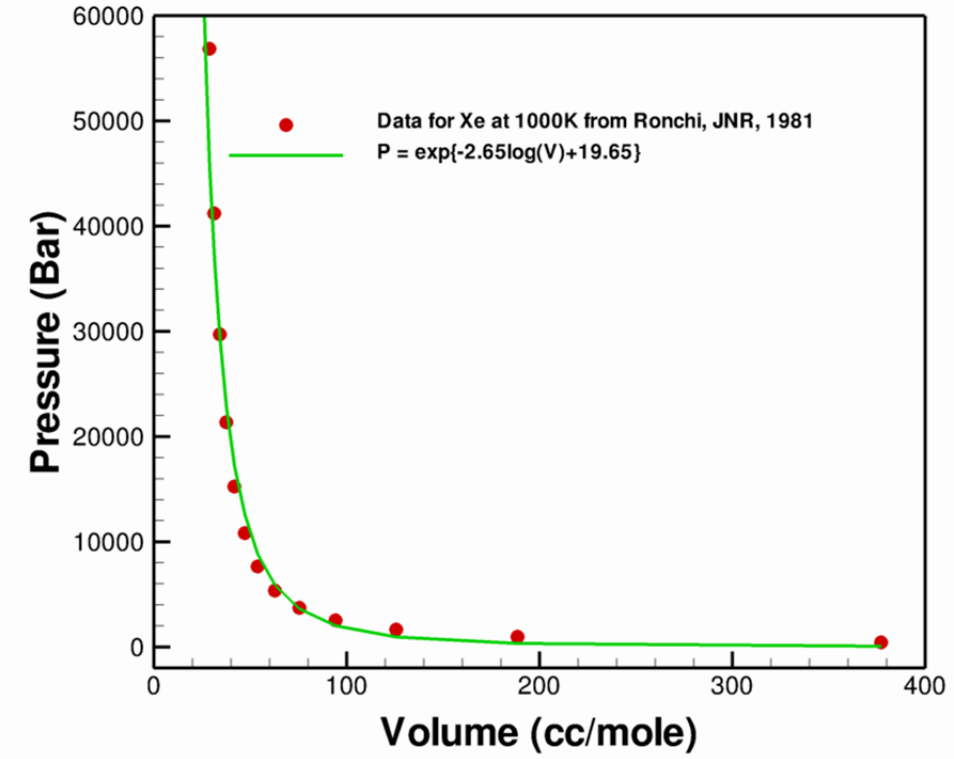

Fig. 2. Equation of state for Xe at 1800K from Ronchi [2] and the analytical fit to the data points

The equation of state (EOS) for the Xe bubbles by Ronchi [3] for Xe gas at 1800K, and an analytical fit to the data are shown in Fig.2. In Fig.2, the pressure is in Bars and the volume is in cc/mole. The analytical equation shown in Fig.2 was used in

the calibration procedure for temperature. In MC simulations, the flip of sites associated with the three MC moves is made as usual according a probability given by

$$p = \begin{bmatrix} 1 & \Delta E \le 0 \\ \exp\left(\frac{-\Delta E}{kT}\right) & \Delta E > 0 \end{bmatrix}, \quad (1)$$

where ΔE is the change in energy associated with the flip and kT is the reduced lattice temperature. The Hamiltonian for the system, in the absence of dissolved gas atoms and long-range volume diffusion and concentration gradients, reduces to the surface energies of the various moving interfaces. The first step in the calibration process is to obtain the relationship between kT in equation 1 and $K_b T_R$ where K_b is the Boltzmann constant and T_R is the real temperature in degree Kelvin.

The procedure for calibrating the temperature was as follows. Initially a length scale was assumed for the Potts model. In this case, it is assumed that each site is a sphere with a radius of 1 nm. An initial assumption of the reduced lattice temperature kT was made. The simulation cell consisted of a single crystal with an embedded extended spherical bubble with a radius of 10 nm consisting only of bubble sites. Since such a configuration does not satisfy pressure equilibrium, as the simulation proceeds the extended bubble acquires vacancies in order to reach pressure equilibrium at the assumed lattice temperature. From the bubble radius, the equilibrium gas pressure P_{eq} was obtained using $P_{eq} = 2\gamma/R$. The equilibrated extended bubble contains a known amount of bubble sites and void sites with a known number of atoms inside each bubble site. The equivalent gas volume in cc/mole was calculated. Using the value of gas volume in the Ronchi EOS at 1800K, the gas pressure was calculated. The calculated pressure, P_{EOS} was compared against P_{eq}. The calculations showed that the two pressures approached each other when the lattice temperature kT was 4.75. Table 1 shows P_{eq} and P_{EOS} for various assumed values of kT. At low kT values, P_{eq} is lower than P_{EOS}. The two values cross each other between kT=4.5 and kT=4.75. In all the subsequent simulations, a reduced lattice temperature of 4.75 was used to simulate the evolution at 1800K.

Table 1. Temperature Calibration showing the convergence of P_{eq} and P_{EOS}

MC Lattice Temp (kT)	$P_{eq} = 2\gamma/R$ (Bars)	P_{EOS} (From Ronchi, EOS) (Bars)
3.0	681	2811
3.5	646	1858
4.0	583	819
4.5	571	694
4.75	549	514

In order to establish the relationship between the Monte Carlo time step (MCS) and the real time in seconds, the following procedure was adopted. A simulation cell consisting of a single crystal and an embedded extended void with a void radius of 20 nm was used in a Monte Carlo simulation. The objective of the simulations was to calculate the mean square displacement (MSD) of all the void sites at a lattice temperature of kT=4.75. The size of each void site was 2.0 nm (1 nm radius) and the lattice temperature was set to 4.75 to correlate with a real temperature of 1800K. The average MSD per void site when plotted against MCS gave a straight-line plot as shown in Fig. 3.

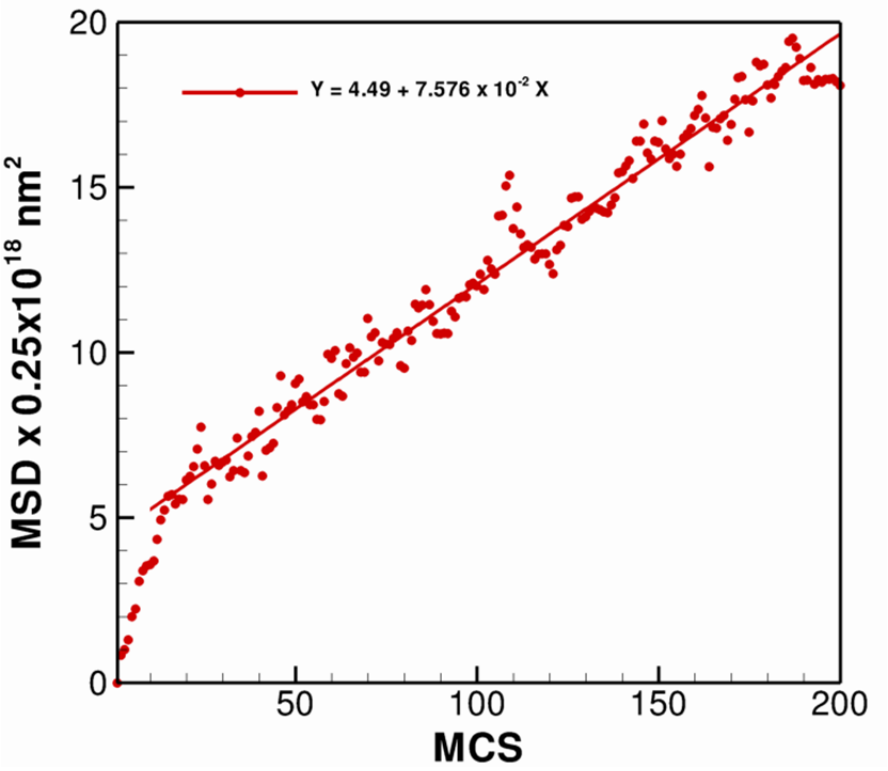

Figure 3. Mean square displacement of void sites adjacent to the void-matrix interface obtained using MC simulations

The MSD corresponds to the surface "diffusion" of the void sites. MSD of uranium atoms adjacent to a void have recently been obtained using molecular dynamics simulations by Desai et al [4]. However, the data is available only for temperatures of 2700K and above. Therefore, the value for 1800K was obtained by extrapolating the results in [4] to 1800K, to obtain a surface diffusion coefficient of 1.0 x 10-15 m^2/s. It should be noted that the oxygen atoms have a much higher diffusivity and there fore are not rate controlling. By comparing the MSD/t in MD with MSD/MCS in the simulations, the relationship between real time and MCS was found as 1 s = 19400 MCS.

Assumptions

1. All the gas atoms reside inside the bubble sites – there is no solubility of Xe in the matrix during annealing.
2. The bubble sites are initially at equilibrium, that is, the pressure exerted by the gas atoms inside the bubble elements balances the surface tension of the bubble-matrix interface. Therefore, there are no long-range stress fields in the matrix associated with pressurized bubbles.
3. The system largely evolves by random migration of the bubbles driven by surface diffusion of U atoms based on an exchange between the void sites and the matrix sites. When two bubbles coalesce, the pressure equilibrium is violated. Restoring the equilibrium occurs by the pressurized bubbles acquiring a void site.
4. The exact mechanism by which the non-equilibrium bubbles acquire void sites is not modeled rigorously; it is assumed that the probability of acquiring a void is proportional to the energy change associated with creating additional void-matrix interface.
5. The effect of matrix dislocations and fission fragments on pinning bubble motion is considered by introducing a fraction of pinning sites in the simulation volume

A simulation cell of 300 x 300 x 30 sites with a site diameter of 2 nm corresponding to a 600 x 600 x60 nm3 volume was in the simulations of bubble evolution at 1800K. From the data provided in [1], the number of atoms in the simulation cell is 350.146×10^4. The number of gas bubbles in the same simulation volume is 19,440. Therefore, if we assume that all the gas atoms are present inside the bubbles with no dissolved gas atoms in the matrix, the total number of gas atoms in each 2nm diameter bubble is 180. Now, the equilibrium gas pressure inside a 2nm diameter bubble can be calculated as $P = 2\gamma/R$. Using a surface energy of 1.0 N/m the equilibrium gas pressure is 20,000 bars. Substituting it in the Ronchi EOS [3], the specific volume of the gas in cc/mole is 39.56 cc/mole. If the volume occupied by the bubble is $4\pi R^3/3$, then it turns out that the number of gas atoms in the equilibrium bubble is 191 atoms per bubble. This is not too far from the value of 180 atoms per bubble based on the assumption that all atoms reside inside the bubbles!

There is a difference in the coarsening behavior of the bubbles versus voids. Although both coarsen by surface diffusion and produce a coarsening curve skewed to the right indicating migration and coalescence, there is a major difference due to the Xe pressure inside a bubble. As mentioned previously, each bubble site is assumed to consist of a certain concentration or number fraction of gas atoms that balance the surface tension between the bubble and the matrix. However when two bubble sites coalesce to produce an extended bubble, the pressure equilibrium is disturbed. Even though the volume is conserved instantaneously, the pressure equilibrium requires a net increase in the surface area of the coalesced bubble. The

mechanism by which this is achieved is by the bubble acquiring more vacancies. In the Potts model, the excess vacancies are heterogeneously nucleated at the bubble matrix interface.

Results and Discussion

The variation of the mean bubble size with annealing time at 1800K is shown in Fig. 4. So far, the simulation has run only up to a total annealing time of just over 1 minute. The mean bubble size has evolved from 2 nm to about 30 nm during this period. The growth curve is not smooth especially at the later stages when large bubbles overlap followed by pressure equilibration. It is also clear that the growth rate is accelerating at larger simulation times.

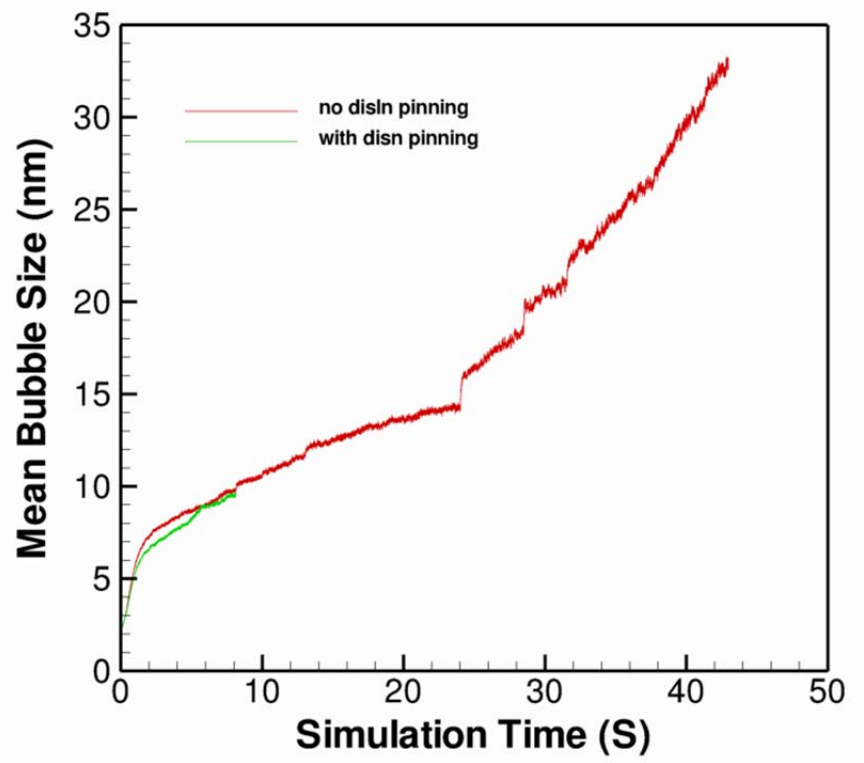

Figure 4. Variation of mean bubble size with annealing time

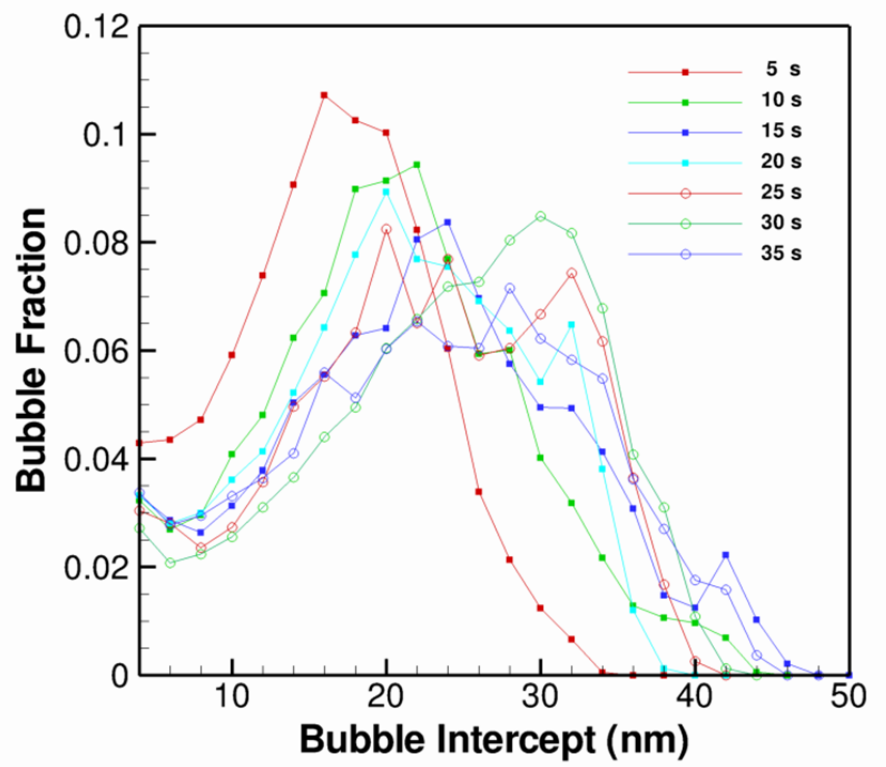

Figure 5. Bubble intercept distribution as a function of simulation time.

Figure 5 shows the distribution of pore intercepts as a function of the simulation time. At early times, the evolution of the structure by bubble migration and coalescence produces a smooth variation of mean pore size versus time up to about 25 s. During this time, the bubble size distribution has a characteristic asymmetrical distribution skewed to the right (the peak is at the left compared to a symmetric curve). However, at longer times, associated with accelerated growth the bubble size distribution changes character with the asymmetry changing to a skewed left (the peak is at the right compared to a symmetric curve).

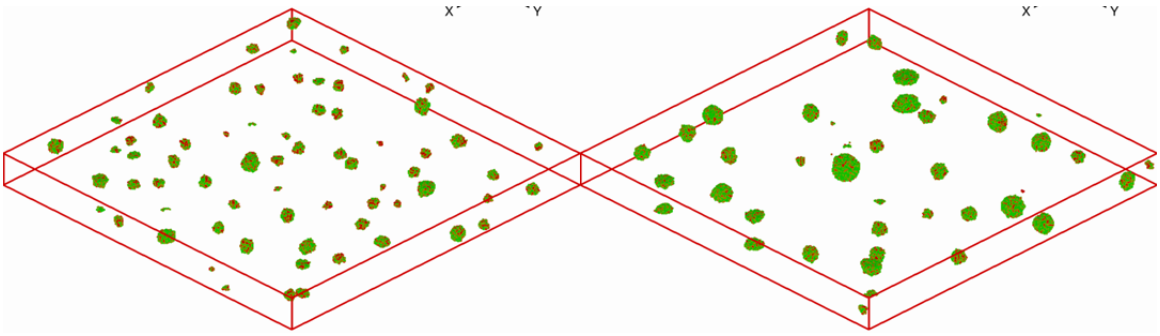

5 S 15 S

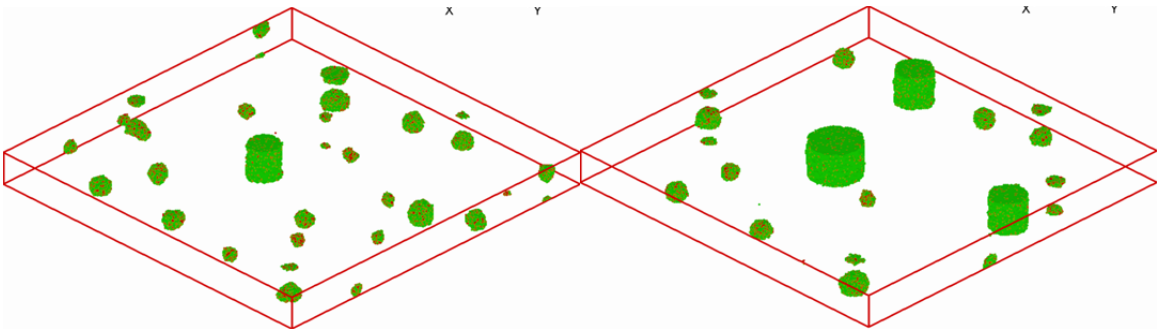

Figure 6. Temporal evolution of the bubble structure at 1800K.

The temporal evolution of the bubble structure is shown in Fig. 6. It is clear that at later stages of the growth, the three-dimensional character of the bubble growth is violated, with the formation of cylindrical bubbles. Since these bubbles cannot migrate freely in all three directions, their mobility is significantly reduced. Further growth appears to occur mainly by other migrating bubbles of smaller sizes coalescing with the bigger and cylindrical bubbles. The accelerated growth seen at later stages appears to result from this phenomenon. It is possible that the accelerated growth rate is due to the breakdown of ideal 3d conditions. It is also interesting that the bubble size distribution changes from one characteristic of migration and coalescence (skewed right) to a distribution characteristic of Ostwald Ripening (skewed left). This probably because the larger bubbles, especially the ones that become cylindrical are essentially stationary and they act as sinks to smaller bubbles, mechanistically resembling Ostwald ripening process. It should be noted that the simulation box size of 300 x 300 x30 sites was chosen on the basis of the recommendations from the FMM group in order to be consistent with the other efforts for comparison. However, it is clear that in this case it introduces a decrease in the dimensionality of the problem and associated changes in the kinetics.

In order to verify this hypothesis, larger 3-D runs were made with a 208 x 208 x 208 sites using 512 processes. The size of each site was again 2.0 nm. Figure 7 shows the growth kinetics of the bubbles, which is significantly smoother than the one shown in Fig. 4. Figure 6 also shows the growth curve in the presence of a small volume fraction (0.005) of "dislocated" sites acting as pinning sites. In these simulations, it was assumed that contact with "dislocated" sites will completely suppress surface diffusion locally for the site. It is clear that pinning reduces the growth kinetics. However, it is not clear at this point how to correlate the dislocation density with the fraction of "dislocated" sites. Also, the long-range stress fields associated with the dislocations have to be considered unless the dislocations are present in the form of a recovered low-angle grain boundary network at the annealing temperature. By adjusting the volume fraction of the dislocated sites it is possible to match the simulation and annealing data of Kashibe et al [5].

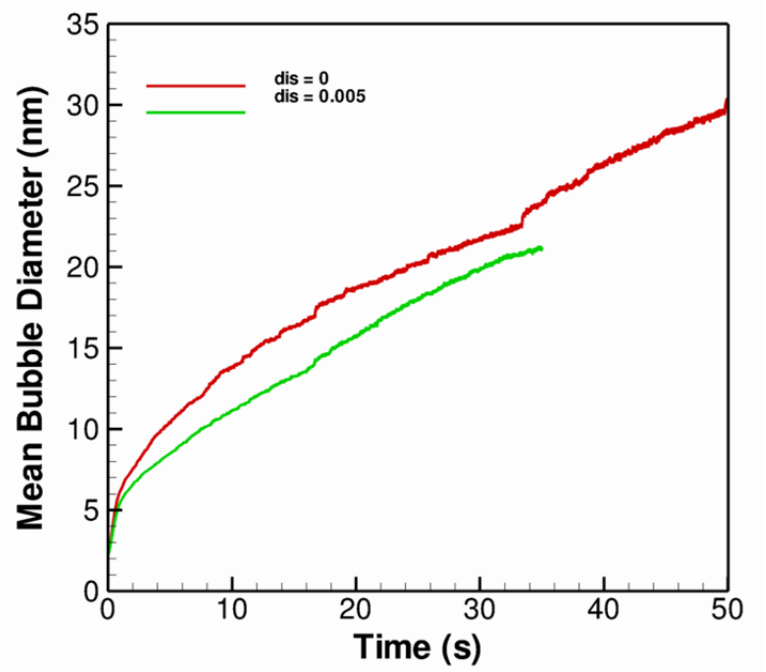

Fig. 7. Bubble growth kinetics in a 416 x 416 x 416 nm^3 simulation volume

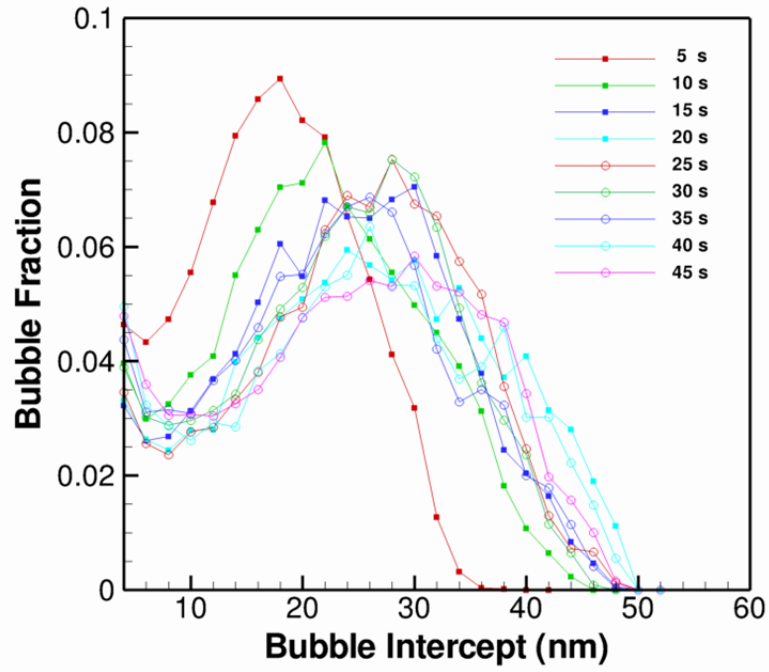

Fig. 8. Bubble size distribution obtained using 416 x 416 x 416 nm^3 run

Figure 8 shows the bubble size distribution in the case of the larger run. Note that the transition from migration and coalesce lik e distribution to Ostwald Ripening like distribution seen in the smaller run no longer exists.

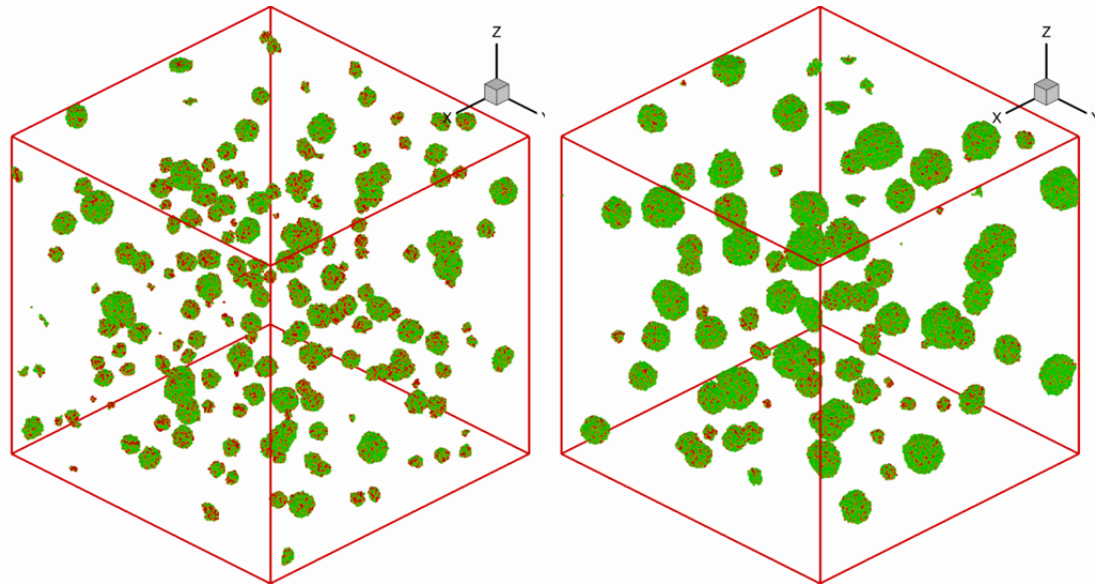

5 s 15s

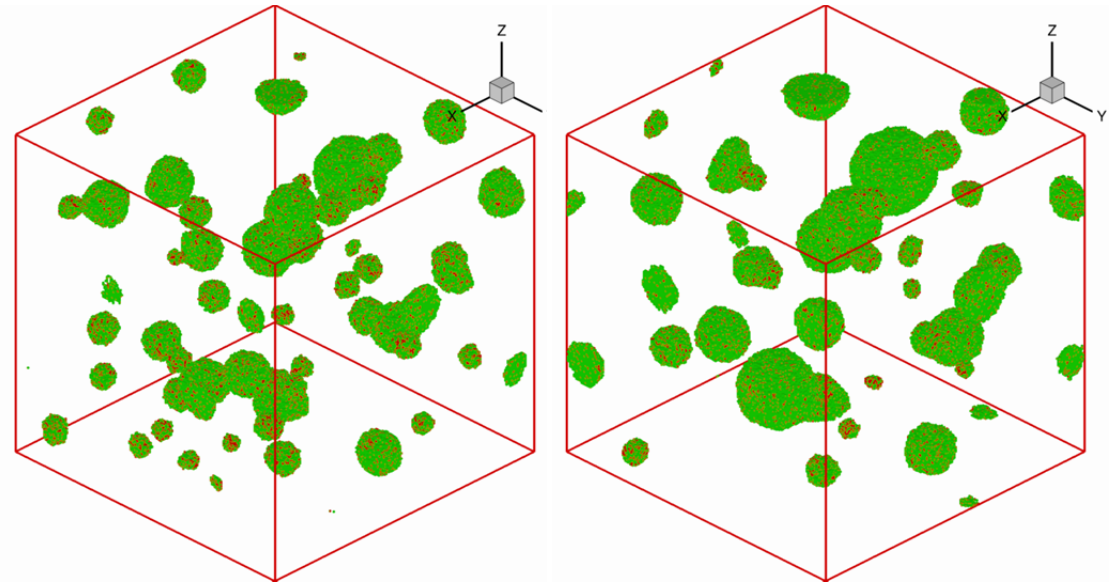

30 s 45 s

Figure 9 shows the temporal evolution of the bubbles in the 416 x 416 x 416 nm^3 run showing migration and coalescence mechanism operating throughout the simulation time.

The temporal evolution of the bubbles is shown in Fig. 9 for the larger run. It is clear that the cylindrical bubbles that formed in the smaller domain do not form and there is no sudden increase in the growth rate as observed in the smaller run. However, a few growth bumps are seen in Fig. 7 that corresponds to rare coalescence events associated with large bubbles.

The calibration of the Potts/KMC code can be rescaled at any time during the simulation, with the assumption that each simulation cell now corresponds to a larger bubble size. The structure should be re-mapped so that the spatial distribution of the bubbles will be preserved. With this re-mapping, it is now possible to change the relationship between MCS and time such that each MCS now corresponds to a larger real time. Such an approach has been demonstrated for simulation grain growth in steels [6]. Therefore the simulations can be used efficiently to follow the structure evolution at annealing times of hours.

Input/Data Needs

1. Effective pinning force due to dislocations at any location due to the cumulative effect of all the dislocations within a cut off radius. This should also take into account whether the geometry of the spatial distribution of the defects (tangle versus regular network)
2. Interfacial energy as a function of temperature and Xenon pressure
3. Strain and strain gradient in the matrix due to non-equilibrium bubbles (when bubbles coalesce)
4. Kinetics of absorption of vacancy at the bubble-matrix interface. This involves modeling the long-range diffusion of vacancies in the matrix in the presence of the dislocations
5. Attachment-detachment kinetics for vacancies near non-equilibrium bubbles

Bibliography

1. R. Montgomery, internal communication.
2. T. Suzudo et al., "A three-dimensional mesoscale modeling for bubble growth in metals," Modelling Simul. Mater. Sci. Eng 16 (2008) 055003
3. C. Ronchi, "Extrapolated Equation of State for rare Gases at High Temperatures and Densities," JNM 96 (1981) 314-328
4. T.G. Desai et al., "Atomistic Simulations of Void Migration under Thermal Gradient in UO_2," Acta Mater. 58 (2010) 330-339.
5. S. Kashibe, K.Une and K. Nogita, "Formation and Growth of Intragranular Fission Gas Bubbles in UO2 Fuels with Burnup of 6-83 GWd/t," JNM 206 (1993) 22-34
6. B. Radhakrishnan and T. Zacharia, "Monte Carlo Simulation of Grain Boundary Pinning in the Weld Heat Affected Zone," Metallurgical and Materials Transactions A, 26 (1995) 2123-2130.

Appendix E

LANL--Data from Atomistic Simulations

David Andersson

Los Alamos National Laboratory

This section contains a brief discussion of the model parameters that are required for simulating UO_2 post-irradiation annealing experiments at the meso-scale. We focus on perspectives obtained from recent atomic level simulations and relate these results to available experiments. The discussion is not meant to cover all aspects of the problem, but rather exemplifies a few cases where atomic level simulations have made an impact on the understanding of material properties that couple directly to meso-scale models. This work is published [1,2,3,4] or in the process of being published [5,6].

Oxygen interstitials and vacancies

From both simulations [2,3,5] and experiments [7,8,9] it is clear that oxygen vacancies and interstitials move several orders of magnitude faster through the UO_2 lattice than cations or fission gases. The migration barriers for anion vacancies and interstitials are ≈0.5 [7,10] and ≈0.9-1.3 eV [6,7,10], respectively, while the lowest barrier for cations (a cluster of two uranium vacancies that can form under irradiation) is predicted to be 2.6 eV [3] and the barrier for migration of single uranium vacancies is 4.5-4.8 eV [3,5]. Based on these observations it is recommended to make simplifying assumptions regarding the distribution of anion defects, since full coupling of cation and anion dynamics would result in significant numerical challenges. One possibility is to treat anion species as always being in equilibrium with respect to the distribution of cation defects. For stoichiometric UO_2 where oxygen vacancies and interstitials appear in approximately equal concentrations under thermal equilibrium, transport occurs predominantly via vacancies due to their lower migration barrier. For UO_{2+x} the concentration of oxygen interstitials or clusters thereof exceeds that of vacancies. Consequently, interstitials and clusters of interstitials dominate the diffusion properties in this stoichiometry range [2,6,11]. In addition to the kinetic properties, meso-scale models need information regarding the concentration of oxygen vacancies and interstitials. This is available from thermodynamic models derived from either experiments [12] or from calculations [1,3]. For strictly stoichiometric UO_2 the oxygen vacancy formation energy and the interstitial formation energy are both half the Frenkel energy, which implies 1.5-2.0 eV from both theory [3] and experiments [8,9].

Uranium interstitials and vacancies

Migration of uranium interstitials was recently investigated using density functional theory calculations [5] and the barrier was calculated to be 3.7 eV for the indirect

interstitialcy mechanism, which is lower than the barrier for single uranium vacancies but about 1 eV higher than for clusters of uranium vacancies (see below). Under thermal equilibrium conditions the contribution from interstitials to cation diffusion is very small due to the negligible concentration of such defects compared to vacancies [5]. The activation energy for the uranium interstitialcy diffusion mechanism in stoichiometric UO_2 was calculated to be as high as 15-16 eV [5].

Experiments typically quote 2.4 eV as the migration barrier of uranium ions via a vacancy mechanism [8,9], which was derived by studying the recovery of UO_2 samples exposed to irradiation. If non-equilibrium clusters form under such conditions the measured barrier could refer to, .e.g., migration of uranium vacancy clusters rather than isolated vacancies. This was confirmed by recent computational studies, which predicted a barrier of about 4.5-4.8 eV for single uranium vacancies and about 2.6 eV for two nearest neighbor uranium vacancies [3]. Simulations of in-pile conditions should probably apply the lower cluster barrier, while the higher barrier for single uranium vacancies may better describe out-of-pile conditions. Uranium diffusion under thermal equilibrium conditions has been measured by a number of authors [8,9,13]. For stoichimetric UO_2 the corresponding activation energy is reported to range from 4.4 [13] to 5.6 eV [8,9]. The activation energy is a strong function of the $UO_{2\pm x}$ stoichiometry. For UO_{2-x} and UO_{2+x} the corresponding activation energies were reported to be 7.8 and 2.6 eV, respectively. In Ref. [3] we used density functional theory calculations to investigate the activation energy for uranium diffusion. Even though the agreement between theory and experiments was rather good [3], the model used for calculating the activation energies from the calculated thermodynamic and kinetic data was incomplete. A second paper [5] explored this in more detail for stoichiometric UO_2 and we achieved improved agreement with experiments compared to the earlier study [5]. The most up to date activation energy for uranium diffusion in UO_2 is 4.4 eV [13] and our calculations predict 4.1-4.9 eV [5]. Whether the meso-scale simulations should use the calculated migration barrier or the activation energy to describe the Arrhenius rates in the transport equations depends on the conditions that are being simulated, e.g. irradiation environments or thermal concentration of defects, and how the deviation from thermodynamic equilibrium is formulated. The effective value of the uranium vacancy formation energy depends on stoichioemtry and chemical environment. For strictly stoichiometric UO_2 we suggest 2.69 eV [3].

Fission gas

In order to understand fission gas transport one must first determine how the atoms interact with the fluorite UO_2 host, both what is the most stable equilibrium trap site but also high energy positions that might result as a consequence of irradiation, and the subsequent transport mechanisms for all forms of the gas within the matrix. Among the fission gases, Xe is the most prominent. Miekeley and Felix [14] performed early experiments on the release of Xe during post-irradiation diffusion anneal from $UO_{2\pm x}$ with a range of different stoichiometries (x). Perhaps the most striking conclusion from their work was that the activation energies for release exhibited unique values in the UO_{2-x} (6.0 eV), UO_2 (3.9 eV) and UO_{2+x} (1.7 eV)

regimes, respectively, while they were almost constant within each of these composition sets. This was interpreted as Xe atoms occupying vacancy trap sites, a concept that was investigated by Catlow [16] using empirical potentials of the Buckingham type. Later Ball et al. [15] applied similar techniques to investigate stability of Xe in trap sites as function of stoichiometry and charge state. According to Ball et al. [15], Xe atoms either reside in a neutral trivacancy cluster for UO_{2-x} and UO_2, a divacancy for UO_2 or in a U vacancy for UO_{2+x}. These conclusions agree well with earlier results by Catlow [16] and also by more recent DFT work [19]. The Xe solution thermodynamics establishes the foundation for species transport, and Ball et al. [15,17] further investigated how the Xe atoms may move from one lattice site to another by binding a second U vacancy to the respective Xe trap sites – a vacancy mediated diffusion mechanism. They proposed that Xe transport occurs by the Xe atom jumping from its original trap site to the second bound vacancy, which constitutes the center of a new Xe trap site after this migration step. In order for net Xe transport to take place, motion of the second vacancy bound to the Xe trap site must be considered. Since Ball et al. did not attempt to study the latter step, they did not compare their calculated data with measured activation energies.

We applied the DFT+*U* methodology to study diffusion of Xe under a variety of conditions [3]; in particular applying the thermodynamic model originally derived by Catlow [16] to calculate activation energies for Xe in the UO_{2-x}, UO_2 and UO_{2+x} ranges. This transport model requires calculation of the binding energy of a second U vacancy to the Xe trap site and the barrier for moving one of the constituent U vacancies to another location such that net transport is enabled. This diffusion mechanism involves three components: the V_U formation energy, the binding energy of this vacancy to the Xe trap site, and the intra-cluster migration barrier for the individual U vacancies bound to this cluster. That is, the rate-limiting step is not Xe motion within the cluster, but the migration of the second vacancy within the cluster; without the motion of the second bound U vacancy Xe does not diffuse.

We note that many earlier studies dismissed vacancy mechanisms, which was motivated by a number of experimental observations summarized by Matzke [9] and Miekeley and Felix [14]. For example, the activation energy in the UO_{2+x} regime was found to be a constant and it did not change with stoichiometry. However, according to our understanding, in experiments where the composition is allowed to vary as function of temperature according to thermodynamic equilibrium relations, the Xe activation energy should contain an additional term coming from the temperature dependence of the stoichiometry. Miekeley and Felix [14] estimated the corresponding Arrhenius energy to be -0.3 eV for UO_2 and UO_{2+x} based on their experiments. According to the thermodynamic model derived by Catlow [16] for UO_{2+x} we should add twice this energy to the Xe activation energy if the composition is not kept fixed in the experiments. This contribution was not accounted for in any computational studies so far, but adding this term to the calculated values for the Xe activation energy in the UO_{2+x} range in fact improves the agreement with the experimental data of Miekeley and Felix [14]. Preliminary work indicates that when the appropriate thermodynamic models are applied the activation energies derived

from density functional theory calculations are very close to the values measured by Miekeley and Felix [14] for all stoichiometries. Moreover, Govers [18] showed that alternative mechanisms based on migration via interstitial sites are unfavorable, thus lending support for the vacancy mechanism. The barriers for moving one of the uranium vacancies from one part of the Xe trap site to another is 3.91, 5.00 and 5.51 eV for the Xe_U (Xe occupies one uranium vacancy), Xe_{UO} (Xe occupies one uranium and one oxygen vacancy) and Xe_{UO2} (Xe occupies one uranium vacancy and two oxygen vacancies) trap sites, respectively. The corresponding defect formation energies are listed in Ref. [3]. For strictly stoichiometric UO_2 we suggest 4.35 eV.

Fission gases can also diffuse via interstitial mechanisms. Due to the large size of Xe atoms it is however unlikely that such mechanisms are important at high temperature since the interstitial Xe atoms would quickly recombine with uranium vacancies. If the Xe atom stays in interstitial positions it may diffuse with a rather low barrier (1.6 eV) compared to vacancy mechanisms [4].

Defect formation volumes

Table 1 lists the formation volumes of oxygen, uranium and fission gas (Xe) defects in stoichiometric UO_2. They were all calculated according to the definition of the corresponding defect formation energies [3]. Note that this definition is slightly more complex than in, e.g., pure metals, which must be accounted for in the meso-scale models.

Table 1: Formation volume of defects in stoichiometric UO_2.

Defect type	Formation volume [Å^3]
Oxygen vacancy	1.79
Oxygen interstitial	1.79
Uranium vacancy	42.3
Schottky defect (unbound)	45.8
Schottky defect (bound)	41.9
Xe	52.8

References

1. D. A. Andersson , J. Lezama, B. P. Uberuaga and S. D. Conradson, Phys. Rev. B **79**, 024110 (2009).
2. D. A. Andersson, T. Watanabe, C. Deo, and B. P. Uberuaga, Phys. Rev. B **80**, 060101(R) (2009).
3. D. A. Andersson, B. P. Uberuaga, P. V. Nerikar, C. Unal, and C. R. Stanek, Phys. Rev. B **84**, 054105 (2011).
4. X.-Y. Liu, B. P. Uberuaga, D. A. Andersson, C. R. Stanek, and K. E. Sickafus, Appl. Phys. Lett. **98**, 151902 (2011).
5. Boris Dorado, David A. Andersson, Christopher R. Stanek, Marjorie Bertolus, Blas P. Uberuaga, Guillaume Martin, Michel Freyss and Philippe Garcia, submitted for publication.
6. D. A. Andersson, F. J. Espinosa-Faller, B. P. Uberuaga and S. D. Conradson, submitted for publication.

7. G. E. Murch and C. Richard A. Catlow, J. Chem. Soc., Faraday Trans. 2 **83**, 1157 (1987).
8. Hj. Matzke, J. Chem. Soc., Faraday Trans. 2 **83**, 1121 (1987).
9. Hj. Matzke, Radiat. Eff. Defect. S. **53**, 219 (1980).
10. B. Dorado, P. Garcia, G. Carlot, C. Davoisne, M. Fraczkiewicz, B. Pasquet, M. Freyss, C. Valot, G. Baldinozzi, D. Simeone and M. Bertolus, Phys. Rev. B **83**, 035126 (2011) .
11. P. Ruello and G. Chirlesan and G. Petot-Ervas and C. Petot and L. Desgranges, J. Nucl. Mater. **325**, 202 (2004).
12. C. Gueneau, M. Baichi, D. Labroche, C. Chatillon and B. Sundman, J. Nucl. Mater. **304**, 161 (2002).
13. A. C. S. Sabioni, W. B. Ferraz and F. Millot, J. Nucl. Mater. **257**, 180 (1998).
14. W. Miekeley and F. W. Felix , J. Nucl. Mater. **42**, 297 (1972).
15. R. G. J. Ball and R. W. Grimes, Chem. Soc., Faraday Trans. **86**, 1257 (1990).
16. C. R. A Catlow, Proc. R. Soc. London Ser. A **364**, 473 (1978).
17. R. G. J. Ball and R. W. Grimes, J. Nucl. Mater. **188**, 216 (1992).
18. K. Govers, S. E. Lemehov and M. Verwerft, J. Nucl. Mater. **405,** 252 (2010).
19. P. V. Nerikar, X.-Y. Liu, B. P. Uberuaga, C. R. Stanek, S. R. Phillpot and S. B. Sinnott, J. Phys.-Condens. Mat. **21**, 435602 (2009).